Doctoral theses at NTNU, 2021:191

Fredrik Kjemperud Olsen

Controlling magnetic properties of $La_{0.7}Sr_{0.3}MnO_3$ by interface coupling and nanopatterning

Doctoral thesis

NTNU
Norwegian University of Science and Technology
Thesis for the Degree of
Philosophiae Doctor
Faculty of Information Technology and Electrical Engineering
Department of Electronic Systems

NTNU
Norwegian University of
Science and Technology

Fredrik Kjemperud Olsen

Controlling magnetic properties of $La_{0.7}Sr_{0.3}MnO_3$ by interface coupling and nanopatterning

Thesis for the Degree of Philosophiae Doctor

Trondheim, June 2021

Norwegian University of Science and Technology
Faculty of Information Technology and Electrical Engineering
Department of Electronic Systems

NTNU
Norwegian University of
Science and Technology

NTNU
Norwegian University of Science and Technology

Thesis for the Degree of Philosophiae Doctor

Faculty of Information Technology and Electrical Engineering
Department of Electronic Systems

ISBN 978-82-326-5474-1 (printed ver.)
ISBN 978-82-326-5491-8 (electronic ver.)
ISSN 1503-8181 (printed ver.)
ISSN 2703-8084 (online ver.)

Doctoral theses at NTNU, 2021:191

Printed by NTNU Grafisk senter

Summary

As modern technology has had tremendous development over the last century, the demand for increased computational power has become imminent. In order to meet this demand dense packing and down-scaling of electronic components has lead modern technology into the realm of nanophysics, and consequently many well-established technologies which are functional only at the macro-scale meet their limits. In search for materials systems which possess functional properties applicable for nanoscale devices, complex oxide materials are one of the promising candidates. Their correlated electronic and magnetic properties make them suitable for use in spintronics, a growing field with expected importance in the near future. However, oxides also display change of properties at the nanoscale, and even novel phases can emerge. In addition, for application of these materials in spintronics device designs the materials have to be defined into specific geometries, for instance as thin film layers or bits, and the patterning methods can also have a significant influence on the properties.

In this thesis, we investigate the effect of down-scaling ferromagnetic and antiferromagnetic thin film layers down to the nanometer scale. We do so by growing thin layers with varying thickness of ferromagnetic $La_{0.7}Sr_{0.3}MnO_3$ and antiferromagnetic $LaFeO_3$ - perovskite oxide materials with interesting properties for spintronics applications. We further impose lateral geometries by patterning of the thin films. The effect of two patterning methods are investigated, where nanomagnets are realized either embedded in a non-magnetic matrix, or as free-standing nanomagnets.

We use the pulsed laser deposition technique to realize high-quality epitaxial thin films and heterostructures with monolayer precision on $SrTiO_3$ substrates. Vibrating sample magnetometry is primarily used to investigate the macroscopic mag-

netic response of the materials system, and a combination of characterization techniques are utilized to further interpret and understand the observed effects. For instance, x-ray diffraction measurements are done to investigate the crystal lattice parameters and x-ray absorption spectroscopy is utilized to reveal the element specific magnetic spin orientations in separate layers. The main results are presented as two published journal articles and as one manuscript in preparation.

In paper A, investigating ferromagnetic thin films and bilayer antiferromagnetic/ ferromagnetic bilayers, we find that the $LaFeO_3$/$La_{0.7}Sr_{0.3}MnO_3$ materials system displays an exchange bias effect when the ferromagnetic layer is thin. The exchange bias effect shows several intriguing features, such as being obtainable without a field-cooling procedure and being observed to coexist with a spin-flop coupling between the two layers. Rather than requiring conventional field-cooling, the exchange bias is obtained by applying a setting field at elevated temperature and subsequent cooling in zero-field. In other words, the exchange bias effect is spontaneous in this system. This is also displayed by the effect being reduced as temperature increases up to an observed blocking temperature, where it disappears, and by a large fraction of the bias being found to be preserved after subsequent cooling. Furthermore, the exchange bias effect is found to have significant dependence on a setting field's strength, temperature at which the field i applied and the thickness of the ferromagnetic layer.

In paper B, the effect of lateral structuring, i.e., by patterning of the ferromagnetic thin films, is investigated by x-ray magnetic dichroism spectroscopy. It is found that for a region close to the nanomagnet edges, the dichroism signal is enhanced near the Curie temperature, which could be a sign of stronger ferromagnetic ordering. At the Curie temperature, the signal extends ~ 150 nm inwards into the nanomagnet from the edges while no dichroism signal is observed at the center of the nanomagnets. X-ray diffraction measurements performed on extended arrays of line-shaped nanomagnets reveal an asymmetric change in lattice parameters. Out-of-plane, the lattice parameter is increased, while in-plane it is reduced perpendicular to the long-axis of the line shaped nanomagnets. Along this long-axis, no change is observed. This change in lattice parameters is strongest for embedded structures, which is assumed to be correlated with an in-plane pressure exerted by surrounding matrix. The embedding non-magnetic matrix which has been subject to ion-bombardment swells in volume. This can in turn cause a pressure to be exerted onto the embedded magnets.

In paper C, the switching properties of line-shaped nanomagnets oriented along an [100] crystallographic direction are investigated for the effect of patterning and the effect of an $LaFeO_3$ layer. It is found that the patterning imposes a strong shape anisotropy, giving rise to an increase ($\sim 120 - 150$ %) in the coercivity

which is largest for embedded nanomagnets. The effect of an $LaFeO_3$ layer is found to give a reduction (~ 30 %) in the coercivity. Since the effect of $LaFeO_3$ in non-patterned films has the opposite effect, namely an increase in coercivity, this finding signifies that lateral structuring has an important influence on the effect an antiferromagnetic $LaFeO_3$ layer has onto $LaFeO_3$/$La_{0.7}Sr_{0.3}MnO_3$.

With these results, we have revealed and elaborated on magnetic properties which are important to $LaFeO_3$/$La_{0.7}Sr_{0.3}MnO_3$ at the nanoscale. The emergent exchange bias effect can be tuned by ferromagnetic layer thickness as well as external fields and temperature control. Anisotropy introduced by patterning and/or coupling to an adjacent $LaFeO_3$ layer can be used to modify the switching properties, which can prove useful in spintronic applications.

Preface

Curiosity, and simply the interest in how nature is composed drives the progression of science. Today, however, the technology which has emerged from progression in science is so integrated in our society that one can safely state; scientific progress is of interest to the general public whether you are curious in the physics of the underlying components or not. Saying the 20th century has been fruitful for human development is a modest understatement. This spring, a worldwide pandemic struck our daily lives but already this month vaccines are being rolled out for large scale vaccination. We live in extremely interesting times, and I am thankful for being allowed to participate in it.

The work in this thesis is that of experimental character. I have had the pleasure of getting hands on experience by synthesizing materials, processing and characterizing them. The setups I have used are highly sophisticated and I have everyone else to thank for the chance to use them. From high voltage source electron guns to vacuum chambers, lasers, monochromic x-rays and even large scale synchrotron facilities; these are systems which together has made my research possible, and it has all been enabled by the collective work of the scientists that came before me. It really makes me humble.

Rewinding back to 2014, when I was half way through my Master's degree's final semester, where I worked on (111)-oriented perovskites together with Ingrid and Thomas, Erik approached me with a proposition that the adventure of oxides did not need to end here. I was in one of my best student years, done with background coursework and finally getting hands on experience in the lab, continuously learning more about the fascinating field of complex oxide physics. Knowing Erik as one of my favorite lecturers and as a friendly colleague of my supervisors, there really was no question on what to do, and so my project started in 2015.

The last five years have been filled with so many experiences there is no way I can mention them all, even though I have to say they all have brought me to where I am now. I admit there have been times I have been riding an emotional roller coaster, and I think this is to be expected of anyone who is doing a PhD degree. However, feeling down or demotivated was always countered by my inspiring colleagues, and I am sincerely grateful for all your tremendous support.

I first and foremost want to thank my supervisor Erik Folven. You are without a doubt the best mentor I could have asked for. With your excellent knowledge in the field, sense of logic in combination with your down-to-earth modesty, humor and kindness, I can honestly say that without exception I have always left our weekly meetings with a motivation boost. I am going to miss your jokes, anecdotes, and all the discussions on random topics from the gourmet IES coffee, volleyball, lecturing, or anything tech-related in life. For instance, thanks to you, I now consider myself quite competent in fixing car engines (or at least I know what to avoid breaking).

I would also like to thank the two other professors Jostein Grepstad and Thomas Tybell in the oxide electronics group. Your expertise and interest in discussing both the science of the field and everything else has made the days at IES a delight. Thomas, without your exciting Master's project on (111)-oriented oxides, I would never had been where I am today. Also a big thanks to Ingrid Hallsteinsen who guided me through my Master's degree and opened the world of oxides to me.

To all my other colleagues in the oxide electroncs group; Magnus Moreau and Sam Slöetjes, thank you for the joy of companionship for years in the A479 office. Our sharing of knowledge and discussions on everything from memes to paradoxes in quantum physics. Ambjørn Bang and Torstein Bolstad - my friends since starting as nanotechnology students in 2009 - plus Kristoffer Kjærnes and Einar Digernes, the four guys at the end of the hall - thank you for gladly letting me invite myself into your office with a cup of coffee. Anders Strømberg who I have shared office with the last year - your incredibly tidy desk inspires me to occasionally reshuffle my junk in order to keep the working conditions up to HSE standards, especially now during the last months. Runar Dahl-Hansen, our satellite in Oslo, thanks for great companionship at the Nano-network workshops, conferences in San Diego and Boston. Yannis Lever, who enthusiastically worked with me on the VSM, thank you for all the discussions and ideas. Also, to all the other employees at the department of electronic systems and the master students in our group, thank you for all the interesting lunch talks. To the department office, thank you for all help throughout my time here.

A big thanks to NTNUI Volleyball for keeping me as their oldest member for years

during my PhD. The sport, the social environment and the experience as a board member in the group has been a memorable part of my life in Trondheim.

Lastly, I would like to thank my family, my mom Turid, dad Axel, and brother Henning for their endless support. You have always given me freedom in the choices I have made, and supported me on the way. I always say I have my curiosity and interest in science from my dad and the organization and structure from my mom, a combination which is very neat when doing a PhD. I often dream back to the days as a boy drawing and building structures, figuring out how things work and having my small or big projects in my room, dreaming about becoming a pilot, architect, artist or a scientist. I sometimes think it is a bit random that I ended up doing a PhD, but I guess it's really not. I could never have done it without all your support, patience and faith in me.

Papers and manuscripts included in this thesis:

Coexisting spin-flop and exchange bias in $LaFeO_3/La_{0.7}Sr_{0.3}MnO_3$ heterostructures
F.K. Olsen, I. Hallsteinsen, E. Arenholz, T. Tybell and E. Folven.
Physical Review B, **99**, 134411 (2019).

Enhanced magnetic signal along edges of embedded epitaxial $La_{0.7}Sr_{0.3}MnO_3$ nanostructures
F.K. Olsen, A.D. Bang, E. Digernes, S.D. Slöetjes, A. Scholl, R.V. Chopdekar, T. Tybell, J.K. Grepstad and E. Folven.
Journal of Magnetic Materials and Magnetism, **521**(1), 167324 (2021).

Magnetization switching in $LaFeO_3/La_{0.7}Sr_{0.3}MnO_3$ nanoscale heterostructures
F.K. Olsen, Y. Lever, A.D. Bang, J.K. Grepstad, E. Folven.
In preparation

Published papers not included as part of the thesis:

Magnetic domain formation in ultrathin complex oxide ferromagnetic/antiferromagnetic bilayers
A.D. Bang, F.K. Olsen, S.D. Slöetjes, A. Scholl, S.T. Retterer, C.A.F. Vaz, T. Tybell, E. Folven and J.K. Grepstad.
Applied Physics letters **113**(13), 132402, (2018)

Néel vector reorientation in ferromagnetic/antiferromagnetic complex oxide nanostructures
A.D. Bang, I. Hallsteinsen, F.K. Olsen, S.D. Slöetjes, S.T. Retterer, A. Scholl, E. Arenholz, E. Folven and J.K. Grepstad.
Applied Physics Letters, **114**(19), 192403, (2019)

Shape-imposed anisotropy in antiferromagnetic complex oxide nanostructures
A.D. Bang, I. Hallsteinsen, R.V. Chopdekar, F.K. Olsen, S.D. Slöetjes, K. Kjærnes, E. Arenholz, E. Folven and J.K. Grepstad.
Applied Physics Letters **115**(11), 112403, (2019)

Interplay between bulk and edge-bound topological defects in a square micromagnet
S.D. Slöetjes, E. Digernes, F.K. Olsen, R.V. Chopdekar, S.T. Retterer, E. Folven and J.K. Grepstad.
Applied Physics Letters, **112**(4), 042401, (2018)

Crystalline symmetry controlled magnetic switching in epitaxial (111) $La0_{0.7}Sr_{0.3}MnO_3$ thin films
I. Hallsteinsen, E. Folven, F.K. Olsen, R.V. Chopdekar, M.S. Rzchowski, C. B. Eom, J. K. Grepstad and T. Tybell.
Applied Physics Letters Materials, **3**, 062501, (2015)

Direct imaging of long-range ferromagnetic and antiferromagnetic order in a dipolar metamaterial
E. Digernes, S.D. Slöetjes, A. Strømberg, A.D. Bang, F.K. Olsen, E. Arenholz, R.V. Chopdekar, J.K. Grepstad and E. Folven.
Physical Review Research **2**, 013222, (2020)

Contents

Summary v

Preface ix

1 Motivation and background 1

2 Magnetic oxide thin films 7

2.1 The perovskite crystal structure 8

2.2 Epitaxial thin films and heterostructures 10

2.3 Magnetism in perovskites 12

2.4 Magnetic anisotropy 19

2.5 Interface exchange coupling 20

3 Materials system 25

3.1 $SrTiO_3$ 26

3.2 $La_{0.7}Sr_{0.3}MnO_3$ 27

3.3 $LaFeO_3$ 29

3.4 Heterostructures and nanopatterning 31

4 Experimental techniques **33**

4.1 Pulsed laser deposition 34

4.2 Atomic force microscopy 37

4.3 X-ray diffraction 38

4.4 Vibrating sample magnetometry 40

4.5 X-ray absorption spectroscopy 42

4.6 X-ray magnetic dichroism 45

4.6.1 Linear dichroism 45

4.6.2 Circular dichroism 46

4.7 X-ray photo-emission microscopy 47

5 Papers **49**

Author's contribution 51

Paper A 53

Paper B 63

Paper C 71

6 Counclusion and outlook **85**

Chapter 1

Motivation and background

Modern technology as we know it has evolved through a chain of events that started in the first half of the 20th century. Achieving computational power through machines was just a concept at first but once proven to work, it quickly gained momentum and and has been a driving force ever since. After the invention of the field-effect transistor in 1947, the computational power was for a long time governed by the amount of transistors one could fit onto a chip. Since 1965, this development has been described by the well-known Moore's law, which states that the density of transistors on a chip is doubled every two years[1]. Moore's law was just a prediction based on empirical data, but proved to hold for decades. One reason why Moore's law could hold for so long time was that transistors could readily be down-scaled in size. However, the down-scaling and dense packing was ended by eventually reaching fundamental barriers like substantial Joule heating, leading to saturation of clock frequency, or the onset of quantum effects or nanoscale physics such as tunnelling currents which breaks down the functionality of the device. Today, even though we are still heavily using and producing the transistor, it is considered an "old technology" which bottlenecks development of computing power, and there is an immense effort to come up with novel designs which can take over as the leading technology[2].

Spintronics is an emergent field which utilizes the electron spin state rather than its charge, and has potential to replace current[1] nanoelectronic devices[3, 4]. For instance, one aspect of spintronics is utilizing spin-polarized currents which have a majority of one spin state. The magnetic moment of the electron's spin couples to the magnetization of the material, and ferromagnetic (FM) metals with large

[1] pun intended

degree of spin-polarization at the Fermi surface are for instance suited as spin filters. Half-metallic ferromagnets are especially interesting as they have have a $\sim 100\%$ spin-polarized Fermi surface[5]. Utilizing this degree of freedom in addition to the electron's charge harbors great potential in reducing energy consumption of electronic devices[6]. However, novel magnetic memory devices such as spin-transfer torque memory are still facing challenges such as need of high current densities and long writing time[7].

The magnetoresistance (MR) effect, where the resistivity of the material changes with an applied magnetic field, has already been heavily utilized for decades. The relatively weak material-inherent anisotropic MR effect was used in reading heads already in the 1950's, and was later replaced by the larger giant magnetoresistance (GMR). GMR is not a material property, but rather a result of multilayer device design where the resistance is governed by the relative alignment of the magnetization in two FM layers. One layer can be switched while the other is fixed, which is sometimes achieved by exchange coupling to an adjacent antiferromagnet. While the separating material originally was a metal, due to down-scaling, today the current is controlled by tunnelling currents through an insulating barrier. Another type of MR is the colossal magnetoresistance (CMR). This effect was initially discovered in doped manganites in the 1950's[8, 9], but first in the 1990's, epitaxial Ca-doped $LaMnO_3$ was revealed to yield thousandfold change in resistivity[10]. However, the CMR effect has not reached many applications yet due to the requirement of relatively large external fields.

Oxides, and in particular perovskites are interesting materials for new device concepts due to their versatility of functional properties combined with stability in crystal structure [11, 12, 13]. Since cations can be interchanged, doped perovskites have been extensively studied and found to host a plethora of functional phases. Among them, the Strontium-doped manganite $La_{0.7}Sr_{0.3}MnO_3$ (LSMO)[2] holds several intriguing features like a near 100 $\%$ spin polarization of Fermi electrons and a high curie temperature (T_C) of 370 K. The FM order is induced by the double exchange mechanism which strongly couples the conductive and the magnetic properties together, and close to T_C LSMO displays a CMR effect. For these reasons, LSMO has been extensively studied for decades for the purpose of spintronics applications. Bulk properties of LSMO from polycrystalline and single-crystalline samples were mapped in detail by the Tokura group in the 1990's[14, 15]. Much of the the renewed interest at that time came with improved synthesizing capabilities and the discovery in 1987 of a superconducting surface between $LaAlO_3$ and $SrTiO_3$ (STO) in a heteroepitaxial thin film system[16]. As the $LaAlO_3$/STO

[2] In this thesis, we use the abbreviation LSMO for the specific dopant concentration of $x = 0.3$, as this is the material used in all the presented work. Other Sr concentrations are specified.

heterostructure system proved, a property which did not exist in either of the two materials could be produced at their interface. Since this work was done with a relatively simple pulsed laser deposition system, an overwhelming new interest grew in both the oxide synthesis field and around oxides in general. This later became known as the oxide renaissance[17]. Growing strained thin films and heterostructures with monolayer precision unlocked a new tier of their potential, namely tuning the different functional phases by adjusting the crystal structure and chemical composition. For LSMO, the role of epitaxial strain on thin films has been considerably investigated, both by the choice of substrate parameters[18, 19] and crystal orientation[20, 21]. Although several substrates have been shown to enable growth of LSMO, STO is one of the most commonly used due to low lattice mismatch and well-displayed LSMO properties in the films.

The properties of functional oxides can be further modified and controlled by interfacial coupling to adjacent layers. Multilayers and superlattices of LSMO has been investigated extensively, for instance in pursuit of superconductivity[22] or multiferroicity in combination with ferroelectric materials such as $BiFeO_3$ [23] or $BaTiO_3$[24]. LSMO is also known to lose its FM properties below a layer thickness of 4 unit cells, but this has for instance been countered by interface coupling to $La_{0.7}Sr_{0.3}CrO_3$ in superlattice structures[25]. Other magnetic phases such as antiferromagnetism were for long considered to be of little interest in applications, one reason being the difficulty of controlling the Néel axis. Even Louis Néel himself said so while receiving his Nobel price in physics in 1970 for his work on antiferromagnets. However, antiferromagnets have shown usefulness through interfacial coupling due to exchange anisotropy, a feature which is heavily utilized to stabilize domains in magnetic reading heads[26]. Recently, the utilization of antiferromagnets has become one of the hottest fields in spintronics[27]. The magnetization of LSMO has been shown to reorient the Néel axis of a coupled antiferromagnet, opening for Néel axis control which can be notoriously difficult. This was first found in superlattices of LSMO and $La_{0.7}Sr_{0.3}FeO_3$[28, 29], and later also in bilayers of LSMO and $LaFeO_3$ (LFO) [30, 31]. Interestingly, the spin alignment in this heterostructure system is perpendicular at the interface, which is rather uncommon. LFO/LSMO heterostructures are also interesting as a model system since the T_C of LSMO is lower than the Néel temperature (T_N) of LFO, allowing the antiferromagnet to be studied with the FM layer turned "on" or "off".

Furthermore, patterning of thin films has been shown to play a significant role to the domain structure of both single layer LSMO films[32] and LFO films[33], i.e., by shape-induced anisotropy. So far, micro- and nanomagnets of LSMO and LFO/LSMO have primarily been studied as embedded in a surrounding matrix material[32]. While the structuring process has been described, knowledge of the

matrix' effect on the functional properties of the magnets is limited. The effect of a matrix-magnet interface can be expected to become increasingly important as the magnets' dimensions are reduced. Understanding the possible implications of different magnet environments is crucial in order to control the functional properties, but also in regards to distinguish it from other anisotropy effects, like interface coupling to an AF layer.

Combining patterning with heteroepitaxy, magnetic switching properties of micromagnet bits patterned on LFO/LSMO bilayer films was investigated by Folven et al. and found to give reduced coercivity as compared to single layer LSMO thin films[34]. This is an interesting finding since the addition of an AF layer usually leads to enhanced coercivity. Takamura et al. also found remnant domain states in LSMO square micromagnets which could only be supported theoretically under an applied field, and suggested an exchange bias could be present at the (001) LFO/LSMO interface [31]. However, no evidence of a net moment on Fe in LFO could be detected. A FM moment on Fe was later discovered both in (001) and (111)-oriented LFO/LSMO, but which followed the rotation of LSMO moments and therefore gave no exchange bias[35, 36, 37].

Aim of the thesis

In this work, we focus on the interface physics of the epitaxial LFO/LSMO heterostructure system and the effect of micro- and nanoscale lateral patterning specifically with respect to the magnetic properties. The work is therefore branched into two categories; the effect of the interface and the effect of patterning. Importantly, in order to correctly distinguish the effects, they have to be investigated separately.

The first part of the work is therefore dedicated to growth and characterization of thin films and heterostructures. We study ultrathin layers of LSMO and LFO and vary the LSMO thickness in order to closer investigate the coupling at the interface and its effect on the magnetization in each material. Specifically, we examine both the macroscopic and element specific magnetization by the use of magnetometry measurements and synchrotron radiation.

The second part of the work entail patterned films and heterostructures in the micro- and nanometer size regime. Here, we examine and compare the effect of having a surrounding matrix and having no matrix, i.e., free-standing magnets. Specifically, we investigate differences in the nanomagnets' crystal structure by x-ray diffraction and their magnetization by magnetometry.

The thesis is outlined as follows; In the following chapter 2, a brief establishment of theory on perovskite oxides is given, first with emphasis on the crystal structure and then the electronic and magnetic structure. In chapter 3, the materials system

used in this work is presented and relevant state-of-the-art features are discussed. Chapter 4 presents the different experimental techniques and methods which have been used. In chapter 5, an overview of contribution from coauthors is declared for all work which has been published, and the published articles and manuscript are presented. Finally, the conclusion and outlook is given in chapter 6.

Chapter 2

Magnetic oxide thin films

In this chapter, first the structural aspects of perovskites will be outlined for bulk systems in 2.1 and then discussed for thin film systems in 2.2. Then the electronic structure and emergent magnetic properties will be discussed in 2.3.

2.1 The perovskite crystal structure

Perovskites are a class of oxides with a chemical formula ABO_3. The B sites are occupied by transition metal cations which form bonds to six oxygen and make up corner-sharing octahedra, while the A sites are dodecahedral voids, occupied by rare-earth or transition metals – see Fig. 2.1 (a). While the oxygen anion charge is fixed to -2 due to strong electronegativity, the remaining positive charge required for neutrality is distributed on the A- and B-cations. This gives room for flexibility in oxidation states for the transition metals, which is one of the reasons the perovskite structure is able to host a variety of element compositions. The geometric structure is also flexible to different sizes of the ions. However, the variation of elements can lead to structural deviations from an ideal cubic symmetry seen in Fig. 2.1 (b-d).

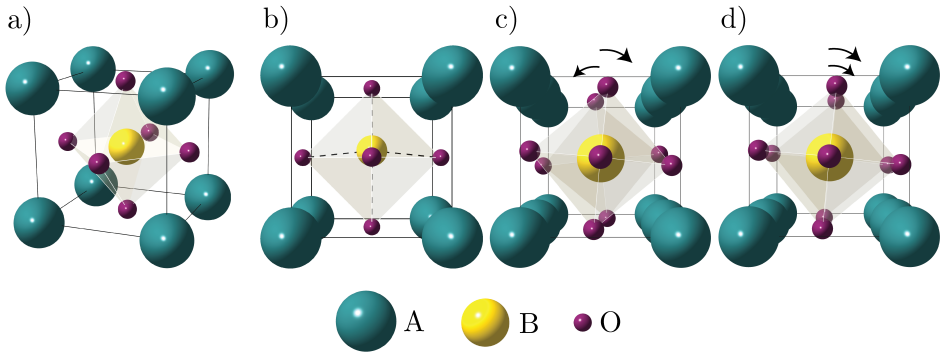

Figure 2.1: The perovskite crystal structure with modifications arising from non-ideal ionic sizes. a) shows the unit cell for ideal cubic symmetry. b) shows a unit cell with tetragonal distortion following $t > 1$ with off-center stabilization of the B-cation. In c) and d), two unit cells are shown along the a axis to illustrate out-of-phase and in-phase rotations - possible outcomes from $t < 1$. c) shows an $a^-b^0b^0$ rotation pattern and d) shows an $a^+b^0b^0$ rotation pattern.

Structural deviations

Non-ideal ionic sizes in this geometric framework can be expressed by the Goldschmith tolerance factor t [38]. It relates how the ionic radii r_A, r_B and r_O influence the lattice parameter, and gives an indication of how the structure will distort:

$$t = \frac{r_A + r_O}{\sqrt{2}(r_B + r_O)} \tag{2.1}$$

When the ionic radii deviates from what gives the ideal ratio $t = 1$, the struc-

ture compensates by cation displacements or tilting of the BO_6 octahedra, both of which reduces the crystal symmetry. For $t > 1$ the B-cations are relatively smaller, and the bond lengths inside the octahedra can become unfavorably long. As a result, the B-cations can rather stabilize in off-center positions, as illustrated in Fig. 2.1 (b). In this situation, the space charge distribution become non-centrosymmetric, which gives rise to the dipolar moment in many ferroelectric perovskites. In the case of $t < 1$, the A cations become relatively small and the BO_6 octahedra can start to rotate. This is driven by the A cation coordination number optimization [39, 40]. Such octahedral rotation distortions can distribute among all three principle axes, and consequently the B - O - B bond angles will deviate from 180°. The common nomenclature for these rotations is given by the Glazer notation system [41] where the three principle axes are labeled a, b, or c. If the magnitude of rotation is equal along two axes, they are given the same letter. The letters are accompanied by superscripts that describe rotation out-of-phase (-), in-phase (+) or no rotation (0). Out-of-phase and in-phase rotations correspond to whether the chirality of rotation along the respective axis is staggered or synchronized, as shown in Fig. 2.1 (c) and (d).

Glazer found that the combination of different rotations constitutes 23 unique tilt patterns in the perovskite structure [41], which due to symmetry equivalence span over 15 different space groups. The cubic structure in Fig.2.1(a) is the smallest possible unit cell, and deviations requires a large unit cell to properly describe the symmetry. It can often get confusing when working with perovskites that are very similar in structure but belong to different symmetry groups since for each group, lattice parameters describe different directions in space but are still labeled a, b or c. Therefore, when working with different perovskites, like in heterostructure systems, it is common to address their lattice parameters in pseudocubic terms, referring to the lattice constants of a single ABO_3 cell. In this thesis and the published works, pseudocubic parameters are used for simplicity unless stated otherwise.

2.2 Epitaxial thin films and heterostructures

The flexibility of the perovskite structure makes it well-suitable for growing epitaxial thin films and heterostructures. However, thin films grown onto substrates are subjected to a structural conflict when there is a lattice mismatch. Since the film will be mechanically clamped to the substrate, both strain and symmetry restrictions from the substrate will be applied. With these modifications new distortions may arise, altering the structure from its bulk ground state. This is the essence of strain engineering, which for perovskite materials have been researched extensively for decades [42].

Epitaxial strain

A film material with larger or smaller lattice parameters than the substrate will be exerted to in-plane compressive or tensile strain respectively. The imposed strain can be withstood up to a critical thickness upon where the film starts to relax by introduction of dislocations, [43] as shown in Fig. 2.2. For films below the critical thickness, the whole film remains epitaxially strained. Perovskites can accommodate epitaxial strain by structural distortions, similar to the ones found when the tolerance factor is non-ideal, e.g., bond elongation and octahedral rotations.

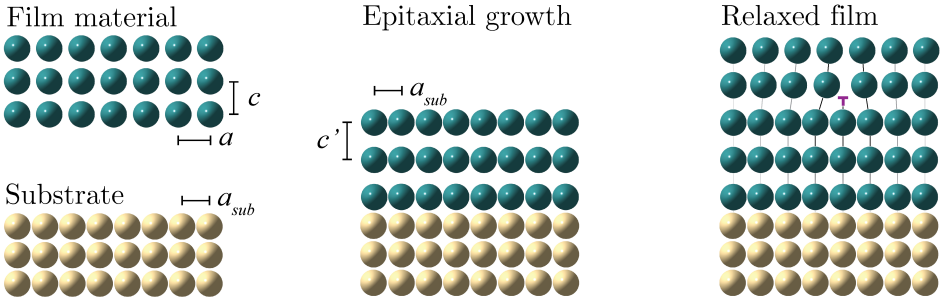

Figure 2.2: Epitaxial strain illustrated for a thin film material and substrate with slight difference in lattice parameters a and a_{sub}. Below the critical thickness, the film lattice parameters adjust to that of the substrate (a_{sub}) in-plane with compensation (c') out-of-plane. For a relaxed film, a line dislocation is shown as an example of crystal defect. B cations and oxygen anions are omitted for better visualization.

Bond length distortions

Epitaxial strain only restricts in-plane lattice geometry. While the B-O bond lengths are shortened in-plane by compressive strain, and elongated in-plane by tensile strain, the structure can compensate along the perpendicular direction. Epitaxial films can thus get new symmetry imposed by the substrate, and new functional

phases may follow. One example is STO, which in bulk crystallizes in the cubic structure. Asymmetric distortion to the crystal structure was predicted by Pertsev et al. to cause B-cation displacement along the elongated axis, leading to ferroelectricity [44]. This was later proved experimentally in tensile strained $SrTiO_3/DyScO_3$ [45].

Octahedral rotations

Theoretical analysis has indicated that under compressive strain, increased tilting is favored around the out-of-plane axis to help maintaining the B-O bond lengths, at the cost of decrease in in-plane rotations. Likewise, the opposite is favored for tensile strain, i.e. increased tilting around in-plane axes, see Fig. 2.3. This was demonstrated to be favored in systems both with out-of-phase rotations [46, 47] and in-phase rotations [48]. Furthermore, a rotation pattern can be imprinted into the film from the substrate [42, 49]. When the tilt pattern does not match at the interface, such as if an in-phase rotation pattern meets an out-of-phase rotation pattern, a structural reconstruction must occur to uphold octahedral connectivity. This geometric frustration was tested by Liao et al [50] by growing rhombohedral $La_{2/3}Sr_{1/3}MnO_3$ ($a^-a^-a^-$) onto orthorhombic $NdGaO_3$ ($a^-a^-c^+$) and ensuring the in-phase rotation axis was in-plane. What they found was that the film fully inherited the substrate tilt pattern, and the larger tilt angle of $NdGaO_3$ decreased over a 4 unit cell long transition region into the $La_{2/3}Sr_{1/3}MnO_3$ film. Furthermore, they found that by implementing a $SrTiO_3$ buffer layer of only 1 unit cell, the transition region could be removed while maintaining the $NdGaO_3$ in-plane lattice parameter.

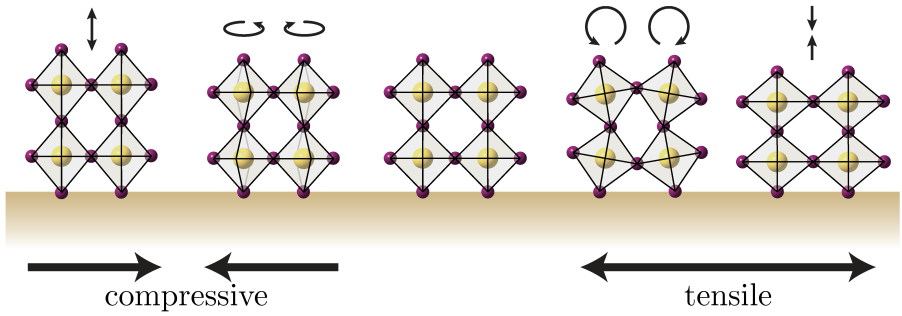

Figure 2.3: Typical modifications of the perovskite structure due to compressive (left) and tensile (right) strain. For compressive strain, bond elongation out-of-plane and octahedral rotations around the out-of-plane axis are shown. For tensile strain, octahedral rotations around an in-plane axis and bond shrinking out of plane is shown. The A cations are omitted in the figure for better visualization.

2.3 Magnetism in perovskites

In solid materials, magnetic moments arise from mainly two sources – the electron spin s and the electron orbital momentum l. Still, not all materials show magnetic response due to that most electrons are paired with opposite spins and thereby cancel each other's moments. Unpaired electrons may be found in orbital states near the Fermi level, which in perovskites typically are the partially filled d-orbitals on the B cation.

Electronic structure

The five hybridized d-orbitals on the transition metal labeled d_{xy}, d_{xz}, d_{yz}, d_{x2-y2} and d_{z2-r2} are degenerate for a single atom, and electrons spread out in accordance with Hund's rules. However, positioned in the octahedral site in the perovskite structure, the orbitals are strongly affected by the ligand field and split into t_{2g} and e_g states. This crystal field splitting arises due to the energetic preference of electrons to occupy orbitals that do not point directly towards the oxygen anions (e_g), but towards the octahedra facets (t_{2g}), see Fig.2.4. The magnitude of the field splitting will be competing with the electron pairing energy, and therefore directly affects the net number of unpaired electrons S. For example the cobaltites are d^6, and $LaCoO_3$ is in a low spin state (t_{2g}^6 and $S = 0$) and does not have magnetic moments at low temperatures [51]. Conversely, The orthoferrites are d^5 and in a high spin state ($S = 5/2$) and yields one of the largest atomic magnetic moments in perovskites [52].

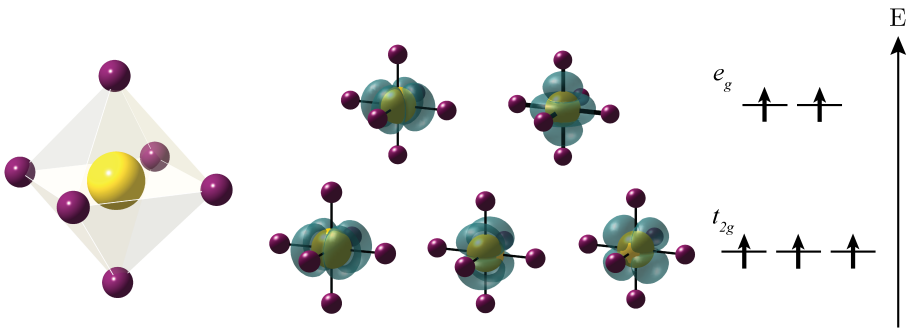

Figure 2.4: Geometric configuration for cation d-orbitals in octaheder positions. The crystal field energy splitting is illustrated to the right, with a d^5 high spin configuration as example.

Magnetic order

Symmetric exchange

The magnetic long-range order such as ferro-, ferri- or antiferromagnetic arises with inter-atomic exchange interactions which is classically described by the Heisenberg model. The exchange coupling J can favor parallel ($J > 0$) or anti-parallel ($J < 0$) alignment of neighboring atomic moments S_i and S_j, leading to long-rang ferro- or antiferromagnetic order respectively. The Hamiltonian for the system is then:

$$H = \sum_{i,j} -J\vec{S_i} \cdot \vec{S_j} \tag{2.2}$$

In perovskites, the sign of J is dictated by a hierarchy of ligand-mediated exchange interactions, i.e, the B-cations interact via the $2p$ orbitals of the oxygen anions. The oxygen $2p$ orbitals are filled, and therefore no electron exchange should be favored by the oxygen. Important theoretical work on these interactions was done by Kramer and later revised by Anderson [53], Goodenough [54] and Kanamori [55]. The Goodenough-Kanamori rules have become a framework for predicting the magnetic order in oxides with various oxidation states. Different orbital interactions which can occur are discussed in the following, and visualized in Fig. 2.5.

Virtual superexchange, meaning no electrons are actually transferred, is first illustrated in Fig. 2.5 a). A half-filled d-orbital will form σ bonding with the oxygen $2p$ and the electrons will in accordance with the Pauli exclusion principle be anti-parallel aligned. On the opposite side of the anion, the other oxygen $2p$ electron interacts with the other metal cation, and the net resulting magnetic order on the metal cations is antiferromagnetic. Intra-atomically on each cation, the spins in t_{2g} states are aligned by Hund coupling. AF order is also promoted by π-interactions between half-filled t_{2g} orbitals, as illustrated in Fig. 2.5 b). In the case of empty e_g orbitals, as shown in Fig. 2.5 c), the oxygen $2p$ forms a semi-covalent bond with the empty states, and the oxygen $2p$ electron participating in that bond couples to the t_{2g} electrons on the cation. Also in this situation, the resulting order is AF. Of the three abovementioned types of superexchange interactions, covalent σ-bonding is the strongest, which has a direct effect on the ordering temperatures in antiferromagnetic perovskites governed by the different mechanisms[56]. A case of unevenly filled e_g orbitals ($t_{2g}^3 e_g^1$) is shown in Fig. 2.5 d). Two types of superexchange mechanisms can then occur when one e_g orbital is half full and the other empty, depending on the geometric orientation of the half-filled orbitals on two

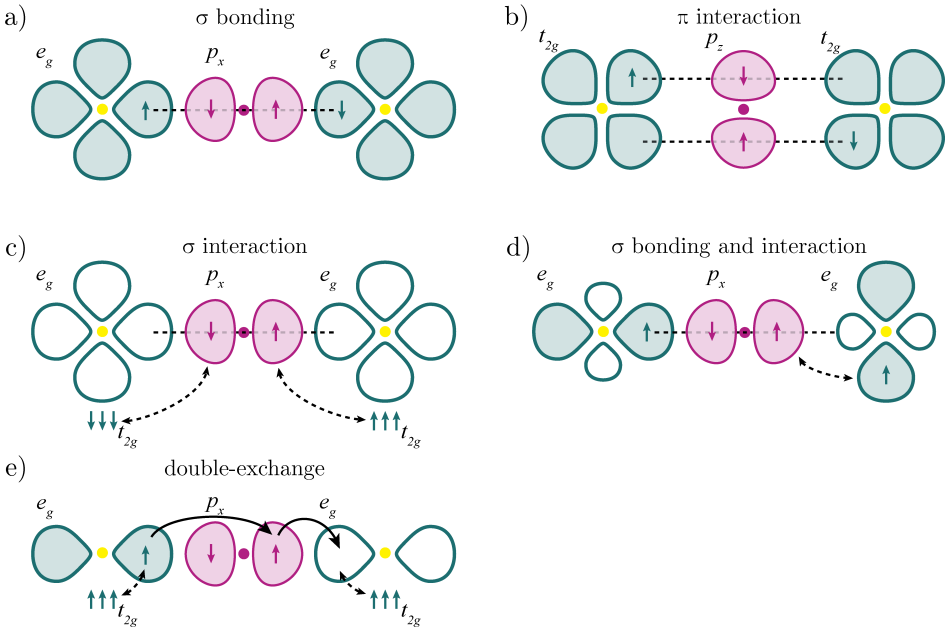

Figure 2.5: Illustration of different exchange interactions between metal cations (green orbitals) mediated by oxygen (purple orbitals) in perovskites. a)-d) shows different types of superexchange interactions. e) shows the double-exchange interaction.

nearby metal cations. If they are aligned (not shown), antiferromagnetic order will be favored through σ-bonding, similarly as in a). However, if they are staggered (90°) as shown in d), the oxygen $2p$ orbital will on one side form a σ bond with the empty e_g orbital causing antiparallel alignment, and on the other end σ interaction will favor parallel alignment through Hund coupling. The net resulting magnetic order is in this case FM. Such staggered orbital alignment can arise by the Jahn-Teller effect [57], which is an asymmetric distortion to the octahedra following uneven electron distribution. In the e_g^1 situation, the half-filled orbital will elongate in order to lower its energy, while the unfilled orbital will contract. This lowers the total energy at the cost of both orbital degeneracy and crystal structure symmetry. The structural distortion can be minimized by staggered order, as is the case with $LaMnO_3$. In $LaMnO_3$ ($t_{2g}^3 e_g^1$), the e_g electrons populate the orbitals in the ab plane, leading to FM order by superexchange interaction shown in 2.5 d). The empty e_g orbitals pointing out-of-plane leads to AF order. This leads to FM planes stacked in an antiparallel order, also called *A*-type AF ordering. The other types often encountered in perovskites are *C* and *G*-type, as shown in Fig. 2.6. As another example, in LFO the Fe ions are $3d^5$ and high spin, implying all d-orbitals are half-filled. This leads to strong AF order in all bond directions and consequently *G*-type AF order.

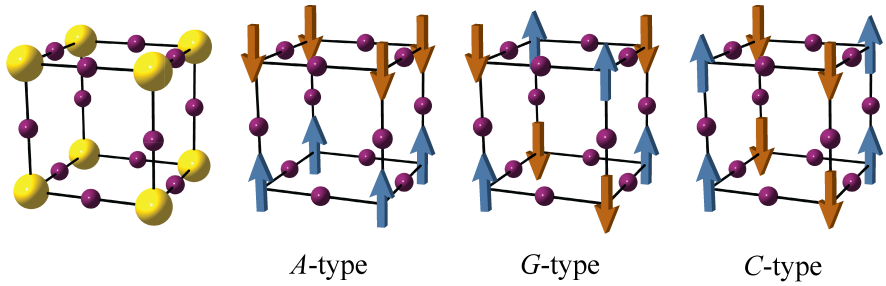

Figure 2.6: Different antiferromagnetic orderings in perovskites resulting from combinations of exchange mechanisms between magnetic B cations (yellow).

Non-integer oxidation states can be realized on the B cations by doping, in which case double-exchange interaction can facilitate both ferromagnetic order and electron itineracy causing a metallic state [58]. Fig. 2.5 e) shows the example of $e_g^{0.5}$, simplified in the illustration as e_g^1 and e_g^0 on nearby metal cations. These ordered oxidation states are energetically unfavored, and the oxygen allows the e_g electron to instead delocalize over the two cations by hopping through the $2p$ orbital. Thus, the energy gain also causes electron itineracy. Due to Hund coupling of the e_g spin with the t_{2g} electrons on each metal cation, the same spin state is favored on all cations, resulting in FM order.

The strengths of the interactions are strongly affected by the B-O-B bond overlap and angles. Therefore, structural distortions such as octahedral rotations can be expected to influence the magnetic properties. The effect of bond angle differences on magnetic properties is for instance seen in orthoferrites by varying the rare-earth A cation, $RFeO_3$. With increasing size of the R^{3+} ion from Lu to La, Fe-O-Fe bond angles increase ($142° - 157°$), giving stronger interaction which is displayed by the increase in Néel temperature of 620-740 K [59].

Magnetoelectric coupling and asymmetric exchange

Materials with more than one ferroic order coexisting in the same phase are called multiferroics. When both the magnetic and electric types of ferroic order are cross-coupled, i.e., adjusting one property will have influence on the other, the material is magnetoelectric. Such materials have been sought for in recent decades due to their potential in electronic devices where there is high interest to be able to control magnetization by an electric field, and vice versa. One type of magnetoelectric coupling is the asymmetric exchange. Dzyaloshinskii [60] found that a cross-linking interaction term between two neighboring spins favorizes non-parallel spin alignment, in contrast to the previously discussed direct exchange interaction J. Moriya [61] thereafter supplied that the driving force for the interaction is closely linked to the crystal symmetry, and that the term only becomes considerate in crystals with lowered symmetry. The Dzyaloshinskii-Moriya interaction (DMI) was originally used to explain the occurrence of weak ferromagnetism due to spin canting in antiferromagnets, but it can also for instance explain stabilization of spiral spin textures or skyrmions. In systems that can accommodate DMI, a term is added to the total Hamiltonian so that it becomes:

$$H = \sum_{i,j} -J\left(\vec{S}_i \cdot \vec{S}_j\right) + \vec{D}_{i,j}\left(\vec{S}_i \times \vec{S}_j\right) \tag{2.3}$$

where D_{ij} is the DM vector. While the direct exchange term favors parallel alignment, the energy gain from the DMI term is maximized when the spin moments are perpendicular. However, the asymmetric exchange is weak and is typically only capable of causing small spin canting in competition with the direct exchange [61]. In the perovskite crystal structure, the DM vector's direction and magnitude is dependent on the position of the oxygen anion, given by

$$\vec{D}_{i,j} \propto \vec{r}_O \times \vec{r}_{i,j} \tag{2.4}$$

where r_O is the offset of the oxygen from the direct line r_{ij} between magnetic

ions as shown in Fig. 2.7. $\vec{D}$ can therefore be directly linked to the presence of octahedra rotation distortions.

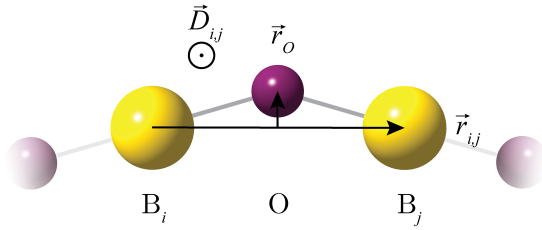

Figure 2.7: Relation between oxygen offset $\vec{r_o}$, metal cation separation $\vec{r_i, j}$ and the DM vector $\vec{D_{i,j}}$ in perovskites due to octahedral rotations.

Due to the corner connectivity of octahedra and staggered pattern, the spin canting will be also be staggered, as illustrated in Fig. 2.8(b). Therefore, in ferromagnets, any net moment arising perpendicular to the FM axis is cancelled out. However, the additional staggered spin structure of antiferromagnets can potentially lead to a net moment arising perpendicular to $\vec{D}$ and the Néel axis.

When further considering (1) different types of AF order and (2) different octahedra rotation patterns, many combinations of these will lead to a cancellation of any FM moment arising from spin canting. For example, with AF order along an in-phase rotation axis, as illustrated along the z-axis in Fig. 2.8(c), the FM moment arising from canting is cancelled out in the xz plane. On the other hand, out-of-phase rotations and AF order, or in-phase and FM order can lead to a net moment (not shown). Therefore, a *G*-type antiferromagnetic order and an $a^-a^-a^-$ rotation pattern will cause no intrinsic cancellation of the moment arising from spin canting. However, even when weak ferromagnetism is present, the net macroscopic moment may still be suppressed. For example, in antiferromagnetic $BiFeO_3$, spin canting causes weak ferromagnetism but the small net moments form cycloid patterns with a period of 62 nm, resulting in zero net macroscopic moment [62, 63]. For *G*-type antiferromagnet with different tilt pattern, such as LFO which has $a^-a^-c^+$, there may exist planes in the lattice with net magnetic moments even though the macroscopic net moment is cancelled. Such a plane is illustrated in Fig. 2.8(d).

Domains

In ferromagnets, the exchange interaction alone favors a single magnetic domain where all moments are aligned. However, this would lead to maximization of the net magnetization and therefore also a large generated demagnetizing field. The

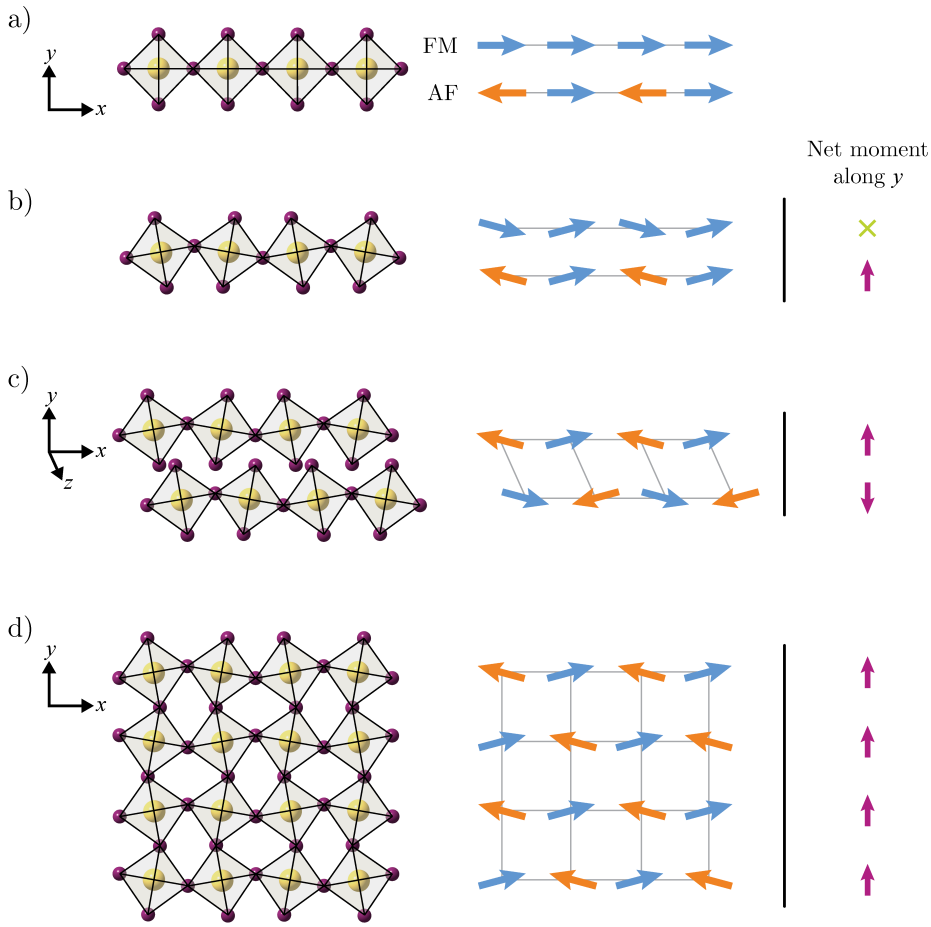

Figure 2.8: Illustration of canting of magnetic moments in perovskites due to octahedra rotations and Dzyaloshinskii-Moriya interactions. a) shows the example spin structure for a ferromagnetic and antiferromagnetic order along x with no octahedra rotations. b) shows octaheder tilting and resulting spin canting for ferromagneticcally and antiferromagnetically ordered spins along x.

magnetostatic energy which arises due to the magnetization's interaction with this field, and therefore the magnetization breaks up into domains. Between neighboring domains, there is consequently a region called domain walls where moments rotate. The rotation comes at a cost of exchange interaction energy, but energy gain by lowering the total magnetostatic energy. Since the dominating cause for domain formation is lowering of magnetostatic energy, intuitively, antiferromagnets could be expected not have domains. However, antiferromagnet are often found to have complex domain patterns. The reason for domain formation in antiferromagnets is therefore believed to be due to imperfections in the crystal structure, e.g., structural domains and defects which disrupt the energy locally.

2.4 Magnetic anisotropy

Magnetic anisotropy is the favoring of the magnetization to lie along certain geometrical directions. In the following, different contributions to anisotropy in magnetic materials are discussed. Magnetic anisotropy effects related to interface coupling will be discussed in chapter 2.5.

Magnetocrystalline anisotropy

In crystalline magnetic materials, the magnetization tends to prefer lying along certain crystalline directions (easy axes) more than others (hard axes). This phenomenon is termed magnetocrystalline anisotropy and is a 'fingerprint' of the orbitals' spatial distribution and their interaction with the surrounding crystal structure. Under applied external magnetic fields, electrons with their spin and orbital angular momentum want to lower the interaction energy by reorienting their spin directions. However, they are connected to the orbitals by spin-orbit coupling, and the hybridized orbitals are in turn bound to the lattice geometry. The energy associated with magnetocrystalline anisotropy is generally defined as the energy required to rotate the magnetization from an easy axis into a hard axis. Therefore, in many cases it will be the energy of overcoming the spin-orbit coupling [64]. Typically, materials with strong spin-orbit coupling display the strongest magnetocrystalline anisotropy. Crystal symmetry will always be reflected in the magnetocrystalline anisotropy, and materials with high symmetry display low anisotropy [64, 65]. For example, the magnitude of magnetocrystalline anisotropy for simple ferromagnetic metals like Co, Fe or Ni are on the order of 10^5 erg/cm^3 [66]. For thin films, this energy is easily outweighed by other anisotropy terms induced by shape or strain.

Shape anisotropy and surface environment

For highly anisotropic shapes of materials, e.g. rods or films, the magnetization tends to follow the geometry of the material – an effect known as shape anisotropy. This happens due to the lowering of the magnetostatic energy when most moments

are aligned parallel to the surface. For example in thin films, due to the high anisotropic shape, it is energetically preferable for the the magnetic moments to lie in the film plane [67]. However, there may be other anisotropy terms which can dominate. For example, at the very surface, the crystal truncation imposes a broken symmetry environment to the atoms. The anisotropic surroundings cause surface atoms to have altered electronic structure, an effect which can become important as the film gets very thin. The monolayer at the very surface may have a strong favorization of the orbital angular momentum to be in-plane. If there is strong spin-orbit coupling, the electron spin will be directed out of plane. Such perpendicular anisotropy, first described by Néel in 1954, is termed surface anisotropy[66, 67].

Magnetoelastic anisotropy

The magnetization direction in a material may show anisotropic effects from strain. This effect, discovered in 1842 by Joule is called anisotropic magnetostriction and can be described by the strain observed at saturation magnetization, $\lambda_S = \Delta l/l$. The reverse effect is also of significant importance, namely stress-induced magnetic anisotropy. For materials with $\lambda_S > 1$, magnetization is easier in the tensile stress direction, and vice versa [66]. For instance, Berndt and Suzuki studied (001)- and (110)-oriented films of LSMO grown on STO [68, 69, 20]. The epitaxial films were found to have significant altered anisotropy from single crystals and the change was correlated to the symmetry of the substrate lattice. (001)-oriented films showed in-plane $\langle 110 \rangle$ easy axes and $\langle 100 \rangle$ hard axes, suggesting cubic anisotropy inherited from the substrate. (110)-oriented films showed uniaxial anisotropy along the in-plane [110] axis which indicate domination of magnetoelastic effects imposed by in-plane strain due to lattice mismatch.

2.5 Interface exchange coupling

The long-range magnetic order, governed by J as discussed in chapter 2.3, is disrupted at the interface in magnetic heterostructures. While the Goodenough-Kanamori rules give an interpretation of magnetic order in perovskites, the exchange coupling J_{int} across heterointerfaces is not straight forward to predict. In the following, we focus on AF/FM interfaces specifically.

Spin-flop

Considering an AF/FM interface with a spin-compensated plane on the AF side and spin-polarized plane on the FM side, an equal number of parallel and antiparallel spin alignments will be present. Koon [70] showed by micromagnetic simulations based on a Heisenberg model, that the energetically preferred alignment at such interfaces is a perpendicular, or so-called spin-flop state, where the ferromagnet aligns its moments 90° to the Néel axis of the antiferromagnet – see Fig. 2.9.

Most AF/FM interfaces are although reported to display collinear alignment of AF and FM spins which is believed to be due to that most interfaces are not perfectly spin-compensated and that only small deviations can cause a transition to collinear alignment [71].

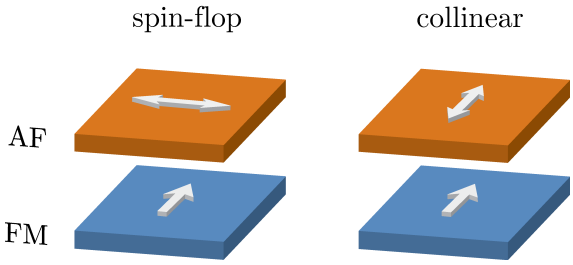

Figure 2.9: Illustration of spin-flop and collinear coupling between an antiferromagnetic and ferromagnetic spin lattice.

Enhanced coercivity

While the AF spin lattice is robust and remains unaffected by relatively large magnetic fields, an exchange coupling can impose significant increase to the coercivity of the FM layer, sometimes referred to as ferromagnetic enhancement. This enhanced coercivity is attributed to that the coupled AF spin lattice has to rotate together with the FM during switching [72, 73]. This effect can be expected as long as there is a strong exchange coupling between the two layers.

Exchange bias

A unidirectional bias can arise at AF/FM interfaces, i.e., the FM layer obtains a preferred magnetization direction. This effect, known as exchange bias (EB), manifests as a shift of the FM hysteresis curve along the field axis – see Fig.2.10. Because its occurrence requires exchange interaction with an AF, the effect is often just referred to as exchange anisotropy. EB was discovered and reported for the first time, in 1956 by Meiklejohn and Bean [74], to occur in FM cobalt particles coated with AF cobalt oxide. Since the discovery, the EB effect been reported in numerous AF/FM systems, including small particles, inhomogeneous materials and thin film heterostructures, where the latter has been the most widely studied group [73, 75]. Since it can be utilized to pin the magnetization direction of FM layers, EB is heavily utilized in spintronic applications [71, 72, 75], e.g., for domain stabilization in magnetoresistive reading heads [26] and pinning a hard FM layer in spin valves [76, 77].

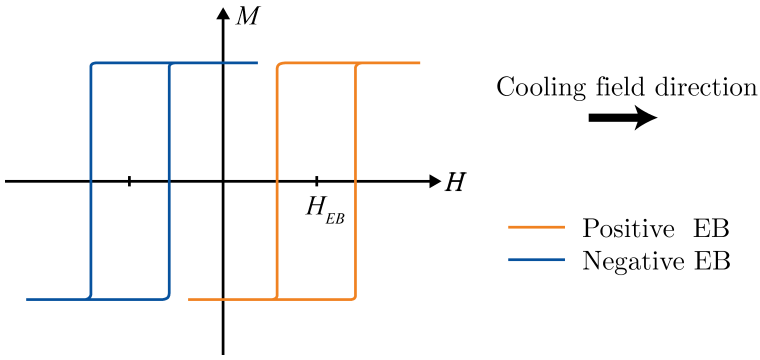

Figure 2.10: Manifestation of exchange bias by a shift of the ferromagnetic hysteresis curve along the field axis. The direction of the shift is termed relative to the direction of the cooling field.

Driving mechanism

The driving mechanism for EB was early proposed to be the presence of a net moment in the AF layer which couples to the FM layer via exchange interactions [71]. EB is most commonly found by applying a magnetic field while cooling the materials through the T_N of the antiferromagnet, a process termed field cooling. During cooling through T_N, some magnetic moments in the AF are pinned ferromagnetically in the cooling field direction as the AF spin lattice orders [78]. Consequently, such "frozen moments" perturb the otherwise spin-compensated AF interface layer and can give a bias to the adjacent FM. More recently, EB has for some systems been reported to occur without the necessity of field cooling, therefore termed zero-field cooled EB, or spontaneous EB [79, 80]. In the last 10 years, spontaneous EB has been reported in an increasing number of perovskites where in most cases a spin glass state is believed to be responsible, for example in $BiFeO_3$ nanocomposites [81], $YMnO_3$ nanoparticles [82], polycrystalline $La_{1-x}Sr_xCo_yMn_{1-y}O_6$ [83, 84], and $Eu_{0.9}Pr_{0.1}CrO_3$ [85] and also recently in epitaxial heterostructures of LSMO/$Eu_{0.45}Sr_{0.55}MnO_3$ [86].

Thin film theoretical model

There are many theoretical models that have been developed to explain EB in various materials systems. Most are based on the original work by Meiklejohn and Bean [74, 87, 78]. For thin films, it is customary to model the magnitude of the EB in terms of interface energy per unit area, σ_{int}:

$$\sigma_{int} = M_{FM} t_{FM} H_E \tag{2.5}$$

Here, M_{FM} is the saturation volume magnetization, t_{FM} is the ferromagnet thickness and H_E is the exchange bias magnitude. Common values for oxides are in the range 1 μJ/m^2 – 3.5 mJ/m^2 [73, 71] while theoretically, a perfect uncompensated interface would yield $\sim$10 mJ/m^2 [88]. As the model shows, EB is inversely proportional to the FM layer thickness. Hence, EB can be expected to emerge when the FM layers get thin. The interface energy can further be expressed in terms of a Heisenberg model which incorporates the direct exchange energy at the interface:

$$\sigma_{int} = J_{int}\vec{S}_{AF} \cdot \vec{S}_{FM}/a_{AF}^2 \tag{2.6}$$

Here, $\vec{S}_{AF}$ and $\vec{S}_{FM}$ are the AF and FM spin moments connected at the interface and a_{AF} is the unit cell area of the AF [88].

Influence of interface irregularities

EB is reported to be highly influenced by structural irregularities at the interface. This can be understood as any structural disorder will cause changes to the energy landscape. Examples of disorder are interface roughness or impurities [89]. However, over 60 years of research has revealed that there is no infallible trend with disorder, implying that the inherent origin of EB and the influence of structural disorder must be investigated specifically for each system. This has led to an immense pool of EB literature, but luckily also some well-written reviews covering broad parts of the research [71, 72, 73, 75, 90]. As an example of the complexity, interface roughness is reported to lead to a decrease the magnitude of EB for polycrystalline films, but increase the magnitude in single crystals. However, there are also examples of opposite behaviour. Furthermore, there is no clear correlation between roughness and the degree of inherit spin-compensation at the AF interface layer [73]. This can be understood for spin-compensated AF interface layers since roughness should on average expose the same number of opposite moments in the AF layer. On the other hand, the maximum EB would be expected for a fully uncompensated (fully spin-polarized) AF interface layer, and any roughness should decrease the magnitude. Uncompensated spin planes at the interface can for instance be obtained by choosing the right crystal orientation, but this has not been found to necessarily grant EB [37, 89, 91]. Ultimately, it is important to note that the picture is complicated because interface roughness likely influences the exchange coupling J_{int}.

Horizontal and vertical shifts of the hysteresis loop

The most common observation of EB is a shift in the opposite direction as the cooling field, which therefore is termed negative EB. This is illustrated in Fig. 2.10. A common assumption is that the exchange coupling J_{int} is stronger than

the Zeeman energy of the FM, and hence small cooling field strengths will align the FM moments while the AF moments will be governed by the exchange coupling energy J_{int} as they freeze in. It is not necessarily straight-forward to predict the sign of J_{int}. Even when knowing the sign and strength of J in each separate layer, the environment at the interface can influence the exchange interaction significantly. For instance, even FM/FM bilayers have shown to favor antiferromagnetic interface exchange [92]. It can also prove difficult to identify the sign of J_{int} experimentally for AF/FM systems. However, if the amount of pinned AF moments is large, a vertical shift could potentially be observed in the hysteresis loop. A positive vertical shift could imply that both the FM and the AF are aligned parallel with the cooling field, indicating that $J_{int} > 0$. Likewise, a negative vertical shift could indicate $J_{int} < 0$. Unfortunately, vertical shifts are not always observed, as only a small number of pinned moments is necessary to yield a large bias [88]. Furthermore, very strong cooling fields can overcome J_{int}, in which both layers will be parallel aligned with the field during the cooling process. However, if $J_{int} < 0$, the FM moments can flip back as the field is removed, which would result in a positive EB. This explains how some AF/FM systems may show field-dependent change of sign in EB, which has been found in several systems, for instance epitaxial $La_{0.3}Sr_{0.7}FeO_3/SrRuO_3$ heterostructures on (001)-oriented $SrTiO_3$ [93] or polycrystalline $La_{0.5}Sr_{0.5}Co_{0.2}Mn_{0.8}O_3$ [84].

Blocking temperature

EB is found at low temperatures and usually decreases for higher temperature. Often, EB is found to disappear above a temperature called the blocking temperature T_B. Many studied AF/FM systems exhibit a larger ordering temperature for the FM than the AF, i.e., $T_C > T_N$ [73], which allows observing the FM with and without the AF layer turned “on”. In such systems, T_B often coincides with, or is found close to T_N, but it can also occur at significantly lower temperatures.

Chapter 3

Materials system

In this chapter, an overview of the materials used in the experimental work is presented. For the materials used as epitaxial thin films in this work, both bulk properties and epitaxial properties on STO are discussed. Finally, a brief overview of relevant published works on the LFO/LSMO heterostructure system is given.

3.1 $SrTiO_3$

STO is a perovskite with ideal cubic structure at room temperature. Due to the ability to control its surface structure with atomic precision during growth, it has great potential as a substrate for epitaxial thin films and heterostructures [94]. The alternating (001) planes (TiO_2/SrO) are polar, which makes it desirable for conductive interfaces. Particularly after the superconductive interface was found for epitaxial heterostructures of $LaAlO_3$ on STO, it became widely used as a substrate material for oxide thin film growth [95].

At 105 K, STO undergoes a structural phase transition to tetragonal (low temperature phase), which occurs due to phonon softening [96]. The TiO_6 octahedra rotate around one axis which is expanded, while the other two contract. This has been shown do cause modifications to the magnetic properties of epitaxial films of LSMO with thickness up to 220 nm [97].

STO is a band insulator ($E_g = 3.25$ eV), but the conductivity can be tuned by doping [98]. Nb-substitution for Ti causes n-type doping and the conductivity can be tuned from $10^{-7} - 10^4$ S/cm [99, 100]. In this work, we have used 0.05 wt% Nb-doped STO which has a room temperature conductivity of 10 S/cm [101], primarily to prevent charging on the sample surface during experiments.

Substrates used in this work were treated prior to epitaxial film growth. As-received substrates with dimensions $15 \times 15 \times 0.5$ mm with 0.1° miscut angle were cut laterally into smaller pieces using a diamond edged circular blade. The substrates were cleaned by acetone and ethanol in ultrasonic baths for 5 min and then annealed in 2 hours at 950°C under oxygen flow in order to create well-defined step-edges.

3.2 $La_{0.7}Sr_{0.3}MnO_3$

$La_{1-x}Sr_xMnO_3$ is the Sr-doped $LaMnO_3$. While $LaMnO_3$ is an AF Mott insulator, Sr substitution of La affects the crystal and electronic structure, giving $La_{1-x}Sr_xMnO_3$ a rich and complex phase diagram. From charge neutrality, when Sr^{2+} substitutes La^{3+}, Mn^{3+} which is $t_{2g}^3 e_g^1$ and high spin is oxidized to Mn^{4+} $3d^3$. This hole doping of the e_g^{1-x} states leads to electron itineracy and FM order by the double-exchange mechanism. Therefore, the half-metallic phase and FM order in LSMO are linked, which is displayed by a coinciding metal-to-insulator transition and T_C. The FM metallic phase is found for $x \in [0.17, 0.46]$ [102]. The Sr doping also reduces the Jahn-Teller distortions found in $LaMnO_3$, but pair-density function experiments have indicated that they are still present locally in the FM metallic phase of $La_{1-x}Sr_xMnO_3$ [103]. At $x = 0.3$, LSMO has a T_C of 370°C. The room temperature ferromagnetism together with a high degree of spin polarization [104] and display of a colossal magnetoresistance effect [14, 105] has led LSMO to become one of the most extensive studied FM manganites.

In bulk, LSMO has rhombohedral symmetry $(R\bar{3}c)$ and an $a^-a^-a^-$ octahedra rotation pattern [14, 106]. Its rhombohedral lattice parameters are $a_{rh} = 5.471$ Å and $\alpha = 60.43°$, which translates to pseudo-cubic $a_{pc} = 3.88$ Å. We hereafter use pseudocubic notation for lattice parameters and crystal directions for all perovskites, unless noted otherwise.

Hydrostatic pressure has been shown to stabilize the FM phase of LSMO. An increase in both the metal-to-insulator transition temperature and T_C is found by application of pressure for a range of Sr-dopant concentrations [107]. T_C has a linear relation to pressure with a coefficient of 0.45 K/GPa reported for $x = 0.3$ [108]. The positive pressure coefficients have been attributed to stabilization of the double-exchange interaction.

The magnetic moments for bulk LSMO have been shown to follow an easy (111) or (110) plane [69, 109, 110], or $[111]$ axis [111], all of which are compatible with magnetocrystalline anisotropy arising from rhombohedral symmetry.

Thin films of $La_{0.7}Sr_{0.3}MnO_3$ on (001)-oriented $SrTiO_3$

The magnetic properties of epitaxial thin films on STO are affected by the thin film geometry and the tensile strain state given by the substrate. The rhombohedral symmetry of bulk LSMO is incompatible with the cubic surface of STO, forcing it into monoclinic symmetry [112]. Different effects are found by varying the crystalline orientation of the substrate surface. (001)-oriented films have in-plane $\langle 110 \rangle$, i.e., two-fold easy axes and $\langle 100 \rangle$ hard axes [20]. (110)-oriented films show a uniaxial in-plane $[110]$ easy axis, due to that the biaxial strain state is anisotropic.

For (111)-oriented films, no macroscopic anisotropy can be disctinguished, while on a microscopic level the magnetic moments are distributed with 6-fold symmetry [113].

(001)-oriented thin films have a volume magnetization of 3.7 μ_B/Mn and a magnetically "dead" layer near the interface, the smallest reported being 3 unit cells [114, 115]. The cause of this loss of FM properties is debated, but orbital reconstruction causing charge ordering [116], or a structural reconstruction resulting in elongated lattice parameter out-of-plane [117] have been suggested. LSMO/STO thin films also have a reduced T_C of 345 K which is attributed to the tensile strain from the substrate [115].

Furthermore, the magnetic properties of LSMO/STO thin films have been shown to depend heavily on oxygen stoichiometry. Anion deficiency is a common type of point defects in perovskites [118], which influences the electronic structure. Lack of oxygen stoichiometry causes cation reduction, which for LSMO implies loss of e_g electrons. Considering the e_g states exclusively, oxygen vacancies essentially counteracts the hole doping done by Sr^{2+}, and therefore weakens the FM phase. This has been demonstrated by conducting epitaxial growth under low oxygen pressures [115, 119].

3.3 $LaFeO_3$

$LaFeO_3$ (LFO) is an insulating AF perovskite, well known for its high T_N of $\sim$ 740 K. With La as its A cation, it has the largest ionic radius at the A-site which stretches the unit cell, straightening the Fe-O-Fe bonds and stabilizing the superexchange [120]. It is $3d^5$ and high spin which promotes superexchange and AF order along all primary axes, resulting in *G*-type AF order. It also hosts a large atomic magnetic moment of 4.4 μ_B/Fe [52]. Due to its pronounced x-ray absorption edges for its valence states, it is widely used for studies of AF properties, and it was among the first antiferromagnets to have its domain texture imaged [121, 122].

LFO has orthorhombic symmetry $(Pbmn)$ with lattice parameters $a_{or} = 5.557$ Å, $b_{or} = 5.565$ Å, and $c_{or} = 7.854$ Å, translated to pseudocubic $a_{pc} \sim 3.93$ Å. The octahedral rotation pattern is $a^-a^-c^+$ and the Fe-O-Fe bonds are buckled to about 155° [123]. Due to asymmetric exchange, the atomic magnetic moments are canted by 9.1 mrad relative to the Néel axis, which is oriented along a $[110]$ axis [120, 124].

Thin films of $LaFeO_3$ strained to $SrTiO_3$

LFO is epitaxially compressive strained to STO. Due to the lattice mismatch, LFO has been shown to prefer its orthorhombic c-axis aligned to the surface plane, along either of the two equal $[100]$ directions, see Fig. 3.1. This causes twinned structural domains oriented 90° to each other, and a four-fold crystalline symmetry around the surface normal [125, 123].

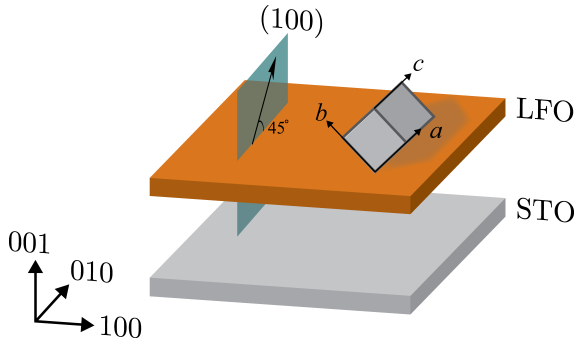

Figure 3.1: Epitaxial $LaFeO_3$ films on (001)-oriented STO. The orientation of the orthorombic unit cell is indicated in grey along one of the two possible directions as discussed in the text. The (100) plane in which the Néel axis is reported to lie is shown in green.

From the bulk magnetocrystalline anisotropy, one could expect the Néel axis to fall along the two available in-plane $[110]$ axes. However, several studies have shown it to be projected by the orthorhombic c-axis with an angle up to 45° out of plane [125]. In other words, in the (100) plane in which the orthorhombic c-axis lies, see Fig. 3.1. The angle giving the out-of-plane component has been reported to vary $(0 - 45^\circ)$ by sensitivity to minor changes in the crystalline structure [126, 127]. The magnetic domains are also reported to strongly follow the crystalline domains [128].

The T_N of LFO is reported to be reduced for thin films in the range 565 - 670 K [128, 122]. This was first assumed to be due to epitaxial strain, but fully relaxed films have also shown significant reduction [129]. In this work, LFO is grown at 813 K (540 °C) and then cooled down through its T_N to room temperature. All subsequent experiments are performed below 400 K.

3.4 Heterostructures and nanopatterning

In this work, we have grown heterostructures of LFO (top layer) and LSMO on (001)-oriented STO substrates. The LFO layer has been kept thin (10 unit cells) in order to let x-rays penetrate the AF layer in spectroscopy experiments, while the LSMO layer thickness has been varied (8-90 unit cells). This section covers some essential properties of this specific system.

At the (001) interface of LFO/LSMO, the AF is ideally fully spin-compensated and a spin-flop coupling takes place [31]. The two sets of magnetic easy axes, i.e., one in each material layer, differ by 45° in respect to each other. A previous study showed that above T_C where the spin-flop coupling is lifted, the LFO layer possesses a four-fold anisotropy with easy axes $\langle 100 \rangle$ and $\langle 110 \rangle$ [126]. The domain distribution over the two sets of axes depends on LFO thickness, in particular showing a slight preference for the $\langle 110 \rangle$ axes for 10 unit cells thickness. The system was also investigated below T_C, at which the Néel axis was found to rotate to align perpendicularly to the FM moments [31], see Fig. 3.2. This implies that the FM anisotropy together with the interface exchange coupling overcomes the anisotropy of the AF layer.

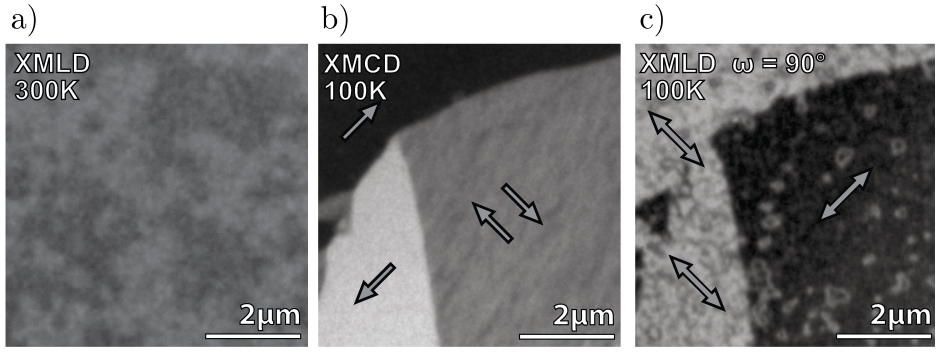

Figure 3.2: Domain structure found in LFO/LSMO heterostructures as measured by x-ray photo-emission electron microscopy. Antiferromagnetic domain structure is shown above the ferromagnetic T_C in (a). Both the LSMO and LFO domain structure is shown below T_C in (b) and (c). Spin orientations are indicated in each of the domains. *Reprinted with permission from* [30].

Nanopatterning of LFO and LSMO single films and LFO/LSMO heterostructures has been shown to induce shape-anisotropy for both layers[32, 33]. For LSMO, the moment axis follows parallel to the edges, which is easily explained in terms of lowering the magnetostatic energy, i.e., classic shape anisotropy. For LFO, the orientation of the Néel axis is more complex. It is found to depend heavily on

crystalline orientation, thickness of the layer, nanopatterning method [130].

For nanostructures of our protoype system, i.e., 10 unit cells LFO / 90 unit cells LSMO / STO, nanopatterning gives both LFO and LSMO a preference of aligning their spin axis parallel to the structure edges. Such collinear alignment is in conflict with the interface spin-flop coupling. For nanomagnets oriented along a crystalline [110]-direction, the spin alignment has been shown to depend on nanostructure width and temperature, as shown in the phase diagram in Fig. 3.3. The width of the nanostructures regulates the influence of the edge effect, and the the spin-flop coupling is found to be stronger at lower temperature. For nanomagnets oriented along [100], a temperature and width dependency is lacking. However, it has been shown that the spin-alignment is collinear for 500 μm wide nanomagnets at 110 K [34].

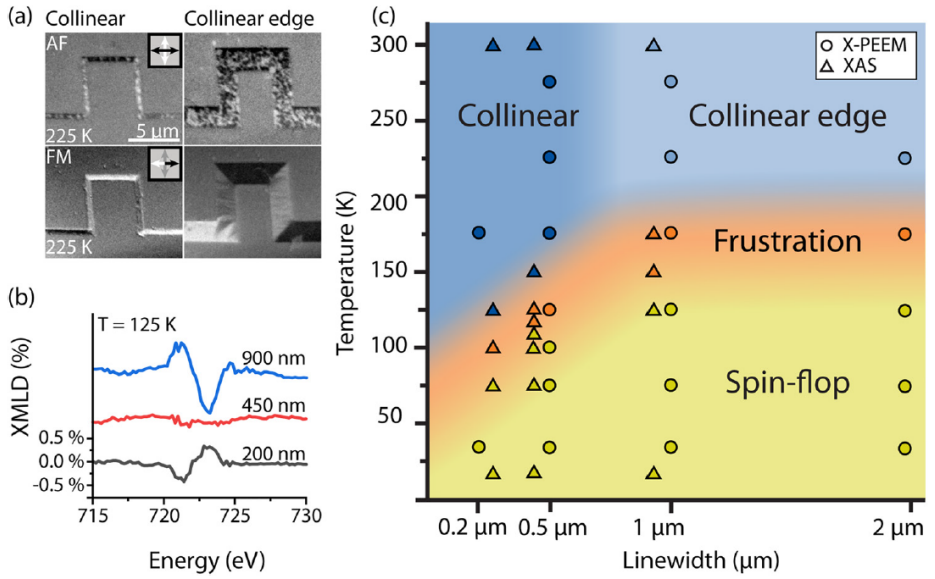

Figure 3.3: Phase diagram showing the alignment of antiferromagnetic and ferromagnetic spins in LFO/LSMO heterostructures. (a) shows selected x-ray photoemission electron microscopy images. (b) shows x-ray magnetic linear dichroism spectra for three linewidths at 125 K. (c) shows the phase diagram. *Reprinted from* [131].

Chapter 4

Experimental techniques

4.1 Pulsed laser deposition

Pulsed laser deposition (PLD) is a material growth technique which uses a pulsed laser to ablate material for deposition onto a substrate within an enclosed environment. It became popular in 1987 when it was used to successfully grow oxide superconductors [132, 133] with quality comparable to that achieved using more advanced alternatives such as molecular beam epitaxy, while its setup is relatively simple and still allows precise control of growth parameters [17]. Today, it is a commonly used technique for growth of epitaxial oxide thin films [134].

The schematic of the PLD setup is shown in Fig. 4.1. While a brief explanation of the growth process is described for each published work in chapter 5, a more detailed outline follows here. The loadlock serves as a transfer stage for the sample holder between atmospheric pressure and the main chamber ($\sim 10^{-8}$ mbar). The sample holder is mounted onto the heater, which is then positioned so the substrate surface is aligned parallel with the target surface - see Fig. 4.1. The chamber is evacuated by a turbo pump, levelled above a roughening pump while the ambient gas mixture and pressure is continuously controlled through connected inlets. Electric current is run through a platinum wire to produce joule heating in proximity of the sample holder. Thermal contact between substrate and sample holder is ensured by silver glue, and an even temperature on the substrate surface is cross checked by a proximity resistivity sensor and an infrared sensor mounted outside the chamber. Detailed growth parameters are listed in table. 4.1. Targets are mounted on a rotatable carousel which enables heterostructure growth. Target material ablation is achieved by a directed pulsed KrF eximer laser (Lambda Physik, PLX Pro 210) with wavelength of 248 nm and fluency of $\sim 2 - 4$ J/cm^2,[1] which produces a plasma plume at the target surface. Prior to material deposition, targets are pre-ablated by 1000 pulses at 5 Hz while a shutter is shielding the substrate. During deposition, an electron gun aimed in a low angle to the sample surface enables in-situ reflective high-energy electron diffraction (RHEED) from during growth, which is monitored by a phosphorous screen (and CCD camera). After growth, the samples are kept at growth temperature in an increased O_2 pressure of 100 mbar for 15 min, before cooled to room temperature.

[1] Laser fluency was always checked before and after growth to ensure steady fluency during growth.

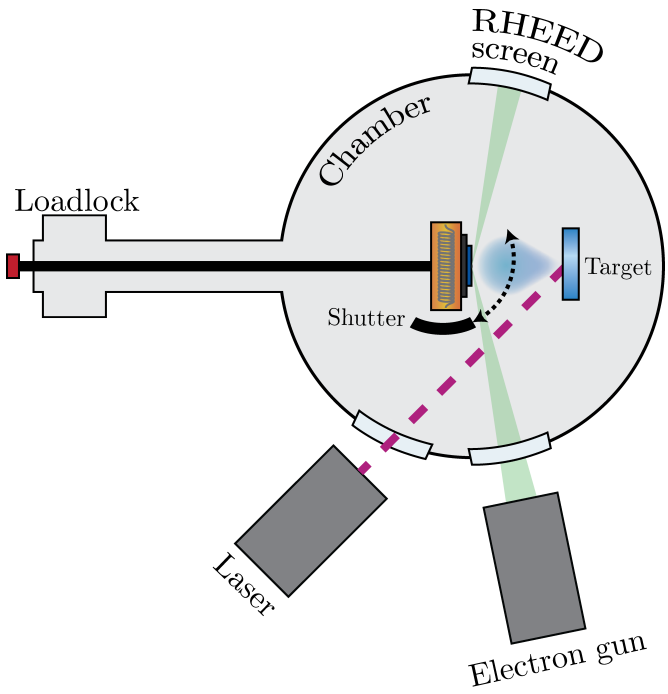

Figure 4.1: Overview of a PLD system. A sample (blue) is mounted on the heater (orange) near the center of the chamber.

Table 4.1: PLD growth parameters for the two materials grown.

Parameters	$La_{0.7}Sr_{0.3}MnO_3$	$LaFeO_3$
Growth temperature (K)	700	540
Oxygen pressure (mbar)	0.35	0.01
Laser pulse frequency (Hz)	5	1
Target-to-substrate distance (mm)	45	50

RHEED

RHEED is a surface sensitive diffraction technique which is used to monitor the crystallinity of the sample surface during growth. The technique was most commonly used a characterization tool in ultra-high vacuum systems due to its pressure sensitivity [135], but setups allowing higher deposition pressures were developed in the late 90's to allow integration in PLD systems [17, 136]. An electron beam is focused onto the sample surface at a grazing angle as seen in Fig. 4.1, and diffracted electrons from the sample surface are gathered on a phosphor screen.

The grazing angle and sample azimuth angle is adjusted for optimal intensity and symmetric diffraction pattern. Example RHEED patterns is shown in Fig. 4.2(a) pre-growth and (b) post-growth. For high quality crystalline surfaces Kikuchi lines may be observed. The intensity of the primary spot (central spot) is monitored by the CCD camera and recorded during growth. Figure 4.2(c) shows a close-up of the initial 90 seconds. Every laser pulse can be identified by a sudden drop in intensity, as new adatoms increase the surface roughness. As described by Boschker et al. [137], the intensity following a laser pulse is a signature of the surface adatom dynamics and can explain growth mechanics. The large oscillations seen on the scale of tens of seconds[2] are attributed to growth of a monolayer. Thus, the thickness of the layers can be monitored in-situ.

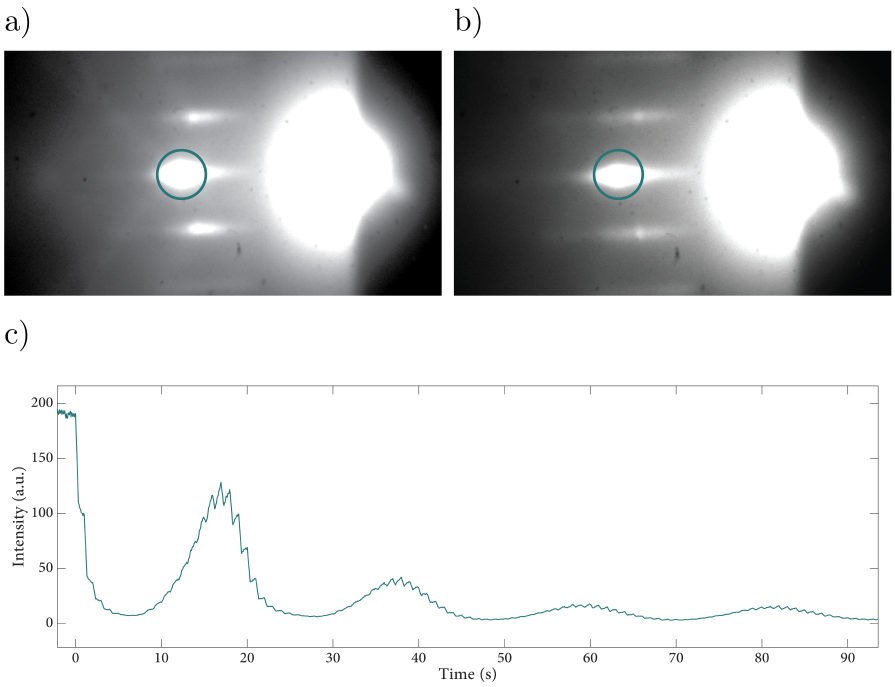

Figure 4.2: RHEED monitoring during growth. (a) shows the diffraction pattern from an (001) STO substrate before growth of a thin film layer. The green circle indicates the area where intensity is to be measured during growth. (b) shows the diffraction pattern after growth of a 100 unit cell thick layer of LSMO. The intensity in both (a) and (b) is increased in the images for better view of the diffraction peaks. (c) shows the measured intensity during growth of the first 4 oscillations. Laser pulses can be observed every 0.2 seconds.

[2]Oscillation period is dependent on parameters such as laser frequency, and here mentioned in relation to the example in the figure.

4.2 Atomic force microscopy

Atomic force microscopy (AFM) is a surface imaging technique which uses a scanning probe in close proximity of the surface. It was invented in 1986 in the advent of the scanning tunneling microscope [138], both techniques which have greatly impacted nanoscale materials research. The setup of the AFM, as shown in Fig. 4.3, is simple yet delicate. Much like a gramophone, a sharp tip mounted on a cantilever is used to scan the topography of a surface, only that the tip is sharp down to the last singular atom. Thus, the interactions experienced by the tip are atom-atom interactions, which leads to sub-nanometer height resolution. The lateral resolution is dependent on in-plane movement of the cantilever, which is most often controlled by piezoelectric crystals. A laser beam aimed at the top side of the cantilever is reflected and detected by an optical sensor screen. The cantilever is oscillated at a set frequency, and thus tip-sample interactions are detected by changes in frequency, phase and deflection of the beam path. The working principle of the AFM allows for measurement of various properties of the sample surface such as topography, but also ferroelectricity, piezoelectricity or magnetic moments. These recording modes can be interchanged by changing the sample tip or working distance (tip to surface distance) to control the type of interaction. In our work, we have used AFM as a tool to inspect four stages of sample preparation. Specifically, (1) inspect as-received substrates, (2) ensure success of thermal annealing, (3) inspect film topography after growth and (4) inspect nanostructures after patterning processes.

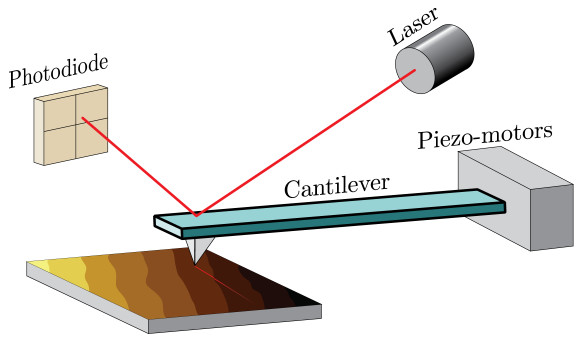

Figure 4.3: A simplified schematic of an atomic force microscopy setup.

4.3 X-ray diffraction

X-ray diffraction (XRD) is a non-destructive technique used to investigate the crystal structure of materials. While the principle of XRD can be used for non-crystalline materials, here we will focus on its usage for crystalline solids. When parallel x-rays are incident on a crystalline material, coherent scattering results from the crystal field, i.e., the electron distribution in the atomic lattice. The x-ray penetration depth is dependent on photon energy but also incident angle of the incoming x-rays. Therefore, measurements can be made surface-sensitive by so-called grazing incidence, while increasing angles will increase the fraction of signal coming from deeper in the material. The conditions for constructive interference is governed by the wavelength λ of the x-rays as well as the spacing of the lattice planes, as described by Bragg's law:

$$2d \sin\theta = n\lambda \tag{4.1}$$

where θ is the angle between the incident x-rays and the lattice plane, and n is an integer. The interplanar distance d for lattice planes is related to the planes' Miller indices (hkl):

$$d_{hkl} = \frac{a}{\sqrt{h^2 + k^2 + l^2}} \tag{4.2}$$

Thus, for angles that satisfy the condition above, lattice planes will yield constructive interference and a large intensity measured by the detector, i.e., diffraction peaks. The diffraction peaks are the Fourier transform of the electron density which scatters the x-rays, and will therefore yield information about the crystal lattice parameters. The Fourier transform implies the reciprocal characteristics to its origin. While infinite crystals would yield diffraction peaks as infinitely small points in real space, diffraction peaks from real crystals are broadened. Lattice planes are two-dimensional and therefore their diffraction peaks will come out as one-dimensional lines, or rods. These lines are intercepted by the detector. The location of the diffraction peaks are found by performing angular scans, i.e., rotating the sample and/or the detector.

Since substrate and film lattice parameters are on the same length scale, scans can be conducted close to substrate diffraction peaks in search for the film peaks. The known substrate lattice parameters therefore also work as a reference to calculate the film parameters. Film peaks will be shifted in the directions where their lattice parameters are unequal to that of the substrate. E.g., for epitaxially strained films, while the in-plane lattice parameters are clamped to the substrate, the out-of-plane lattice parameter relaxes. This causes film peaks to be shifted along Q_Z,

the reciprocal direction corresponding to the out-of-plane direction in real space. Film peaks will also be broadened along this axis due to the low thickness of the film. The substrate peaks are easy to locate since the substrate material is thick and therefore yield a large signal. The intensity of diffraction peaks from thin films are weaker due to the reduced thickness. XRD scan results can be presented by reciprocal space maps (RSMs). Since reciprocal space spans three dimensions, RSMs are usually presented by the two axes displaying the most interesting features. In this work, a Bruker D8 Discover x-ray diffractometer was used. A CuKα_1 radiation source is filtered by a monochromatic crystal, giving a wavelength of 1.5406 Å.

4.4 Vibrating sample magnetometry

Vibrating sample magnetometry (VSM) is a technique used to measure the macroscopic magnetic moment of a material. Its first mention was in 1956 by Foner [139], where its designs' simplicity was demonstrated by allowing it to be assembled from a loudspeaker, a drinking straw, a paper cup and a permanent magnet by the use of glue.[3] A more sophisticated version was published in 1959 [140] and today there are several commercial providers.

A cross section of a VSM setup is shown in Fig. 4.4. The sample to be measured is fixed to the end of a long rod which is suspended vertically in a cylindrical chamber. The top end is clamped to a linear motor, often consisting of piezoelectric materials which oscillates the rod vertically. Detection coils are situated surrounding the sample. In accordance with Faraday's law of induction, electrical current is induced in these pickup coils by any change in the magnetic field within. As the magnetic sample oscillates, current will also oscillate in the pickup coils.

An external magnetic field is achieved by an additional conducting coil mounted outside the cylindrical chamber. This coil is cooled down below its critical temperature, making it superconducting and an electric current is ramped up in order to produce a magnetic field at the sample. Such electromagnets in VSM setups can typically produce fields of several Teslas. Since detection can run simultaneously as the magnet is ramped, dynamic measurements can be done. The lower end of the time scale is however limited to the order of seconds and minutes by the ramping time required for the coil.

In this work, we have used a Quantum Design Versalab system with a VSM module. It allows a sample temperature range of 50-400 K and and applied field strength of ± 3 T. The electromagnet is mounted such that the applied field is parallel to the the detected magnetization. The samples are mounted such that the detection is done parallel to the surface of the films. The sample mounting is fixed, i.e., it cannot be rotated after insertion. Note that for the materials used in this work, the VSM temperature range enables heating above the LSMO T_C, but not the LFO T_N.

[3] We note that sometimes novel experimental setups can be so beautifully simple.

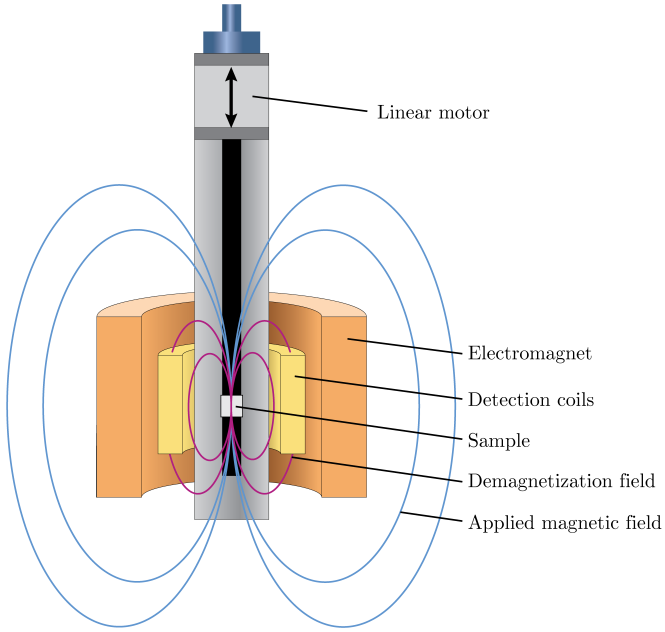

Figure 4.4: Vibrating sample magnetometry setup.

4.5 X-ray absorption spectroscopy

Photons can be utilized to investigate the electronic and chemical structure of a material. With sufficient energy for photons incident on a material, photoexitation can occur, a photon-matter interaction where the photon is absorbed and an electron situated in a low-energy orbital is excited to one at higher energy. In x-ray absorption spectroscopy (XAS), energies that correspond to such transitions, called edges, and are named after the shells $(K, L, M, ..)$ which electrons are excited from. The structure of the edges is a direct signature of the material's electronic structure. Their width depicts the density of states of the bands formed by the orbitals. Figure 4.5 shows an absorption spectrum for $LaFeO_3$ around the L_2 and L_3 edges, together with the relevant transitions. The $3d$ bands are narrow and therefore the L edge is sharp. Since the p orbitals are split by spin-orbit coupling, transitions from $p_{1/2}$ and $p_{3/2}$[4] produce the two peaks named L_2 and L_3. In addition, due to crystal field splitting of $3d$ orbitals in perovskites, as discussed in chapter 2.3, the edges display fine structure.

These edges have energies on the scale of hundreds of eV, i.e., in the soft x-ray regime. Synchrotron radiation is therefore an x-ray source suited for XAS, since soft x-rays with tunable energy are required. In this work, we have performed XAS experiments at the Magnetic Spectroscopy and Scattering (4.0.2) beamline at the Advanced Light Source.

XAS is measured either by detection of transmitted x-rays or by secondary effects such as fluorescence or Auger electrons. For our work, the use of transmission mode is excluded since it requires thin samples, and our substrates have a thickness of 5 mm. On the other hand, Auger electrons create a cascade of scattered electrons resulting in high electron yield. Therefore, a total electron yield detection method has been used which counts the total number of electrons that are emitted from the sample by measuring the supplying current from ground, see Fig. 4.6(a). Both Auger and secondary electrons generated in the sample have a short mean free path, limiting the probing depth to a few nanometers even though the soft x-ray penetration depth is 20 – 100 nm [65], hence this is a surface sensitive technique. On the other hand, the detection method allows for magnetic fields to be applied to the sample during measurement.

[4] $1/2$ and $3/2$ refer to the total angular momentum number $J = L + S$

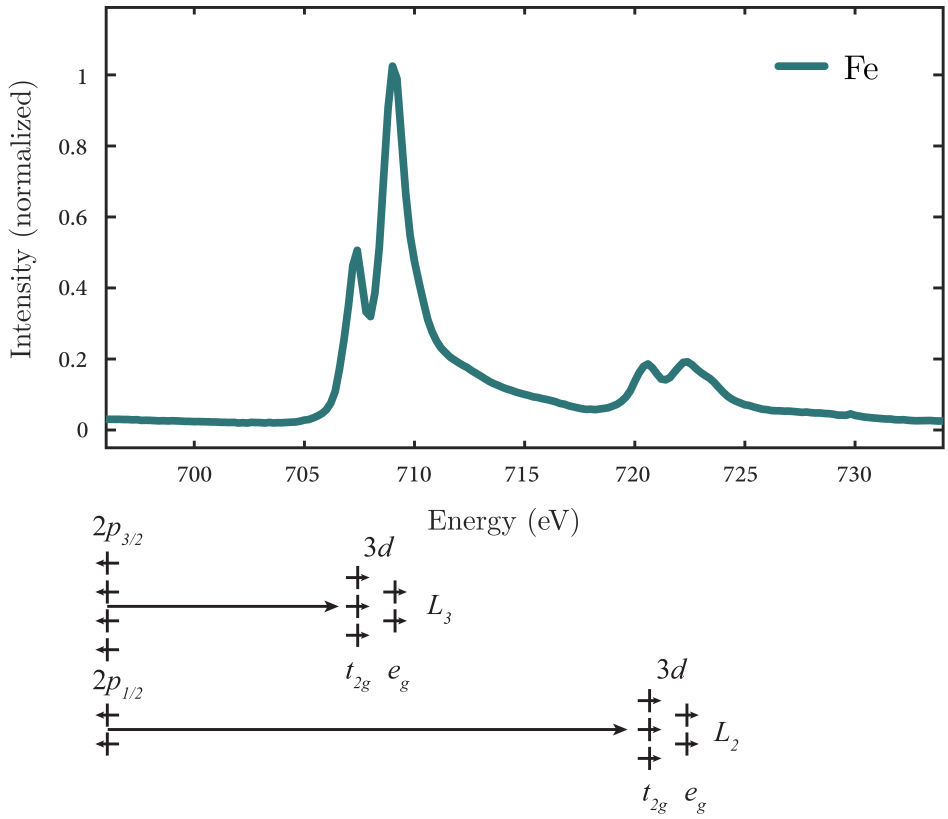

Figure 4.5: An x-ray absorption spectrum obtained from $LaFeO_3$, showing the L_3 and L_2 absorption edges. Below the graph is an illustration of the electronic transitions giving rise to the edges and their fine structure.

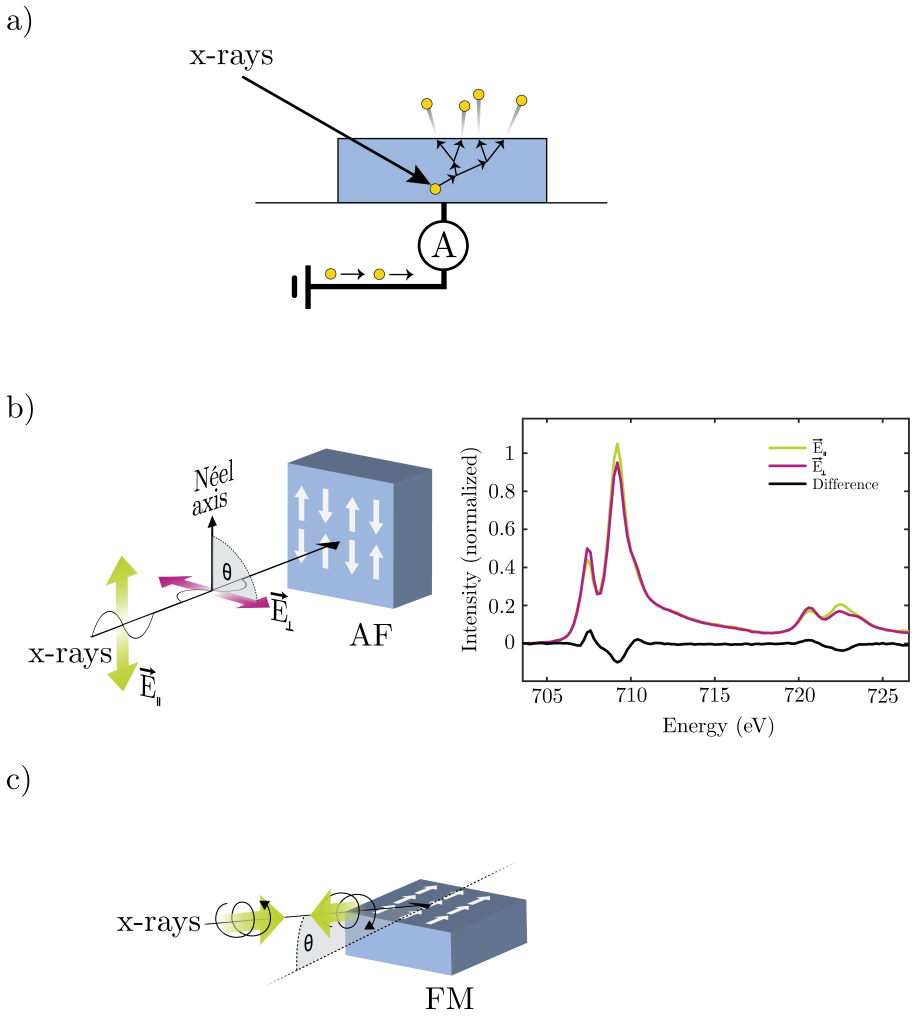

Figure 4.6: Illustration of x-ray absorption spectroscopy experiments. a) Schematic of Auger and secondary electron cascade generation and total electron yield measurement. b) Illustration of sample geometry during XMLD measurement (left) and an XMLD spectrum taken of $LaFeO_3$ at 80 K as an example (right). c) Illustration of sample geometry during XMCD measurement setup.

4.6 X-ray magnetic dichroism

The x-ray absorption can display dependency on the polarization of the incoming photons, a phenomenon termed dichroism. In a simplified picture, the absorption probability is dependent on whether the angular momentum of the incoming photons are easily transferred to the electrons which are to be excited. In magnetic materials, the electron spins giving rise to the magnetic moments are ordered, which therefore will result in larger absorption when the electric field vector of the incoming light is aligned to certain directions. Two types of polarization are discussed – linear and circular.

4.6.1 Linear dichroism

X-ray magnetic linear dichroism (XMLD) arises from uniaxial spin alignment and is therefore found for both FM and AF magnetic order. A schematic is illustrated in Fig. 4.6(b) together with an example of an LFO XMLD absorption spectra. The XMLD intensity is dependent on the alignment of the E-vector of the linearly polarized light and the magnetic spin axis [121]:

$$I_{XMLD} = a + b\left(\cos^2\theta - 1\right)\left\langle M^2\right\rangle_T \tag{4.3}$$

where a and b are constants, θ is the angle between the electric field vector and the magnetic spin axis, and M is the temperature dependent average of the magnetic moment [65]. For XMLD, the dichroism is similar on the L_2 and L_3 peaks, but opposite for transitions to t_{2g} and e_g states which leads to an asymmetric intensity change on each of the two L edges. XMLD is therefore done by performing two scans with x-rays polarized 90 degrees respective to each other in each scan, and the result is often presented as the difference between the two scans (seen as "up-down" signature in Fig. 4.6(b). The incidence of the light can be perpendicular to the sample surface such as shown in the figure.[5] However, determination of Néel axis orientation is still not straight forward. In principle, an up-down or a down-up signature should relate to which of the two x-ray polarizations the Néel axis is parallel to. At first, XMLD signal was believed to be angle-independent. However, Czekaj et al. found for LFO that the sign of the signal can switch depending on the orientation of the magnetization relative to the crystalline axes [127]. This angle dependency was further elaborated by Arenholz et al. for cubic systems [141, 142], demonstrating that the XMLD signal can disappear or change sign.

[5] The two polarization are sometimes referred to as s- and p- polarization. This is typically when the measurement geometry is such that the incoming light does not have normal incidence, implying one of the two polarizations have an out-of-plane component. The polarization which is in-plane is then termed p (from German parallel) and the other s (from German senkrecht).

Therefore, careful interpretation must be done.

4.6.2 Circular dichroism

X-ray magnetic circular dichroism (XMCD) requires directional spin alignment, i.e., a FM order or net magnetization. An illustration of measurement geometry is shown in Fig. 4.6(c). The absorption probability is dependent on the alignment of the helicity vector of the circularly polarized light being parallel or antiparallel to the orbital angular momentum of the electron to be excited. Therefore, a strong coupling of the spin to the orbital angular momentum, i.e., spin-orbit coupling, is crucial for an XMCD signal. The intensity is given by:

$$I_{XMCD} = a \cos\theta \langle M \rangle_T \tag{4.4}$$

Since the x-ray helicity vector must have a component in the direction of the magnetic axis, for magnetic thin films where the moment is dominantly in-plane, normal incidence is excluded. A complete parallel alignment of polarization is also geometrically impossible and therefore experiments are done with an incident angle $0^\circ < \theta < 90^\circ$. For XMCD, the dichroism is opposite for the L_2 and L_3 edges, i.e. polarization giving an increase on L_3 will give a decrease on L_2 and vice versa.

4.7 X-ray photo-emission microscopy

X-ray photo-emission electron microscopy (XPEEM) is an imaging technique based on the principles of x-ray absorption and Auger/secondary electron emittance, as previously discussed for XAS. XPEEM can therefore implement the principles of XMLD and XMCD to generate lateral resolution of the magnetic spin structure in materials. While several imaging modes are available with XPEEM, here we will focus on magnetic contrast. By the use of a strong electric field, electrons emitted from the sample are accelerated and directed towards an optical column and detection screen. Modern XPEEM instruments allow a magnification up to 10.000. The spatial resolution is $\sim$ 20 nm, limited by several conditions. Sample topography results in curvature of the electric field, which degrades the resolution. The secondary electrons used for detection are spread in energy, causing chromatic aberration. Due to the limited mean free path of electrons, the technique is also surface sensitive and the probing depth is a few nanometers. A key limitation to XPEEM in contrast to the XAS setup discussed earlier, is that applied magnetic fields will alter the path of emitted electrons flowing towards the detector, and thereby blurring the image. Nevertheless, XPEEM is outstanding in probing the magnetic structure of thin films without any considerable disturbance of the magnetic structure, something which can be considerable for alternative imaging techniques such as magnetic force microscopy. It also allows for element specific probing of magnetic moments. In this work, we have used the PEEM-3 (11.0.1) beamline at the Advanced Light Source and the SIM (X11MA) beamline at the Swiss Light Source.

In an XPEEM experiment, an XAS scan is initially performed to determine precise edge energies. Thereafter, two separate images are taken (A and B) with energies fixed to peaks which display XMLD or XMCD contrast. For XMCD, one image is taken at the L_3 edge and the other at the L_2 edge. For XMLD, two energies of different multiplet peaks on the same edge are chosen – typically on the L_2 edge since its multiplet splitting is particularly pronounced. The asymmetry is then calculated by dividing the A and B intensity difference by the sum, $(B - A)/(B + A)$.

Chapter 5

Papers

Author's contribution

The work in this thesis has resulted in three main papers which are included in the following chapter.

Paper A

In *Coexisting spin-flop and exchange bias in $LaFeO_3$/$La_{0.7}Sr_{0.3}MnO_3$ heterostructures*, the PLD growth of thin film and heterostructure samples, AFM, XRD and VSM measurements were carried out by the lead author. XMCD and XMLD investigation was done at the Advanced Light Source in collaboration with I. Hallsteinsen, E. Arenholz and E. Folven. The lead author analyzed the data and wrote the manuscript in close collaboration with all co-authors.

F.K. Olsen, I. Hallsteinsen, E. Arenholz, T. Tybell and E. Folven.
Physical Review B, **99**, 134411, (2019).

Paper B

In *Enhanced magnetic signal along edges of embedded epitaxial $La_{0.7}Sr_{0.3}MnO_3$ nanostructures*, the lead author carried out the PLD sample growth, AFM, XRD and VSM measurements. XMCD-PEEM measurements was carried out in collaboration with all coauthors. The lead author analyzed the data and wrote the manuscript in collaboration with all coauthors.

F.K. Olsen, A.D. Bang, E. Digernes, S.D. Slöetjes, A. Scholl, R.V. Chopdekar, T. Tybell, J.K. Grepstad and E. Folven.
Journal of Magnetic Materials and Magnetism, **521**(1), 167324, (2021).

Paper C

In *The effect of $LaFeO_3$ on $La_{0.7}Sr_{0.3}MnO_3$ line structures*, the PLD growth and post-growth characterization was carried out by the lead author. Sample patterning was done by A.D. Bang. VSM measurements were done in collaboration with Y. Lever. The lead author analyzed the data and wrote the manuscript in collaboration with all coauthors.

F.K. Olsen, Y. Lever, A.D. Bang, J.K. Grepstad, E. Folven.
Paper to be submitted

Paper A

Coexisting spin-flop coupling and exchange bias in $LaFeO_3/La_{0.7}Sr_{0.3}MnO_3$ heterostructures

F.K. Olsen, I. Hallsteinsen, E. Arenholz, T. Tybell and E. Folven.
Physical Review B, **99**, 134411, (2019).

Coexisting spin-flop coupling and exchange bias in $LaFeO_3/La_{0.7}Sr_{0.3}MnO_3$ heterostructures

F. K. Olsen,[1] I. Hallsteinsen,[1,2] E. Arenholz,[2] T. Tybell,[1] and E. Folven[1]
[1]*Department of Electronic Systems, NTNU – Norwegian University of Science and Technology, 7491 Trondheim, Norway*
[2]*Advanced Light Source, Lawrence Berkeley National Laboratory, Berkeley, California 95616, USA*

(Received 11 January 2019; revised manuscript received 27 February 2019; published 5 April 2019)

Exchange bias occurs in field-cooled antiferromagnet/ferromagnet systems and can most often be explained in terms of uncompensated magnetic moments at the interface that are pinned in their orientation during field cooling. The presence of spin-flop coupling is often associated with spin-compensated interfaces. Here, we report exchange bias in complex oxide heterostructures of antiferromagnetic $LaFeO_3$ and thin layers of ferromagnetic $La_{0.7}Sr_{0.3}MnO_3$ with several intriguing features. The exchange bias does not require field cooling but can also be obtained by applying a setting field at elevated temperature. Furthermore, the exchange bias is positive for setting fields up to 3 T, and its magnitude is strongly dependent on the setting-field strength. X-ray magnetic linear dichroism measurements show a predominantly perpendicular spin configuration at the interface. We discuss the possibility of the exchange bias being driven by a net moment from spin canting in the antiferromagnet due to Dzyaloshinkii-Moriya interactions.

DOI: 10.1103/PhysRevB.99.134411

I. INTRODUCTION

Complex oxide heterostructures and their interfaces offer a wide range of new and unexpected phenomena with potential for utilization in modern devices [1]. In highly correlated electron systems, interfacial magnetic frustration, discontinuity of electron states, and strain- or charge-transfer-induced orbital reconstructions may give rise to new ground states and functional properties [2,3]. Phenomena such as superconductivity, colossal magnetoresistance, metal-insulator transitions, and multiferroicity have attracted much attention over the last decades [4–6], and recent developments in modern material synthesis have enabled research on tuning of these functional properties using interface engineering.

At the interface between a ferromagnet (FM) and an antiferromagnet (AF), exchange coupling of the FM and AF spin lattices can give rise to increased coercivity in the FM layer and in some cases induce a unidirectional anisotropy or exchange bias (EB) [7]. Due to its technological relevance, the EB effect has attracted much attention since its discovery but its origin in diverse systems is still researched extensively today [8–10]. In most systems EB is obtained by field cooling (FC) the AF/FM system through the AF ordering temperature, T_N. However, spontaneous EB that does not require field cooling has been reported, e.g., in $Fe/Cr_2O_3/Fe$ trilayers [11] and Ni-Mn-Sn alloys [12] and recently also in perovskite systems such as polycrystalline $La_{1.5}Sr_{0.5}CoMnO_6$ [13], and $La_{0.7}Sr_{0.3}MnO_3/Eu_{0.45}Sr_{0.55}MnO_3$ heterostructures [14]. A shift of the hysteresis loop in the opposite direction of the cooling field is most commonly observed (negative EB), but a loop shift in the cooling-field direction (positive EB) has also been reported [15–18].

Theoretical models often explain EB by the presence of uncompensated magnetic moments at the interface. These uncompensated moments could result either from the bulk-truncated spin structure or, in cases where a spin-compensated AF surface is expected, from defects, surface roughness, AF spin canting, or induced FM- or spin-glass order in the antiferromagnet [8–10,19]. Furthermore, Dong *et al.* predicted that Dzyaloshinkii-Moriya interactions (DMIs) could give rise to EB in *G*-type AF/FM perovskite heterostructures with spin-compensated interfaces [20], and EB was later observed experimentally in the $SrMnO_3/La_{2/3}Sr_{1/3}MnO_3$ system [21]. Since DMIs in perovskites are closely linked to the extent of octahedral rotations, epitaxial strain can be used to modify the interaction, which enables engineering of EB in perovskites.

In many systems showing EB, the spin coupling across the AF/FM interface is reported to be collinear and EB is explained in terms of an imbalance in the number of parallel and antiparallel aligned spins. For some spin-compensated AF/FM systems, a spin-flop coupling is found, i.e., the AF spin axis is aligned perpendicular to the FM spin axis [22]. The spin-flop coupling is highly sensitive to imperfections in the spin compensation, which would cause a transition to collinear coupling [10], and most EB systems are reported to show collinear coupling. However, coexisting EB and spin-flop alignment has also been found, e.g., in the ferrimagnetic/AF system of Fe_3O_4/CoO where DMI is proposed to give rise to uncompensated moments [23].

Here, we report positive EB which can be set without FC through a magnetic ordering temperature in $LaFeO_3/La_{0.7}Sr_{0.3}MnO_3$ (LFO/LSMO) heterostructures grown epitaxially on (001)-oriented $SrTiO_3$ (STO). The *G*-type AF order in LFO gives rise to a fully spin-compensated interfacial plane, and spin-flop coupling has been demonstrated in several experimental studies [24,25]. LFO is known to exhibit DMI which causes weak ferromagnetism [26], but EB has not been reported in this epitaxial system before. We discuss how spin canting in LFO can give rise to a net moment at the interface, explaining the EB, without breaking the spin-flop state in this system.

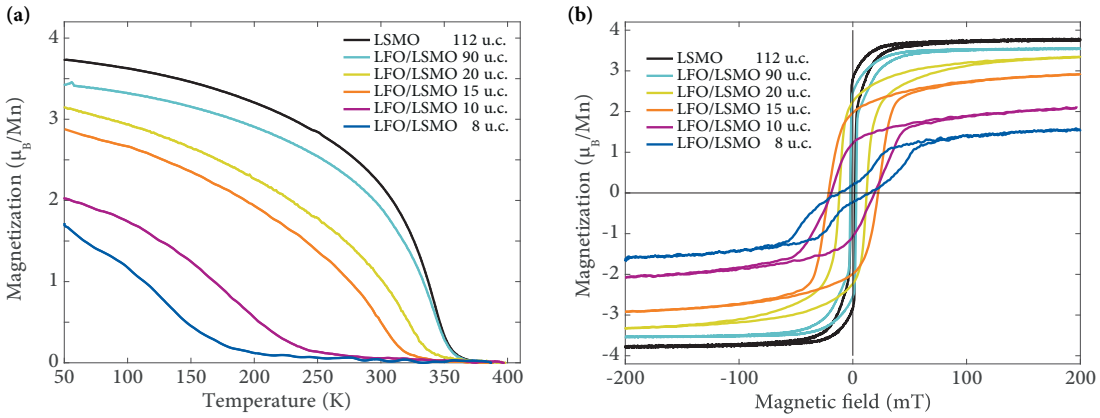

FIG. 1. (a) Saturation magnetization as function of temperature, measured during gradual heating in a field of 200 mT, after field cooling in 3 T from 400 K and (b) hysteresis loops of as-grown samples measured at 50 K after cooling in zero field. The moment is normalized to Bohr magnetons (μ_B) per Mn ions in the LSMO layer.

II. EXPERIMENTAL

Epitaxial LSMO films and LFO/LSMO heterostructures were grown on (001)-oriented STO using pulsed-laser deposition. Samples investigated by x-ray spectroscopy were grown on conducting STO substrates doped with 0.05 wt % Nb to avoid charging. A KrF excimer laser ($\lambda = 248$ nm) with a fluency of $\sim 2\,\mathrm{J/m^2}$ and frequency of 1 Hz (LSMO) and 5 Hz (LFO) was used. Oxide layers were deposited at 700 °C (LSMO) and 540 °C (LFO) in oxygen pressures of 0.35 mbar (LSMO) and 0.01 mbar (LFO). *In situ* reflection high-energy electron diffraction showed monolayer oscillations throughout the growth. After deposition, the samples were annealed in an oxygen pressure of 100 mbar for 15 min. LSMO samples were grown with layer thicknesses of 10 u.c. (unit cells), 15, 20, 40, and 112 u.c. (4–43 nm), and heterostructures with fixed LFO thickness of 10 u.c. (4 nm) and LSMO thicknesses 8, 10, 15, 20, and 90 u.c. (3–35 nm) were synthesized. Atomic force microscopy revealed surfaces with submonolayer roughness and step edges inherited from the STO substrate. X-ray diffraction measurements were performed on samples with thickness >20 u.c. and showed LSMO layers fully strained to the STO substrate. Magnetization data were acquired using a Quantum Design vibrating sample magnetometer (VSM) in the temperature range 50–400 K. Care was taken to ensure that all experiments were conducted using the same cooling rate (20 K/min) and any external setting fields were applied using the same field-ramping rate (20 mT/s). X-ray magnetic circular and linear dichroism measurements (XMCD and XMLD, respectively) were performed at beamline 4.0.2 at the Advanced Light Source, Lawrence Berkeley National Laboratory.

III. RESULTS AND DISCUSSION

Figure 1(a) shows the saturation magnetization as a function of temperature for the LFO/LSMO heterostructures together with a 112-u.c. single-layer LSMO reference sample. Both volume magnetization and the Curie temperature, T_C, show a strong dependence on LSMO thickness. This agrees well with previous studies where reduction of M and T_C for thin epitaxial LSMO layers on STO is explained in terms of a magnetically dead layer near the film-substrate interface, and an associated transition from a three-dimensional to a two-dimensional magnetic ordering [27,28]. For LFO thin films grown on (001) STO, $T_N = 670$ K [29].

FM hysteresis loops for as-grown single-layer LSMO and LFO/LSMO heterostructures measured at 50 K are shown in Fig. 1(b). The hysteresis loops are all symmetric around the origin and the heterostructures show a coercive field, H_C, an order of magnitude larger than that of single-layer LSMO films. Enhanced coercivity is a common observation when ferromagnets are coupled to antiferromagnets, and our values correspond to those previously reported for LFO/LSMO heterostructures [30]. In LFO/LSMO samples with an LSMO thickness down to 10 u.c., single hysteresis loops are observed. However, the heterostructure with 8-u.c. LSMO shows signs of a double loop, suggesting possible EB in the system.

Upon FC from 400 to 50 K in a 3-T field applied along the crystallographic [100] axis, hysteresis loops obtained at 50 K reveal pronounced EB in all heterostructures, except for the sample with a thick (90-u.c.) LSMO layer. The hysteresis loop shift is in the same direction as the cooling field, i.e., a positive EB is observed. Hysteresis loops for the LFO (10-u.c.)/LSMO (8-u.c.) heterostructure are shown in Fig. 2(a), where the EB shift is 29 mT after FC, for both directions of the setting field.

The dependence of the EB on cooling-field strength is investigated by performing FC from 400 K ($>T_C$) to 50 K and subsequently measuring hysteresis loops at 50 K, $H_{\mathrm{EB}}^{50\ \mathrm{K}}$, for the LFO (10-u.c.)/LSMO (8-u.c.) heterostructure; see Fig. 2(b). We find $H_{\mathrm{EB}}^{50\ \mathrm{K}}$ to be positive for all cooling fields and increase monotonically with field strength up to 3 T. The biased loops are asymmetric around the loop center for all field strengths, which suggests that a 3-T field is not sufficient to fully saturate the bias. For the zero-field-cooled measurements shown in Fig. 1(a), the two subloops in the

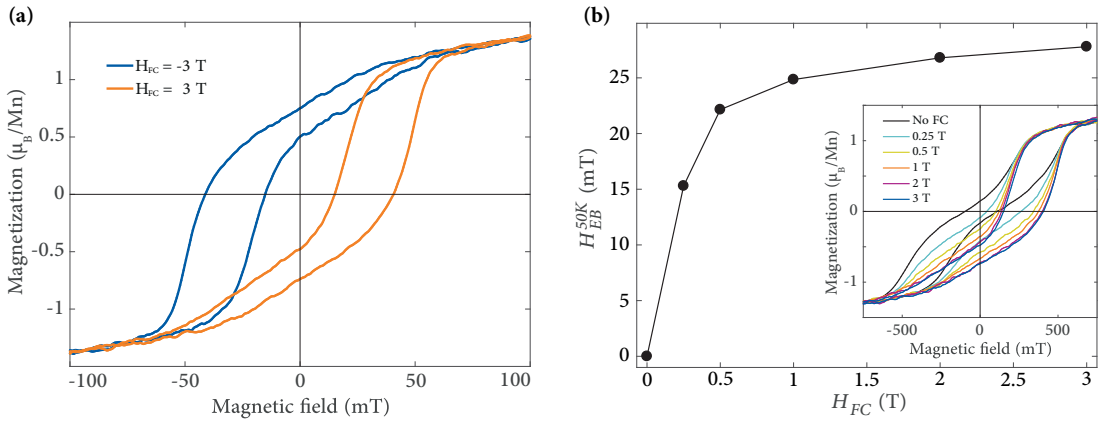

FIG. 2. Exchange bias measured after field cooling, shown for the LFO (10-u.c.)/LSMO (8-u.c.) sample. (a) Hysteresis loops measured at 50 K after field cooling in 3 T fields from 400 K. (b) Exchange bias obtained at 50 K as function of cooling-field strength, where field cooling is performed from 400 K. The solid line is meant as a guide to the eye. The inset in (b) shows the hysteresis loops measured at 50 K.

hysteresis indicate that there are biased domains even after growth, but a balanced distribution of domains biased in different directions. As can be seen in the inset in Fig. 2(b), the subloop shifted in the cooling-field direction grows at the expense of the other upon FC. This indicates that all domains generate a positive EB and that the ones aligned with the cooling field grow with increasing field strength. Positive EB can be explained by a net magnetic moment at the interface which favors antiparallel coupling to the bulk FM moment. We note that Bruno *et al.* have recently reported induced FM moments on Fe at the LFO/LSMO interface [30]. These moments are only present below T_C and couple antiparallel to the Mn moments in LSMO. However, as these induced moments are found to follow the rotation of the LSMO moments, they do not give rise to EB.

The temperature dependence of the observed EB is examined by gradually heating the samples from 50 K, after FC in 3 T, and measuring hysteresis loops in intervals of 25 K. The EB values obtained as a function of temperature are shown in Fig. 3(a). As the temperature is increased, a monotonic reduction of the EB is found up to a blocking temperature T_B, i.e., the temperature where the EB goes to zero. The T_B values for the different samples, indicated in Fig. 3(a), show no clear trend with film thickness and are found to be in the range 150–200 K. We find T_B to be lower than T_C for all LSMO thicknesses. These data indicate that T_B and the T_C of LSMO are not directly related.

The coercive field observed after FC is larger than for single LSMO films and decreases with increasing temperature, as shown in Fig. 3(b). We note that there is no obvious change in H_C at T_B. Compared to the single-layer LSMO reference sample, enhanced H_C is also found above T_B while EB disappears. Our results indicate that the mechanisms that give rise to EB and increased H_C, respectively, have different temperature dependence and are of different origin.

After heating above T_B, even as high as 400 K, we still find a significant EB when the samples are cooled back down to 50 K in zero field. This result implies that the moment responsible for EB is lost neither at T_B nor at T_C. Hence, neither of these temperatures corresponds to the ordering temperature of the moment causing EB. This result also suggests that T_B in our system is not associated with a spin-glass freezing temperature, as has been reported for similar systems showing EB [31,32]. Performing multiple (30×) field loops at 50 K does not result in any training of the system (data not shown). However, we find that the symmetric double loop, with no net EB, as shown in Fig. 1(b) can be regained by performing a demagnetizing cycle (i.e., alternating fields) at 400 K, starting at 3 T with decrements of 10 mT.

To further explore how EB behaves in this system, we apply different setting fields, H_{set}, at different temperatures, T_{set}, cool the sample in zero field, and measure $H_{\text{EB}}^{50\text{ K}}$. We find that the EB can be set without FC, i.e., the system features spontaneous EB, and that the magnitude of the EB depends on both H_{set} and T_{set}. Figure 4 (lower panel) shows the resulting $H_{\text{EB}}^{50\text{ K}}$ for the LFO (10-u.c.)/LSMO (8-u.c.) sample. We find three different regimes. For low T_{set}, the EB is "frozen", i.e., applied fields up to 3 T are insufficient to set any EB. For intermediate T_{set}, the EB can be partially set, i.e., the magnitude of the EB depends on the value of H_{set}. For high T_{set}, the EB can be fully saturated and we obtain the largest EB values; however, a reduction in $H_{\text{EB}}^{50\text{ K}}$ is also found as T_{set} is increased above ∼250 K. Figure 4 (upper panel) shows the $H_{\text{EB}}^{50\text{ K}}$ values for $H_{\text{set}} = 3$ T in detail together with the values obtained by FC from the same temperatures. Comparing the FC- and zero-FC data, we find that no EB can be set at low temperature and intermediate T_{set} leads to similar $H_{\text{EB}}^{50\text{ K}}$ values for both cases. We also find a bifurcation point at intermediate T_{set}. While FC from temperatures above 250 K yields the same $H_{\text{EB}}^{50\text{ K}}$ as for 250 K, zero-FC yields largest $H_{\text{EB}}^{50\text{ K}}$ for $T_{\text{set}} = 250$ K but it is reduced as $T_{\text{set}} > 250$ K. The decreased values of $H_{\text{EB}}^{50\text{ K}}$ for higher T_{set} can be attributed increased thermal fluctuations, i.e., the moment which causes EB is effectively reduced when the applied magnetic field is

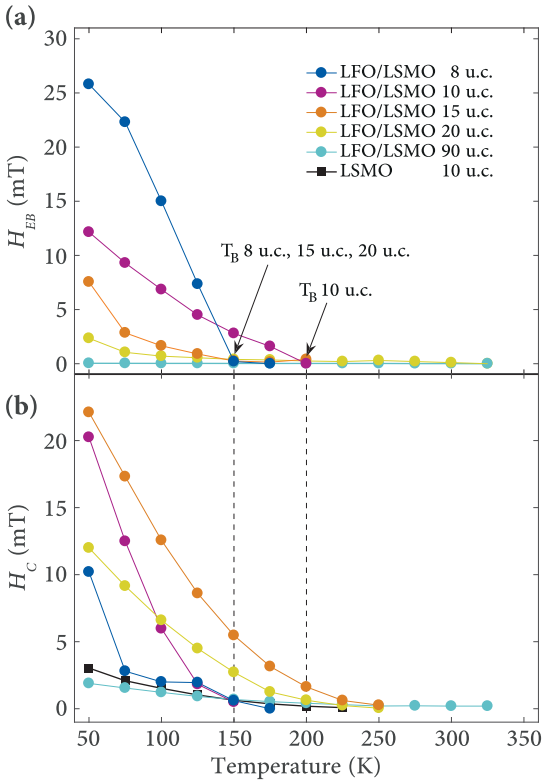

FIG. 3. Temperature dependence of (a) exchange bias and (b) coercivity in the LFO/LSMO heterostructures as function of increasing temperature, measured after field cooling in 3 T from 400 K. The solid lines are meant as a guide to the eye. Approximate values of T_B for the heterostructures are indicated in (a) and the coercive field for the 10-u.c. LSMO single-layer sample is included for reference in (b). The dashed lines are meant as a guide to the eye.

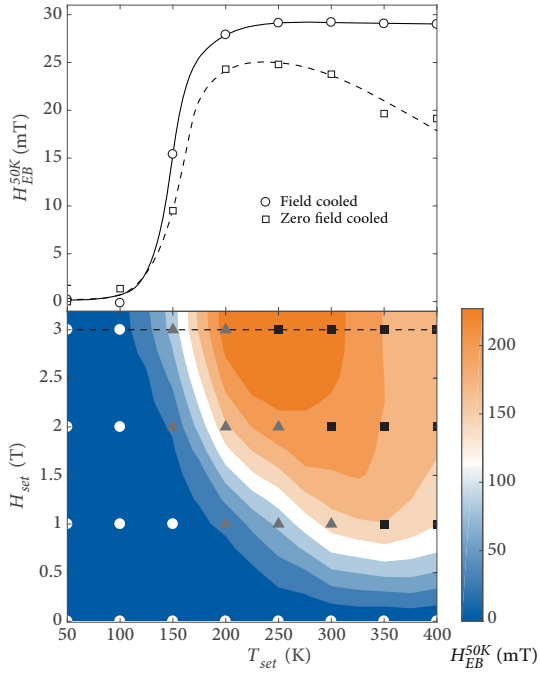

FIG. 4. $H_{EB}^{50\,K}$ measured after applying a setting field H_{set} at a temperature T_{set} and zero-field cooling to 50 K (lower panel). The color grading is based on interpolation between the data points and serves as a guide to the eye. Symbols indicate the three regimes; frozen (white circles), intermediate (gray triangles), and saturation (black squares). The EB is reset by field cycling at 400 K in between each measurement. The data points indicated by the dashed line in the lower panel are shown in the upper panel (squares) together with exchange bias measured at 50 K after field cooling in 3 T (circles) from T_{set}. The solid and dashed lines in the upper panel are guides to the eye.

removed. Since the field is not removed in the FC case, a larger $H_{EB}^{50\,K}$ is obtained. Furthermore, we see from Fig. 4 (lower panel) that lowering T_{set} requires an increase in H_{set} in order to obtain similar EB values. We attribute this feature to an increase in coercivity for the magnetic moments responsible for the EB, as temperature is lowered. We also note that an EB can be set at 400 K without FC, which indicates that the ordering temperature of the moment causing EB is above this temperature.

The EB as function of LSMO thicknesses is shown in Fig. 5. An EB is only observed for LSMO thicknesses of 20 u.c. (8 nm) and below, and increases abruptly as the LSMO layer thickness is reduced. We apply a simple model following the original ideas of Meiklejohn and Bean, which relates the EB to the thickness of the FM layer.

$$H_{EB} = \frac{\sigma_{int}}{M_{FM} t_{FM}}.$$

Here, σ_{int} is the effective interfacial energy density arising from the magnetic moments causing EB, and M_{FM} and t_{FM} are the FM magnetization and thickness, respectively [7,33,34]. For a *G*-type antiferromagnet such as LFO, the (001) interface is ideally spin compensated. However, our experimental EB values for the different LSMO thicknesses correspond to σ_{int} in the range $7-15\,\mu J/m^2$. The average value $\sigma_{int} = 10.6\,\mu J/m^2$ is used to calculate the solid line in Fig. 5. We note that the EB and corresponding σ_{int} values are in the same range as reported in studies on metal/LFO systems, e.g., Fe/LFO and Co/LFO [35,36]; however, orders of magnitude lower than the theoretical predicted values for fully uncompensated interfaces. This suggests that the LFO/LSMO interface consists of only a fraction of uncompensated spins. σ_{int} can be expressed as $\sigma_{int} = J\vec{S}_{FM}\vec{S}_{AF}/a^2$, which includes the interface exchange interaction, J, between the interfacial spins $\vec{S}_{FM}$ and $\vec{S}_{FM}$ in the FM and AF layers and a, which is the in-plane unit-cell parameter of the AF. One possibility is that a fraction of the interfacial Fe spins couples antiparallel rather than spin flop to the Mn spins in LSMO. In this situation the AF spins would not cancel and ∼5% of interfacial Fe spins being antiparallel ordered to LSMO would explain the

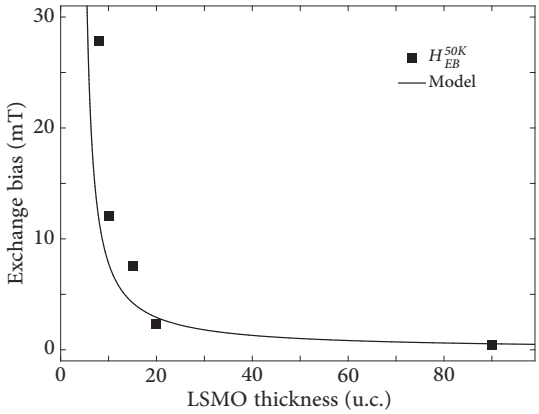

FIG. 5. Exchange bias as function of LSMO layer thickness, with data points measured at 50 K after field cooling in 3 T from 400 K. The solid line represents the Meiklejohn and Bean model, calculated with the average σ_{int} of 10.6 μJ/m^2 . A magnetic dead layer of 4 u.c. in LSMO has been accounted for in the calculations.

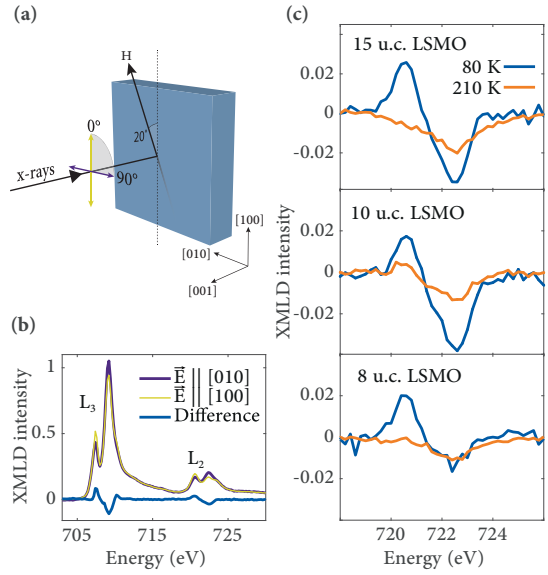

FIG. 6. (a) Schematic of the XMLD measurement geometry. (b) XAS spectra for the LFO (10-u.c.)/LSMO (15-u.c.) heterostructure obtained at 80 K for two linear polarizations, together with XMLD difference. (c) Difference in dichroism signal at the L_2 edge for heterostructures with different LSMO layer thickness, obtained at 80 and 210 K.

observed EB effect. Even though neither VSM nor XMCD measurements at the Mn and Fe L edges performed at 300 K show any detectable FM moment (data not shown), we cannot exclude the possibility of a net moment at the interface, as only a small moment would be sufficient for a significant bias. Another possibility is that interfacial Fe spins are canted in plane, which would yield a net magnetic moment and could produce an EB in LSMO.

To investigate the spin configuration for LFO/LSMO exhibiting EB, we perform XMLD spectroscopy on heterostructures with LSMO thickness 8, 10, and 15 u.c. An EB is set by applying a 3-T field along the crystallographic [100] direction at 300 K, and the heterostructures are then cooled in zero field. The XMLD measurements are performed with x rays incident perpendicular to the sample surface and an azimuthal orientation of the sample such that the linear polarization of the light coincides with a ⟨100⟩ axis; see Fig. 6(a). In this geometry, an XMLD signal will only arise if there is an imbalance in AF spins oriented along the in-plane [100] and [010] directions, respectively. The FM moment of LSMO is aligned to the in-plane [100] direction by an external field. To avoid trapping of photoemitted electrons by the external field, it is applied with an angle of 20° to the sample surface; see Fig. 6(a). The full Fe L-edge XAS spectra obtained from the heterostructure with 15-u.c. LSMO at 80 K using two linear polarizations are shown in Fig. 6(b) together with the XMLD difference. The sign of the XMLD signal at the L_2 edge corresponds to a majority of Fe spins aligned parallel to the [010] direction [25,37]. As the FM is saturated along the [100] direction, there is a perpendicular alignment of Mn and Fe spins and we conclude we have coexisting spin flop and EB in our system. The dichroism signals at the L_2 edge obtained at 80 and 210 K for the three measured samples are shown in Fig. 6(c). For all three heterostructures we find a strong dichroism signal at 80 K and no evident dichroism signal at 210 K. The coexistence of EB and spin-flop at low temperatures together with the finding that the two phenomena vanishes in the same temperature range could suggest that spin-flop alignment and EB are related in this system.

The presence of EB and a predominantly perpendicular spin configuration at the LFO/LSMO interface could indicate DMI-driven EB. This asymmetric exchange interaction adds another term to the total exchange energy:

$$H = \sum_{i,j} [J_{i,j}(\vec{S}_i \cdot \vec{S}_j) + \vec{D}_{ij} \cdot (\vec{S}_i \times \vec{S}_j)],$$

where $\vec{D}_{ij}$ is the DM vector related to two neighboring spins $\vec{S}_i$ and $\vec{S}_j$. Dong *et al.* have previously discussed how interfacial DMI, i.e., considering the term including $\vec{S}_{\text{AF}}$ and $\vec{S}_{\text{FM}}$ across the interface in a G-type AF/FM system, can cause EB when the AF spin structure has a large out-of-plane component [20]. However, in the LFO/LSMO system, both the FM and AF spins are ideally in plane, and hence the interface DMI term $\vec{D}_{\text{AF,FM}} \cdot (\vec{S}_{\text{AF}} \times \vec{S}_{\text{FM}})$ will not give rise to any net moment in our system. On the other hand, bulk LFO is known to exhibit spin canting and weak ferromagnetism due to DMI between neighboring AF spins [26]. We cannot exclude that at the LFO/LSMO interface, a net moment due to such spin canting may give rise to EB. In perovskites with reduced symmetry, like orthorhombic LFO, the octahedral rotations cause staggered B–O–B bonds which causes the direction of $\vec{D}_{ij}$ to alternate when moving along $\langle 100 \rangle_{\text{pc}}$. When the direction of $\vec{D}_{ij}$ coincides with a staggered AF spin structure a net moment will result. Considering the three principal axes

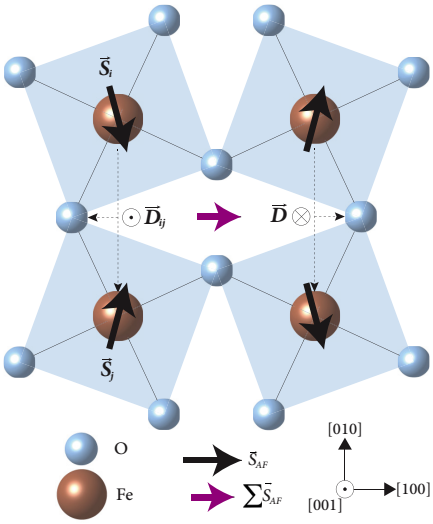

FIG. 7. Illustration of octahedral rotations around the [001] axis, causing spin canting in the (001) plane in LFO due to Dzyaloshinkii-Moriya interactions. The staggered $\vec{D}$ vectors together with the *G*-type AF order cause a net spin moment in the [100] direction, indicated by the purple vector.

of rotation for a (001)-oriented interface plane, it is the out-of-plane octahedral rotations, i.e., around the [001] axis, which will cause a $\vec{D}_{ij}$ out of plane and lead to canting in-plane; see Fig. 7. If we assume that all interfacial Fe spins are canted by an equal amount, our experimental value of σ_{int} would correspond to a canting of ∼3°, i.e., in deviation from perfect spin flop. However, this would require a larger canting angle than that reported in bulk LFO of 0.521° [26].

IV. SUMMARY

In summary, we report positive EB in epitaxial LFO/LSMO bilayers grown on (001) STO substrates. The EB persists up to a blocking temperature T_B, which is similar for all LSMO layer thicknesses and lower than both T_C of LSMO and T_N of LFO. The EB does not require field cooling, and the direction and magnitude of the EB can be tuned by applying magnetic fields above T_B. The magnitude of the EB is dependent on the LSMO layer thickness. Element-specific x-ray spectroscopy shows a predominant perpendicular spin alignment at the AF/FM interface, which emerges together with the onset of EB at T_B. Finally, we discuss possible explanations for EB in a system with spin-flop coupling.

ACKNOWLEDGMENTS

The Advanced Light Source is supported by the Director, Office of Science, Office of Basic Energy Sciences, of the US Department of Energy under Contract No. DE-AC02-05CH11231. Partial funding was obtained from the Norwegian Ph.D. Network on Nanotechnology for Microsystems, which is sponsored by the Research Council of Norway, Division for Science, under Contract No. 221860/F60. A special thanks to Magnus Moreau for fruitful discussions.

[1] M. Lorenz *et al.*, J. Phys. D **49**, 433001 (2016).
[2] H. Y. Hwang, Y. Iwasa, M. Kawasaki, B. Keimer, N. Nagaosa, and Y. Tokura, Nat. Mater. **11**, 103 (2012).
[3] A. Bhattacharya and S. J. May, Annu. Rev. Mater. Res. **44**, 65 (2014).
[4] A. Ohtomo and H. Y. Hwang, Nature (London) **427**, 423 (2004).
[5] Y. Tokura, Rep. Prog. Phys. **69**, 797 (2006).
[6] M. M. Vopson, Crit. Rev. Solid State Mater. Sci. **40**, 223 (2015).
[7] W. H. Meiklejohn and C. P. Bean, Phys. Rev. **102**, 1413 (1956).
[8] W. Zhang and K. M. Krishnan, Mater. Sci. Eng. R. **105**, 1 (2016).
[9] M. Kiwi, J. Magn. Magn. Mater. **234**, 584 (2001).
[10] A. E. Berkowitz and K. Takano, J. Magn. Magn. Mater. **200**, 552 (1999).
[11] S. Sahoo, T. Mukherjee, K. D. Belashchenko, and C. Binek, Appl. Phys. Lett. **91**, 172506 (2007).
[12] B. M. Wang, Y. Liu, B. Xia, P. Ren, and L. Wang, J. Appl. Phys. **111**, 043912 (2012).
[13] J. K. Murthy and A. Venimadhav, Appl. Phys. Lett. **103**, 252410 (2013).
[14] J. K. Murthy and P. S. A. Kumar, Sci. Rep. **7**, 6919 (2017).
[15] C. Shang, S. P. Guo, R. L. Wang, Z. G. Sun, H. B. Xiao, L. F. Xu, C. P. Yang, and Z. C. Xia, Sci. Rep. **6**, 25703 (2016).
[16] J. Nogues, D. Lederman, T. J. Moran, and I. K. Schuller, Phys. Rev. Lett. **76**, 4624 (1996).
[17] R. Rana, P. Pandey, R. P. Singh, and D. S. Rana, Sci. Rep. **4**, 4138 (2014).
[18] A. P. Chen *et al.*, Adv. Mater. **29**, 1700612 (2017).
[19] R. L. Stamps, J. Phys. D **33**, R247 (2000).
[20] S. Dong, K. Yamauchi, S. Yunoki, R. Yu, S. Liang, A. Moreo, J.-M. Liu, S. Picozzi, and E. Dagotto, Phys. Rev. Lett. **103**, 127201 (2009).
[21] F. Li, C. Song, Y. Y. Wang, B. Cui, H. J. Mao, J. J. Peng, S. N. Li, G. Y. Wang, and F. Pan, Sci. Rep. **5**, 16187 (2015).
[22] N. C. Koon, Phys. Rev. Lett. **78**, 4865 (1997).
[23] Y. Ijiri, T. C. Schulthess, J. A. Borchers, P. J. van der Zaag, and R. W. Erwin, Phys. Rev. Lett. **99**, 147201 (2007).
[24] E. Folven, A. Scholl, A. Young, S. T. Retterer, J. E. Boschker, T. Tybell, Y. Takamura, and J. K. Grepstad, Nano Lett. **12**, 2386 (2012).
[25] Y. Takamura, E. Folven, J. B. R. Shu, K. R. Lukes, B. Z. Li, A. Scholl, A. T. Young, S. T. Retterer, T. Tybell, and J. K. Grepstad, Phys. Rev. Lett. **111**, 107201 (2013).
[26] D. Treves, J. Appl. Phys. **36**, 1033 (1965).
[27] A. Monsen, J. E. Boschker, F. Macia, J. W. Wells, P. Nordblad, A. D. Kent, R. Mathieu, T. Tybell, and E. Wahlstrom, J. Magn. Magn. Mater. **369**, 197 (2014).
[28] M. Huijben, L. W. Martin, Y.-H. Chu, M. B. Holcomb, P. Yu, G. Rijnders, D. H. A. Blank, and R. Ramesh, Phys. Rev. B **78**, 094413 (2008).
[29] A. Scholl *et al.*, Science **287**, 1014 (2000).
[30] F. Y. Bruno *et al.*, Nat. Commun. **6**, 6306 (2015).

[31] J. F. Ding, O. I. Lebedev, S. Turner, Y. F. Tian, W. J. Hu, J. W. Seo, C. Panagopoulos, W. Prellier, G. Van Tendeloo, and T. Wu, Phys. Rev. B **87**, 054428 (2013).

[32] M. Vafaee, S. Finizio, H. Deniz, D. Hesse, H. Zabel, G. Jakob, and M. Klaui, Appl. Phys. Lett. **108**, 072401 (2016).

[33] H. Ohldag, A. Scholl, F. Nolting, E. Arenholz, S. Maat, A. T. Young, M. Carey, and J. Stohr, Phys. Rev. Lett. **91**, 017203 (2003).

[34] W. H. Meiklejohn, J. Appl. Phys. **33**, 1328 (1962).

[35] J. W. Seo, E. E. Fullerton, F. Nolting, A. Scholl, J. Fompeyrine, and J. P. Locquet, J. Phys.: Condens. Matter **20**, 264014 (2008).

[36] C. Sterwerf, Ph.D. thesis, Bielefeld University, 2016.

[37] E. Arenholz, G. van der Laan, F. Yang, N. Kemik, M. D. Biegalski, H. M. Christen, and Y. Takamura, Appl. Phys. Lett. **94**, 072503 (2009).

Paper B

Enhanced magnetic signal along edges of embedded epitaxial $La_{0.7}Sr_{0.3}MnO_3$ nanostructures

F.K. Olsen, A.D. Bang, E. Digernes, S.D. Slöetjes, A. Scholl, R.V. Chopdekar, T. Tybell, J.K. Grepstad and E. Folven.
Journal of Magnetic Materials and Magnetism, **521**(1), 167324, (2021).

Journal of Magnetism and Magnetic Materials 521 (2021) 167324

Contents lists available at ScienceDirect

Journal of Magnetism and Magnetic Materials

journal homepage: www.elsevier.com/locate/jmmm

Research articles

Enhanced magnetic signal along edges of embedded epitaxial $La_{0.7}Sr_{0.3}MnO_3$ nanostructures

F.K. Olsen[a,*], A.D. Bang[a], E. Digernes[a], S.D. Slöetjes[a,b], A. Scholl[b], R.V. Chopdekar[b], T. Tybell[a], J.K. Grepstad[a], E. Folven[a]

[a] Department of Electronic Systems, NTNU – Norwegian University of Science and Technology, 7491 Trondheim, Norway
[b] Advanced Light Source, Lawrence Berkeley National Laboratory, Berkeley, CA 94720, USA

ARTICLE INFO

Keywords:
Nanomagnets
LSMO
Patterned magnetic thin films
XMCD-PEEM

ABSTRACT

When thin films are patterned to realize nanoscale device geometries, maintaining their structural integrity is key to the quality of their functional properties. The introduction of new surfaces and interfaces by lateral modifications may alter material properties as well as the expected device functionality. In this study, two different techniques for nanoscale patterning of epitaxial thin films of $La_{0.7}Sr_{0.3}MnO_3$ are used to investigate the effects on their ferromagnetic properties and film crystalline structure. Nanomagnets are realized as free-standing structures and embedded ferromagnets in a paramagnetic matrix, respectively. We find that the magnetic dichroism signal in x-ray spectomicroscopy is stronger along the edges of the embedded magnets close to T_C. X-ray-diffraction measurements reveal a reduction of their in-plane lattice parameters. We discuss how in-plane stress from the nanomagnet surroundings can affect the magnetic properties in these structures.

1. Introduction

Thin film patterning is essential to the fabrication of modern electronic devices. Lithographic patterning techniques relying on etching or ion bombardment can be used to realize precisely controlled nanoscale structures [1]. However, when introducing new interfaces and surfaces on this length scale, the material properties may be perturbed. Locally, modifications of crystal and orbital structure can lead to substantial changes of functional properties such as conductivity, ferroelectricity, and magnetic order [2]. However, such changes brought about by patterning can also be exploited as a means of controlling material properties [3–5].

The strongly correlated electrons found in complex oxides imply a robust structure–property coupling, which make them good candidates for functional property engineering [2,6]. The ferromagnetic mixed-valence manganites are renowned for their metallic and magnetic nature resulting from the double-exchange mechanism [7]. Ferromagnetic $La_{0.7}Sr_{0.3}MnO_3$ (LSMO) has the highest Curie temperature (T_C) (370 K) of the manganites, shows a very large magnetoresistance dubbed colossal magnetoresistance (CMR), and has 100% spin polarization at the Fermi level [8–10]. The synthesis of high-quality thin films of LSMO by epitaxial growth on (001)-oriented $SrTiO_3$ (STO) substrates is well established [11–13]. However, tensile strain due to lattice mismatch with the STO substrate causes a reduced $T_C \sim 350$ K. This reduction in T_C has been explained in terms of a biaxial lattice distortion that increases the Jahn-Teller effect, which in turn inhibits the double exchange mechanism [14]. Furthermore, the magnetic properties of LSMO were shown to depend on parameters such as Sr content [8], oxygen stoichiometry [15], pressure [16] and strain [17]. Kozlenko et al. [16] showed that hydrostatic pressure increases the Curie temperature of LSMO, raising the question of whether this finding can be utilized to tailor the magnetic properties of nanomagnets defined in LSMO thin films.

In this study, we report on the magnetization of patterned LSMO thin film nanomagnets grown epitaxially on STO. Two different patterning techniques were adopted to realize nanomagnets embedded in a paramagnetic matrix and free-standing structures, respectively. X-ray photoemission electron microscopy measurements in combination with magnetic circular dichroism (XMCD-PEEM) were used to probe the magnetic domain structure of the patterned nanomagnets. Furthermore, x-ray diffraction (XRD) measurements on extended arrays of parallel lineshaped nanomagnets were carried out to probe the in-plane lattice parameters parallel and perpendicular to the lines.

* Corresponding author.
E-mail address: fredrik.k.olsen@ntnu.no (F.K. Olsen).

https://doi.org/10.1016/j.jmmm.2020.167324
Received 28 May 2020; Received in revised form 12 July 2020; Accepted 12 August 2020
Available online 26 August 2020

2. Experimental

Epitaxial films of LSMO, 90 unit cells (~35 nm) thick, were grown on 10 × 10 × 0.5 mm^3 Nb-doped (0.05 wt%) STO substrates by pulsed laser deposition. LSMO was deposited at 700°C in an oxygen ambient of 0.35 mbar using a KrF excimer laser with a pulse frequency of 1 Hz and a fluency of ~ 2 J/m^2. The target-to-substrate distance was 45 mm. *In situ* reflection high energy electron diffraction showed monolayer oscillations throughout the growth. After deposition, the films were annealed at the growth temperature in a 100 mbar oxygen atmosphere for 15 min. Each film was subsequently cut into four pieces. One piece was kept as a blanket (non-patterned) reference sample. Magnetization data from the reference samples was aquired using a Quantum Design vibrating sample magnetometer (VSM). The other three pieces were patterned into nanoscale thin film magnets. Masks were defined with electron beam lithography using a positive resist (CSAR62), then followed by Ar^+ ion implantation for fabrication of embedded magnetic structures, or by ion milling, using a mixture of Ar^+ and O^{2-} ions, for fabrication of free-standing magnets. The fabrication details are reported elsewhere [18]. For the patterned samples, two different designs were realized. Rectangular nanomagnets (2 × 0.8 μm^2 for embedded and 2 × 1 μm^2 for free standing) were prepared for magnetic domain imaging, and extended arrays (2.5 × 2.5 mm^2) of parallel lines, 500 nm wide with a pitch of 1 μm, were prepared for XRD measurements. Additionally, one sample was patterned with thinner embedded lines, 300 nm wide with a pitch of 600 nm. In the presented work, we will describe the crystalline orientations in terms of pseudocubic lattice parameters. All nanostructures were defined with their long axis parallel to in-plane ⟨110⟩ crystalline axes, which are the magnetic easy axes in (001)-oriented LSMO thin films [19]. The magnetic domain structure was imaged using the PEEM-3 microscope at the Advanced Light Source. The XMCD-PEEM images were measured at the Mn L_3 absorption edge with the x-rays incident at 30° with the sample surface parallel to the nanomagnets' long axis. Surface topography images were acquired using a Veeco Multimode V atomic force microscope, and the XRD measurements were taken with a Bruker D8 x-ray diffractometer.

3. Results

Fig. 1 shows schematics, AFM images, and AFM line scans of the embedded rectangular magnets [Fig. 1(a)] and the arrays of free-standing extended line magnets [Fig. 1 (b)]. The AFM linescan in Fig. 1(a) of a rectangular nanomagnet shows the characteristic topography of the embedded structures, i.e., well-defined nanomagnets with a ~6 nm height increase of the surrounding implanted regions. This difference is attributed to swelling as result of the Ar^+ ion implantation and is consistent with previous reports using this patterning technique [20,21]. Both AFM micrographs show little surface roughness. The topography of the free-standing structures appears from the AFM line scan of the extended line magnets in Fig. 1(b) and show well-defined parallel lines with a steep sidewall profile. The lines are 460 ± 40 nm wide with trenches 50–60 nm deep, exceeding the LSMO film thickness of 35 nm. The reduction in line-width relative to the nominal 500 nm width is attributed to over-exposure of the positive electron beam resist. Fig. 1(c) shows the temperature dependence of the saturation magnetization in a reference blanket LSMO film, as measured by VSM. The magnetization curve shows expected LSMO behaviour [22], and T_C is estimated at 345 K. Fig. 1(d) shows an XMCD-PEEM image of a rectangular nanomagnet recorded at 330 K. The arrows indicate how the direction of the magnetization is related to the contrast. In all presented XMCD-PEEM data, the direction of the incoming light is horizontal from left to right in the figures. We note that while magnetization parallel or antiparallel to the incoming light is clearly distinguishable, perpendicular oriented magnetization cannot be distinguished from the paramagnetic matrix surrounding the nanomagnet. As XMCD-PEEM is a surface sensitive technique, the signal is obtained from the top ~5 nm

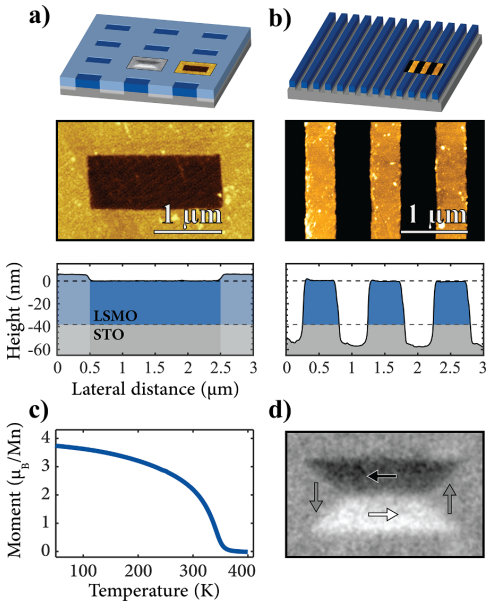

Fig. 1. Schematics, atomic force microscopy images and corresponding line scans of a) embedded rectangular magnets and b) free-standing lines. The color scale in the two AFM images is normalized to the max/min values for the scan in a). c) Saturation magnetization as function of temperature for a blanket LSMO film, measured in an applied field of 200 mT from 50 to 400 K. d) XMCD-PEEM image of a rectangular magnet recorded at 330 K. The arrows indicate the magnetization direction.

of the 35 nm thick film. It should also be noted that the temperatures is not measured at the sample surface in the VSM and PEEM-3 setups. Thus, a slight discrepancy between the measured temperatures is to be expected.

Fig. 2(a) shows XMCD-PEEM images of the embedded nanomagnets at temperatures near T_C. At 330 K, the magnetic domain patterns are clearly visible and take the form of a single or double Landau flux-closure, characteristic of rectangular magnets this size [23–25]. Upon heating the sample to 345 K, i.e., the T_C measured by VSM for the non-structured film, the overall dichroism signal is strongly reduced. Strikingly, at this temperature the XMCD-PEEM images show a stronger dichroism signal along the edges of the nanomagnets compared to that of their interior. The enhanced signal extends inwards from the edges ~150 nm, where the dichroism signal becomes indistinguishable from the surrounding paramagnetic matrix. When increasing the temperature to 360 K, the magnetic contrast along the edges disappears as the LSMO nanostructures rise above T_C. Magnetization is recovered upon subsequent lowering of the temperature to 330 K, with every rectangular nanomagnet entering a single flux-closure domain state.

XMCD-PEEM data for the rectangular free-standing nanomagnets is shown in Fig. 2(b). No enhanced dichroism signal is found along the nanostructure edges in such magnets for temperatures close to T_C. This suggests that the presence of a surrounding matrix is important to the enhanced dichroism signal near the edges of the embedded structures. We note, however, that the magnetic dichroism signal disappears at significantly lower temperature for the free-standing magnets than for the embedded magnets. X-ray absorption spectra taken on and in-between the magnets are compared in Fig. 2. For the free-standing magnets a distinct Mn^{2+} signal is obtained [26], indicating a reduced oxygen content in this sample [27]. It is well established that oxygen deficiency weakens the ferromagnetic properties in LSMO [12]. As the

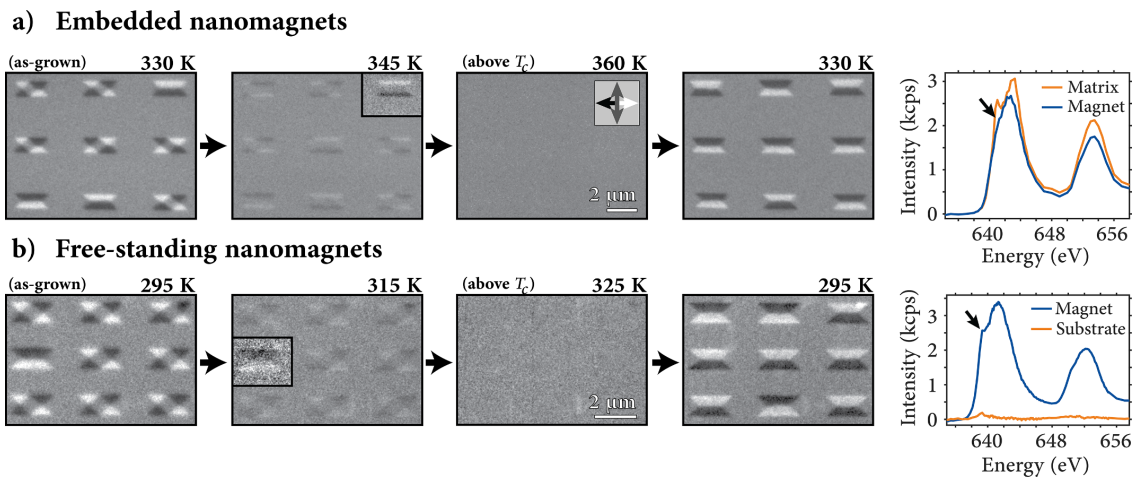

Fig. 2. X-ray photoemission electron microscopy images of a) embedded and b) free-standing nanomagnets recorded at temperatures around T_C in chronological order. The contrast is normalized to that measured at 330 K for embedded and at 295 K for free-standing nanomagnets. Marked with a black frame in the second column of images are magnets shown with maximized contrast for these selected structures. X-ray absorption spectra recorded on and in-between the magnets are shown on the right. The arrows in these graphs indicate the position of the Mn^{2+} peak.

films were grown using the same conditions for both samples, it is likely that the loss of oxygen is caused by the patterning process for the etched, free-standing samples. In particular, the ion milling process tends to harden the resist mask, and the following resist removal can be difficult. Thus, multiple exposures to the developing chemicals were required in the process and it is not unlikely that this processing causes some loss of oxygen in the LSMO thin film.

Upon close inspection of the magnetic dichroism signal near T_C for the embedded nanomagnets, we note an evolution of the domain structure for magnets with double flux-closures at the outset. XMCD-PEEM images of three selected rectangular magnets are shown in Fig. 3. At 330 K, the two flux-closures in each magnet are similar in size, and the domain wall positions along the edges are kept in place by the vortex structures. As the temperature increases to 340 K, the XMCD contrast in the central part of the magnets fades, and at 345 K magnetic contrast can be discerned along the nanomagnets' edges, only. Concurrent with the loss of magnetic contrast in the central part of the magnets, we find a change in domains near the nanomagnet edges – one of the two domains along the horizontal edges grows at the expense of the other. This finding indicates that the magnetic order in the central part of the magnets is lost, or at least too weak, to keep the domain walls stable along the edge at 345 K. After heating to 360 K and subsequently cooling to 330 K, a single flux-closure domain pattern appears in all nanomagnets. This observation implies that the magnet's

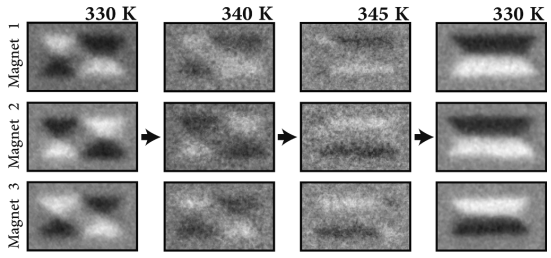

Fig. 3. X-ray photoemission electron microscopy images of three selected rectangular nanomagnets, showing an evolution in the domain pattern with increased temperature. The image contrast is normalized separately for each temperature.

edges, as well as their central sections have been heated above the magnetic ordering temperature.

A possible explanation for the enhanced dichroism signal along the edges of embedded nanomagnets is lateral stress imposed by the surrounding ion-implanted paramagnetic matrix, which the AFM investigation showed to be swollen. The dependence of T_C on isotropic pressure for LSMO was tested by Kozlenko et al. [16] and estimated at 4.3 K/GPa. In order to explore lateral pressure-induced changes in the LSMO lattice parameters for our patterned thin films, samples with extended arrays of parallel lines were investigated using XRD. In the following, the [110] direction is defined to be parallel to the patterned lines. The in-plane lattice parameters parallel and perpendicular to the lines were probed by recording reciprocal space maps (RSM) around {113} reflections. The {113} planes have $\vec{d}_{hkl}$ in-plane components along the ⟨110⟩ directions, i.e., either [110] which is parallel, or [1$\bar{1}$0] which is perpendicular to the lines. Schematic of the XRD geometry and the RSMs taken around the {113} peaks are shown in Fig. 4. The reference blanket film displays similar RSMs for all of the four equivalent {113} planes. Therefore, only one reference map is depicted in Fig. 4. The blanket film has the LSMO film peak aligned with that of the STO in the [hk0] direction, i.e., the film is fully strained to the substrate. The position of the LSMO peak in the [00l] direction corresponds to an out-of-plane (pseudocubic) lattice parameter of ~ 3.85 Å. This number is in accordance with reported parameters for epitaxial films of (001)-oriented LSMO/STO [11,28]. The diffuse peaks observed on either side of the LSMO film peak in the blanket film can be attributed to the presence of a 4-variant monoclinic structural distortion due to symmetry mismatch between rhombohedral LSMO and cubic STO [29].

Fig. 4 (b-d) show RSMs measured around the (113) peak for the patterned samples. The LSMO film peaks show no shift in the [hk0] direction, i.e., no change in the in-plane strain along the lines. However, the film peak is shifted towards the STO peak in the [00l] direction, indicating a larger out-of-plane lattice parameter compared to blanket films. The shift corresponds to a change in lattice parameter of 0.01 Å (~0.3%) for 500 nm wide lines and of 0.02 Å (~0.5%) for 300 nm wide lines. The signal-to-noise ratio is reduced compared to that recorded for blanket film samples. We note that a reduction in the signal-to-noise ratio is expected after patterning, as half the volume of the LSMO probed is either rendered amorphous (embedded line arrays) or removed (free-standing line arrays).

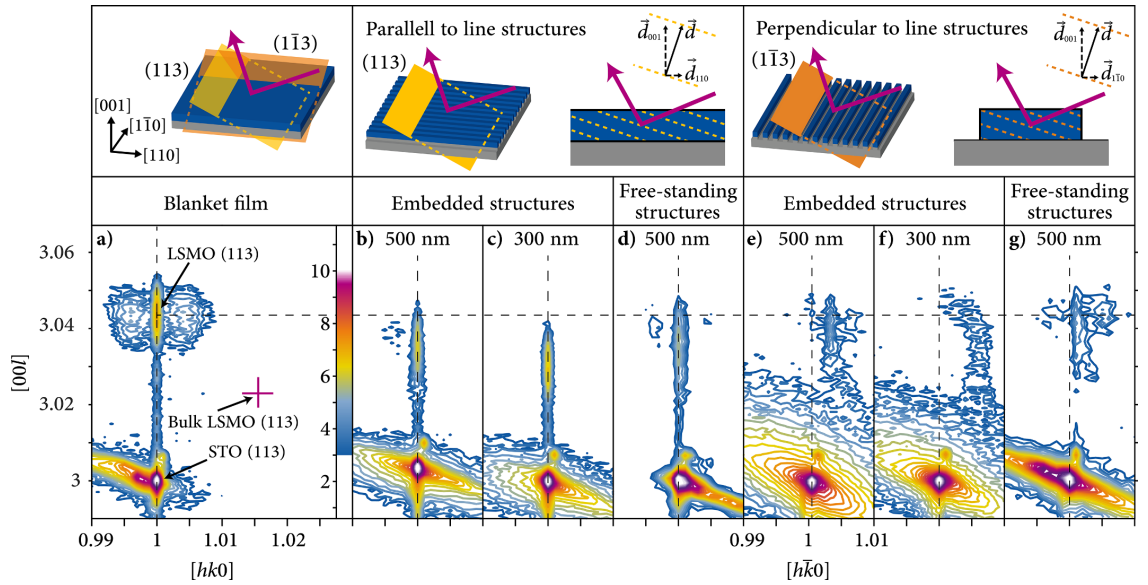

Fig. 4. XRD experimental geometry and reciprocal space maps recorded around the STO (113) diffraction peaks for a blanket film sample (a) and patterned structures (b-g). The scale on the x- and y-axes is given in units of *hkl* reciprocal lattice vectors. Dashed lines are introduced as a guide to the eye, indicating the film peak position for the blanket film. The position of the bulk LSMO (113) diffraction peak is indicated in a) for reference. The intensity scale is in ln(cps).

The RSMs of the (1$\bar{1}$3) diffraction peaks for the embedded line structures [Fig. 4 (e,f)] show a significant shift of the LSMO film peaks along [$h\bar{k}$0]. No overlap of the film and STO diffraction peaks is found in the in-plane direction. This suggests relaxation of the (1$\bar{1}$3) lattice parameter across the full linewidth. The shift along [$h\bar{k}$0] suggests that the LSMO pseudocubic unit cell is compressed along the [1$\bar{1}$0] direction, i.e., perpendicular to the patterned lines, while remaining fully strained to STO along the lines. For the fully strained blanket film the unit cell face diagonal is 5.523 Å. For the 500 nm lines it is reduced by 0.02 Å (~0.4%), and for the 300 nm lines, the reduction is 0.03 Å (~0.5%). Furthermore, the (1$\bar{1}$3) film peaks are found to be broadened and have a reduced amplitude compared to that found for (113). This finding suggests a slight variation of the LSMO lattice parameter in the in-plane direction across the line structures. The observation of one single peak rather than two, which one could expect from the XMCD-PEEM data, indicates that the lattice is distorted throughout the full width of both the 500 nm and the 300 nm lines. Since the line structures are only 500 nm and 300 nm wide, and the rectangles measured in XMCD-PEEM are 1 μm wide, it is not unlikely that the extension of strain imposed at the edges can be different. For the out-of-plane lattice parameter, a shift of the (1$\bar{1}$3) film peak towards the STO peak is observed for both linewidths, in keeping with the (113) RSM data. A minor shift of the diffraction peaks in-plane along [$h\bar{k}$0] can also be discerned for the (1$\bar{1}$3) RSMs of free-standing lines [Fig. 4 (g)], corresponding to a reduction of the pseudocubic unit cell along [1$\bar{1}$0] by 0.006 Å (~0.1%). This shift suggests that formation of free-standing lines also leads to relaxation of the tensile-strained LSMO film. However, the effect is much reduced compared to that observed for embedded structures.

From the XRD data summarized above, it is evident that the crystal structure of LSMO is affected by the patterning process. In particular, the embedded line magnets display an anisotropic modification of the in-plane lattice parameters. All the RSM data is consistent with an increase in the out-of-plane lattice parameter compared to blanket films, which may be expected from the measured relaxation of the in-plane epitaxial strain perpendicular to the nanomagnet lines. The XRD data is consistent with local stress imposed on the microstructures by swelling of the ion-implanted matrix. In bulk LSMO, Young's modulus is reported to be ~120 GPa [30,31]. Using the data from 300 nm wide lines, a change in lattice parameters of 0.5% would correspond to a pressure 0.6 GPa imposed on the line magnet sidewalls. With the pressure dependence of T_C reported by Kozlenko et al. [16], the corresponding increase in T_C would come to ~ 3 K, which is reasonably consistent with the XMCD-PEEM data. However, the variation in T_C with in-plane stress for nanostructured epitaxial films may differ from that of bulk LSMO for several reasons, such as the biaxial tensile strain from the substrate and the additional anisotropic distortion of the film crystalline structure.

4. Conclusions

In summary, the impact of two different patterning methods on the magnetic and structural properties of nanostructured thin films of LSMO was investigated. In particular, we report an increased magnetic dichroism signal near T_C along the edges of embedded nanomagnets, extending laterally ~150 nm inwards from the magnet edges. XRD measurements show that the patterning process leads to an anisotropic change of in-plane lattice parameters for line-shaped LSMO nanomagnets, notably a smaller lattice parameter perpendicular to the magnet-matrix interface. We argue that the enhanced dichroism signal can be attributed to lateral stress from swelling of the paramagnetic matrix surrounding the embedded nanomagnets upon Ar^+ ion implantation, and corresponding modification of the LSMO lattice parameters.

CRediT authorship contribution statement

F.K. Olsen: Conceptualization, Investigation, Formal analysis, Data curation, Visualization, Validation, Writing - original draft. **A.D. Bang:** Investigation. **E. Digernes:** Investigation. **S.D. Slöetjes:** Investigation. **A. Scholl:** Resources, Software. **R.V. Chopdekar:** Resources, Software. **T. Tybell:** Conceptualization, Writing - review & editing. **J.K. Grepstad:** Conceptualization, Writing - review & editing. **E. Folven:** Conceptualization, Project administration, Funding acquisition,

Supervision, Validation, Writing - review & editing.

Declaration of Competing Interest

The authors declare that they have no known competing financial interests or personal relationships that could have appeared to influence the work reported in this paper.

Acknowledgements

A special thanks to Kristoffer Kjærnes for fruitful discussions on XRD. The Advanced Light Source is supported by the Director, Office of Science, Office of Basic Energy Sciences, of the US Department of Energy under Contract No. DE-AC02-05CH11231. Nanoscale patterning and AFM imaging was carried out at NTNU NanoLab, NorFab. The Research Council of Norway is acknowledged for support to the Norwegian Micro- and Nanofabrication Facility, NorFab, Project No. 245963/F50. Partial funding was obtained from the Norwegian Ph.D. Network on Nanotechnology for Microsystems, which is sponsored by the Research Council of Norway, Division for Science, under Contract No. 221860/F60.

References

[1] J.I. Martin, J. Nogues, K. Liu, J.L. Vicent, I.K. Schuller, Ordered magnetic nanostructures: fabrication and properties, J. Magn. Magn. Mater. 256 (2003) 449–501, https://doi.org/10.1016/S0304-8853(02)00898-3.

[2] H.Y. Hwang, Y. Iwasa, M. Kawasaki, B. Keimer, N. Nagaosa, Y. Tokura, Emergent phenomena at oxide interfaces, Nature Mater. 11 (2012) 103–113, https://doi.org/10.1038/Nmat3223.

[3] S.N. Kim, Y.J. Nam, Y.D. Kim, J.W. Choi, H. Lee, S.H. Lim, Formation of magnetic anisotropy by lithography, Sci. Rep. 6 (2016), https://doi.org/10.1038/srep26709.

[4] N. Martin, J. McCord, A. Gerber, T. Strache, T. Gemming, I. Monch, N. Farag, R. Schafer, J. Fassbender, E. Quandt, L. Schultz, Local stress engineering of magnetic anisotropy in soft magnetic thin films, Appl. Phys. Lett. 94 (2009), https://doi.org/10.1063/1.3079664.

[5] B.M. Lefler, T. Duchon, G. Karapetrov, J.Y. Wang, C.M. Schneider, S.J. May, Reconfigurable lateral anionic heterostructures in oxide thin films via lithographically defined topochemistry, Phys. Rev. Mater. 3 (2019), https://doi.org/10.1103/PhysRevMaterials.3.073802.

[6] M. Lorenz, M.S.R. Rao, T. Venkatesan, E. Fortunato, P. Barquinha, R. Branquinho, D. Salgueiro, R. Martins, E. Carlos, A. Liu, F.K. Shan, M. Grundmann, H. Boschker, J. Mukherjee, M. Priyadarshini, N. DasGupta, D.J. Rogers, F.H. Teherani, E.V. Sandana, P. Bove, K. Rietwyk, A. Zaban, A. Veziridis, A. Weidenkaff, M. Muralidhar, M. Murakami, S. Abel, J. Fompeyrine, J. Zuniga-Perez, R. Ramesh, N.A. Spaldin, S. Ostanin, V. Borisov, I. Mertig, V. Lazenka, G. Srinivasan, W. Prellier, M. Uchida, M. Kawasaki, R. Pentcheva, P. Gegenwart, F.M. Granozio, J. Fontcuberta, N. Pryds, The 2016 oxide electronic materials and oxide interfaces roadmap, J. Phys. D 49 (2016), https://doi.org/10.1088/0022-3727/49/43/433001.

[7] C. Zener, Interaction between the *d*-shells in the transition metals. II. Ferromagnetic compounds of manganese with perovskite structure, Phys. Rev. 82 (1951) 403–405, https://doi.org/10.1103/PhysRev.82.403.

[8] A. Urushibara, Y. Moritomo, T. Arima, A. Asamitsu, G. Kido, Y. Tokura, Insulator-metal transition and giant magnetoresistance in $La_{1-X}Sr_xMnO_3$, Phys. Rev. B 51 (1995) 14103–14109, https://doi.org/10.1103/PhysRevB.51.14103.

[9] Y. Tokura, Y. Tomioka, Colossal magnetoresistive manganites, J. Magn. Magn. Mater. 200 (1999) 1–23, https://doi.org/10.1016/S0304-8853(99)00352-2.

[10] M. Bowen, M. Bibes, A. Barthelemy, J.P. Contour, A. Anane, Y. Lemaitre, A. Fert, Nearly total spin polarization in $La_{2/3}Sr_{1/3}MnO_3$ from tunneling experiments, Appl. Phys. Lett. 82 (2003) 233–235, https://doi.org/10.1063/1.1534619.

[11] A. Monsen, J.E. Boschker, F. Macia, J.W. Wells, P. Nordblad, A.D. Kent, R. Mathieu, T. Tybell, E. Wahlström, Thickness dependence of dynamic and static magnetic properties of pulsed laser deposited $La_{0.7}Sr_{0.3}MnO_3$ films on $SrTiO_3$(001), J. Magn. Magn. Mater. 369 (2014) 197–204, https://doi.org/10.1016/j.jmmm.2014.06.038.

[12] M. Huijben, L.W. Martin, Y.-H. Chu, M.B. Holcomb, P. Yu, G. Rijnders, D.H.A. Blank, R. Ramesh, Critical thickness and orbital ordering in ultrathin $La_{0.7}Sr_{0.3}MnO_3$ films, Phys. Rev. B 78 (2008), https://doi.org/10.1103/PhysRevB.78.094413.

[13] J.E. Boschker, E. Folven, A.F. Monsen, E. Wahlstrom, J.K. Grepstad, T. Tybell, Consequences of high adatom energy during pulsed laser deposition of $La_{0.7}Sr_{0.3}MnO_3$, Cryst. Growth Des. 12 (2012) 562–566, https://doi.org/10.1021/cg201461a.

[14] A.J. Millis, T. Darling, A. Migliori, Quantifying strain dependence in “colossal” magnetoresistance manganites, J. Appl. Phys. 83 (1998) 1588–1591, https://doi.org/10.1063/1.367310.

[15] J. Dho, N.H. Hur, I.S. Kim, Y.K. Park, Oxygen pressure and thickness dependent lattice strain in $La_{0.7}Sr_{0.3}MnO_3$ films, J. Appl. Phys. 94 (2003) 7670–7674, https://doi.org/10.1063/1.1628831.

[16] D.P. Kozlenko, I.N. Goncharenko, B.N. Savenko, V.I. Voronin, High pressure effects on the crystal and magnetic structure of $La_{0.7}Sr_{0.3}MnO_3$, J. Phys.-Condens. Mat. 16 (2004) 6755–6762, https://doi.org/10.1088/0953-8984/16/37/011.

[17] F. Tsui, M.C. Smoak, T.K. Nath, C.B. Eom, Strain-dependent magnetic phase diagram of epitaxial $La_{0.67}Sr_{0.33}MnO_3$ thin films, Appl. Phys. Lett. 76 (2000) 2421–2423, https://doi.org/10.1063/1.126363.

[18] A.D. Bang, I. Hallsteinsen, R.V. Chopdekar, F.K. Olsen, S.D. Sloetjes, K. Kjaernes, E. Arenholz, E. Folven, J.K. Grepstad, Shape-imposed anisotropy in antiferromagnetic complex oxide nanostructures, Appl. Phys. Lett. 115 (2019), https://doi.org/10.1063/1.5116806.

[19] L.M. Berndt, V. Balbarin, Y. Suzuki, Magnetic anisotropy and strain states of (001) and (110) colossal magnetoresistance thin films, Appl. Phys. Lett. 77 (2000) 2903–2905, https://doi.org/10.1063/1.1321733.

[20] Y. Takamura, R.V. Chopdekar, A. Scholl, A. Doran, J.A. Liddle, B. Harteneck, Y. Suzuki, Tuning magnetic domain structure in nanoscale $La_{0.7}Sr_{0.3}MnO_3$ islands, Nano Lett. 6 (2006) 1287–1291, https://doi.org/10.1021/nl060615f.

[21] E. Folven, T. Tybell, A. Scholl, A. Young, S.T. Retterer, Y. Takamura, J.K. Grepstad, Antiferromagnetic Domain Reconfiguration in Embedded $LaFeO_3$ Thin Film Nanostructures, Nano Lett. 10 (2010) 4578–4583, https://doi.org/10.1021/nl1025908.

[22] F.K. Olsen, I. Hallsteinsen, E. Arenholz, T. Tybell, E. Folven, Coexisting spin-flop coupling and exchange bias in $LaFeO_3/La_{0.7}Sr_{0.3}MnO_3$ heterostructures, Phys. Rev. B 99 (2019), https://doi.org/10.1103/PhysRevB.99.134411.

[23] K.X. Xie, X.P. Zhang, W.W. Lin, P. Zhang, H. Sang, Magnetization splitting in Landau and diamond-domain structures: Dependence on exchange interaction, anisotropy, and size, Phys. Rev. B 84 (2011), https://doi.org/10.1103/PhysRevB.84.054460.

[24] A.D. Bang, F.K. Olsen, S.D. Sloetjes, A. Scholl, S.T. Retterer, C.A.F. Vaz, T. Tybell, E. Folven, J.K. Grepstad, Magnetic domain formation in ultrathin complex oxide ferromagnetic/antiferromagnetic bilayers, Appl. Phys. Lett. 113 (2018), https://doi.org/10.1063/1.5047271.

[25] S.D. Sloetjes, H.H. Urdahl, J.K. Grepstad, E. Folven, Tailoring the magnetic order in a supermagnetic metamaterial, AIP Adv. 7 (2017), https://doi.org/10.1063/1.4978319.

[26] M. Khan, E. Suljoti, A. Singh, S.A. Bonke, T. Brandenburg, K. Atak, R. Golnak, L. Spiccia, E.F. Aziz, Electronic structural insights into efficient MnO_x catalysts, J. Mater. Chem. A 2 (2014) 18199–18203, https://doi.org/10.1039/c4ta04185b.

[27] S.W. Jin, X.Y. Zhou, W.B. Wu, C.F. Zhu, H.M. Weng, H.Y. Wang, X.F. Zhang, B.J. Ye, R.D. Han, Vacancy defects in epitaxial $La_{0.7}Sr_{0.3}MnO_3$ thin films probed by a slow positron beam, J Phys. D. 37 (2004) 1841–1844, https://doi.org/10.1088/0022-3727/37/13/017.

[28] H. Boschker, M. Huijben, A. Vailionis, J. Verbeeck, S. van Aert, M. Luysberg, S. Bals, G. van Tendeloo, E.P. Houwman, G. Koster, D.H.A. Blank, G. Rijnders, Optimized fabrication of high-quality $La_{0.67}Sr_{0.33}MnO_3$ thin films considering all essential characteristics, J Phys. D. 44 (2011), https://doi.org/10.1088/0022-3727/44/20/205001.

[29] J.E. Boschker, A.F. Monsen, M. Nord, R. Mathieu, J.K. Grepstad, R. Holmestad, E. Wahlstrom, T. Tybell, In-plane structural order of domain engineered $La_{0.7}Sr_{0.3}MnO_3$ thin films, Philos. Mag. 93 (2013) 1549–1562, https://doi.org/10.1080/14786435.2012.747010.

[30] S. Giraud, J. Canel, Young's modulus of some SOFCs materials as a function of temperature, J. Eur. Ceram. Soc. 28 (2008) 77–83, https://doi.org/10.1016/j.jeurceramsoc.2007.05.009.

[31] G. Fehringer, S. Janes, M. Wildersohn, R. Clasen, Proton-conducting ceramics as electrode/electrolyte – materials for SOFCs: preparation, mechanical and thermal-mechanical properties of thermal sprayed coatings, material combination and stacks, J. Eur. Ceram. Soc. 24 (2004) 705–715, https://doi.org/10.1016/S0955-2219(03)00262-0.

Paper C

The effect of $LaFeO_3$ on $La_{0.7}Sr_{0.3}MnO_3$ line structures

F.K. Olsen, Y. Lever, A.D. Bang, J.K. Grepstad, E. Folven.
Paper to be submitted.

Chapter 6

Counclusion and outlook

In this work, we have examined the ferromagnetic properties of $La_{0.7}Sr_{0.3}MnO_3$ as thin films and in $LaFeO_3$/$La_{0.7}Sr_{0.3}MnO_3$ heterostructures. The work has focused on two main subjects; (1) the effect of an antiferromagnetic $LaFeO_3$ layer on $La_{0.7}Sr_{0.3}MnO_3$ thin films and (2) the impact of patterning method of nanomagnets realized in the films.

In the work on $La_{0.7}Sr_{0.3}MnO_3$ thin films and $LaFeO_3$/$La_{0.7}Sr_{0.3}MnO_3$ bilayers presented in paper 1, we find the presence of the $LaFeO_3$ layer to cause an increase in the coercive field, and an exchange bias effect to emerge for thin layers of $La_{0.7}Sr_{0.3}MnO_3$. More specifically, we find that:

- The coercive field of $La_{0.7}Sr_{0.3}MnO_3$ is enhanced by the presence of the $LaFeO_3$ layer. The enhancement is dependent on the thickness of the ferromagnetic layer, i.e., it increases as the $La_{0.7}Sr_{0.3}MnO_3$ thickness is reduced.
- An exchange bias effect emerges in this system when the thickness of the $La_{0.7}Sr_{0.3}MnO_3$ layer is 20 unit cells or less.
- The direction of the exchange bias field is positive, i.e., the hysteresis loop shifts in the same direction as the applied cooling field.
- No vertical shift is observed in the magnetization loops, and no net magnetic moment is detected on Fe by x-ray magnetic circular dichroism measurements. This implies that only a small moment may be needed for the bias to manifest in the system, or that a net moment at the interface is cancelled by another net moment.
- The exchange bias can be induced without a field-cooling procedure, i.e., the system posesses a spontaneous exchange bias. Instead of field-cooling, the effect can be obtained by heating the bilayer system to elevated temperature, applying a setting field and subsequently cooling in zero field.
- The magnitude of the exchange bias is dependent on the thickness of the ferromagnetic layer. Specifically, it is inversely proportional to the thickness of $La_{0.7}Sr_{0.3}MnO_3$.
- The magnitude of the exchange bias is dependent on temperature at which the setting field is applied, and the strength of the setting field. We have presented a phase diagram for the temperature range 50 - 400 K and field strength 0 - 3 T.
- The magnitude of the exchange bias decreases as the temperature is increased, up to a blocking temperature estimated in the range 150 - 200 K.

- Upon heating above the blocking temperature and subsequent cooling, a large portion of the exchange bias is preserved.
- The spin-flop coupling previously reported in (10 unit cells)/(90 unit cells) $LaFeO_3$/$La_{0.7}Sr_{0.3}MnO_3$ heterostructures is found to prevail down to 8 unit cells ($\sim$ 3 nm) of $La_{0.7}Sr_{0.3}MnO_3$ thickness.
- Spin-flop is found to be strongest at low temperature (80 K is the lowest measured) and no evident spin-flop can be found at high temperature (210 K). This demonstrates a temperature dependence of the spin-flop coupling in the system.

The finding of exchange bias coexisting with a spin-flop coupling at the interface of $LaFeO_3$/$La_{0.7}Sr_{0.3}MnO_3$ is peculiar since the spin-flop coupling is assumed to require a spin-compensated antiferromagnetic spin-plane at the interface, while an exchange bias implies a net magnetic moment in order to pin the magnetization of the ferromagnet. Therefore, we discussed the possibility of weak ferromagnetism in $LaFeO_3$, induced by Dzyolashinskii-Moriya interactions, to be present at the interface. We showed that an (001)-plane in $LaFeO_3$ may have a net moment arising from canted antiferromagnetic spins, even though a macroscopic moment is cancelled by this net moment alternating in (001) planes. To validate this however, further investigation is necessary.

In the work on patterned $La_{0.7}Sr_{0.3}MnO_3$ thin films presented in paper 2, we study the impact of two patterning methods on the magnetic properties of the nanomagnets. Specifically, we investigate the difference between nanomagnets embedded in a non-magnetic matrix and free-standing nanomagnets oriented along a [110] crystalline direction. We find the following:

- In rectangular nanomagnets close to the Curie temperature, the x-ray magnetic circular dichroism signal is stronger along the edges for the embedded nanomagnets than in their interior. This is not observed in free-standing nanomagnets.
- At 345 K, which is the Curie temperature of the ferromagnet, the enhanced dichroism signal extends $\sim$ 150 nm inwards from the nanomagnets edges while the center of the nanomagnets give no signal. This indicates that the ferromagnetic order is lost in the center while it still persists along the edges.
- At 345 K, a change in the ferromagnetic domain structure in the edge-region (i.e., the region of enhanced dichroism signal) is found. Specifically, domain walls have moved which at lower temperatures are kept in place to uphold

symmetry in vortex flux closure domain patterns. This finding also supports that the ferromagnetic ordering is weak in the magnet center, while it remains strong enough to produce a dichroism signal at the edges.

- X-ray diffraction measurements on line-shaped nanomagnets reveal a change in in-plane and out-of-plane lattice parameters as compared to blanket films. While blanket films are found to be fully strained to the $SrTiO_3$ substrate, both embedded and free-standing line-shaped nanomagnets show larger out-of-plane lattice parameter and a reduced lattice parameter in-plane, perpendicular to the long-axis of the lines. Along the long-axis of the lines, no change in in-plane lattice paramter is found. The patterning methods therefore impose an asymmetric change in lattice parameters.

- The change in in-plane lattice parameters is larger for embedded nanomagnets (0.5 %) than free-standing nanomagnets (0.1 %). This illustrates a difference of the patterning methods, in particular the importance of the matrix material.

For embedded nanomagnets, exposed areas of $La_{0.7}Sr_{0.3}MnO_3$ are ion-bombarded to make up the embedding matrix material, and the bombardment process causes a swelling of the material volume. It is therefore likely that this swelling imposes the difference seen in change of in-plane lattice parameters of the nanomagnets. Based on the changes in lattice parameters, we estimated the impact of pressure from the matrix and found an expected $\sim$ 3 K increase in the Curie temperature. It is however uncertain that the enhanced signal is due to increased Curie temperature, and this could be pursued in a future study.

In the work on patterned $LaFeO_3$/$La_{0.7}Sr_{0.3}MnO_3$ bilayers presented in paper 3, the magnetization properties of line-shaped nanomagnets oriented along a [100] crystalline direction is investigated by vibrating sample magnetometry. In this system, we obtain the combination of anisotropy effects imposed by interface coupling to an antiferromagnet, and by shape due to patterning. We find the following:

- Both patterning methods, i.e., which realize embedded and free-standing line-shaped nanomagnets respectively, cause a significant increase in coercivity in $La_{0.7}Sr_{0.3}MnO_3$ single layers. This is attributed to shape-imposed anisotropy. The increase is largest for embedded nanomagnets.

- The addition of the $LaFeO_3$ layer causes a decrease in coercivity ($\sim$ 30 %) for line-shaped nanomagnets. This is found for both patterning methods and for all measured temperatures below the curie temperature (50 - 400 K).

We suggest that the difference between embedded and free-standing nanomagnets seen in coercivity is could be due to magnetostriction imposed by the surrounding matrix for the embedded nanomagnets. In paper 2, we elaborated on the impact on lattice parameters for the [110]-oriented nanomagnets. Still, the impact may be different for the [100]-orientation and further analysis is needed to validate this proposal. For instance, an x-ray diffraction study could be done to investigate whether the changes in lattice parameters are similar for the [100]-orientation. Regarding the effect of $LaFeO_3$, it is peculiar that the coercivity is reduced, since in blanket films, an $LaFeO_3$ layer has the opposite effect. Nanomagnets oriented along the [100]-orientation has shown distinct anisotropy in the antiferromagnetic $LaFeO_3$, and this can affect the ferromagnetic switching properties of $La_{0.7}Sr_{0.3}MnO_3$ via exchange coupling. As a suggestion for future work, a detailed investigation of the spin orientation in $LaFeO_3$ for this orientation as function of temperature would be valuable. This would also shed light on the connection between spin-flop coupling and switching anisotropy imposed by $LaFeO_3$. For instance, it could be that a spin-flop coupling and reduction of coercivity in the [100]-oriented nanomagnets are unrelated. In the [110]-orientation, a spin reorientation transition has been reported, while a study on the switching properties of nanomagnets in this orientation showed no significant changes across the same temperature range. This could also be the case for the [100]-orientation. However, in the [100]-orientation, $LaFeO_3$ has a different effect, namely a ~ 30 % reduction of the coercive field. It would be strange if the presence of spin-flop coupling or not has no significance for this reduction, since the exchange interaction between neighbouring atoms, which is believed to be the essential coupling mechanism at the interface, rely on the relative orientation of the spins.

In conclusion, the $LaFeO_3$/$La_{0.7}Sr_{0.3}MnO_3$ system diplays intriguing properties which are tunable by design. This materials system holds the potential for use in future spintronic applications as well as being an interesting model system for understanding magnetic phenomena in nanostructures.

Bibliography

[1] G. E. Moore. Cramming more components onto integrated circuits (reprinted from electronics, pg 114-117, april 19, 1965). *Proceedings of the Ieee*, 86(1):82–85, 1998.

[2] T. N. Theis and P. M. Solomon. It's time to reinvent the transistor! *Science*, 327(5973):1600–1601, 2010.

[3] A. Hirohata, K. Yamada, Y. Nakatani, I. L. Prejbeanu, B. Dieny, P. Pirro, and B. Hillebrands. Review on spintronics: Principles and device applications. *Journal of Magnetism and Magnetic Materials*, 509, 2020.

[4] B. Dieny, I. L. Prejbeanu, K. Garello, P. Gambardella, P. Freitas, R. Lehndorff, W. Raberg, U. Ebels, S. O. Demokritov, J. Akerman, A. Deac, P. Pirro, C. Adelmann, A. Anane, A. V. Chumak, A. Hirohata, S. Mangin, S. O. Valenzuela, M. C. Onbasli, M. D'Aquino, G. Prenat, G. Finocchio, L. Lopez-Diaz, R. Chantrell, O. Chubykalo-Fesenko, and P. Bortolotti. Opportunities and challenges for spintronics in the microelectronics industry. *Nature Electronics*, 3(8):446–459, 2020.

[5] C. M. Fang, G. A. de Wijs, and R. A. de Groot. Spin-polarization in half-metals (invited). *Journal of Applied Physics*, 91(10):8340–8344, 2002.

[6] J. Puebla, J. Kim, K. Kondou, and Y. Otani. Spintronic devices for energy-efficient data storage and energy harvesting. *Communications Materials*, 1(1):24, 2020.

[7] S. Pathak, C. Youm, and J. Hong. Impact of spin-orbit torque on spin-transfer torque switching in magnetic tunnel junctions. *Scientific Reports*, 10(1), 2020.

[8] G. H. Jonker and J. H. Vansanten. Ferromagnetic compounds of manganese with perovskite structure. *Physica*, 16(3):337–349, 1950.

[9] J. Volger. Further experimental investigations on some ferromagnetic oxidic compounds of manganese with perovskite structure. *Physica*, 20(1):49–66, 1954.

[10] S. Jin, T. H. Tiefel, M. Mccormack, R. A. Fastnacht, R. Ramesh, and L. H. Chen. Thousandfold change in resistivity in magnetoresistive La-Ca-Mn-O films. *Science*, 264(5157):413–415, 1994.

[11] H. Y. Hwang, Y. Iwasa, M. Kawasaki, B. Keimer, N. Nagaosa, and Y. Tokura. Emergent phenomena at oxide interfaces. *Nature Materials*, 11(2):103–113, 2012.

[12] J. A. Sulpizio, S. Ilani, P. Irvin, and J. Levy. Nanoscale phenomena in oxide heterostructures. *Annual Review of Materials Research, Vol 44*, 44:117–149, 2014.

[13] M. Lorenz, M. S. R. Rao, T. Venkatesan, E. Fortunato, P. Barquinha, R. Branquinho, D. Salgueiro, R. Martins, E. Carlos, A. Liu, F. K. Shan, M. Grundmann, H. Boschker, J. Mukherjee, M. Priyadarshini, N. DasGupta, D. J. Rogers, F. H. Teherani, E. V. Sandana, P. Bove, K. Rietwyk, A. Zaban, A. Veziridis, A. Weidenkaff, M. Muralidhar, M. Murakami, S. Abel, J. Fompeyrine, J. Zuniga-Perez, R. Ramesh, N. A. Spaldin, S. Ostanin, V. Borisov, I. Mertig, V. Lazenka, G. Srinivasan, W. Prellier, M. Uchida, M. Kawasaki, R. Pentcheva, P. Gegenwart, F. M. Granozio, J. Fontcuberta, and N. Pryds. The 2016 oxide electronic materials and oxide interfaces roadmap. *Journal of Physics D-Applied Physics*, 49(43), 2016.

[14] A. Urushibara, Y. Moritomo, T. Arima, A. Asamitsu, G. Kido, and Y. Tokura. Insulator-metal transition and giant magnetoresistance in $La_{1-x}Sr_xMnO_3$. *Physical Review B*, 51(20):14103–14109, 1995.

[15] M. C. Martin, G. Shirane, Y. Endoh, K. Hirota, Y. Moritomo, and Y. Tokura. Magnetism and structural distortion in the $La_{0.7}Sr_{0.3}MnO_3$ metallic ferromagnet. *Physical Review B*, 53(21):14285–14290, 1996.

[16] A. Ohtomo and H. Y. Hwang. A high-mobility electron gas at the $LaAlO_3/SrTiO_3$ heterointerface. *Nature*, 427(6973):423–426, 2004.

[17] G. K. Chrisey, D. B. Hubler. *Pulsed Laser Deposition of Thin Films*. John Wiley & Sons, Inc, 1994.

[18] Y. Takamura, R. V. Chopdekar, E. Arenholz, and Y. Suzuki. Control of the magnetic and magnetotransport properties of $La_{0.67}Sr_{0.33}MnO_3$ thin films through epitaxial strain. *Applied Physics Letters*, 92(16), 2008.

[19] C. Adamo, X. Ke, H. Q. Wang, H. L. Xin, T. Heeg, M. E. Hawley, W. Zander, J. Schubert, P. Schiffer, D. A. Muller, L. Maritato, and D. G. Schlom. Effect of biaxial strain on the electrical and magnetic properties of (001) $La_{0.7}Sr_{0.3}MnO_3$ thin films. *Applied Physics Letters*, 95(11), 2009.

[20] L. M. Berndt, V. Balbarin, and Y. Suzuki. Magnetic anisotropy and strain states of (001) and (110) colossal magnetoresistance thin films. *Applied Physics Letters*, 77(18):2903–2905, 2000.

[21] I. Hallsteinsen, M. Moreau, R. V. Chopdekar, E. Christiansen, M. Nord, P. E. Vullum, J. K. Grepstad, R. Holmestad, S. M. Selbach, A. Scholl, E. Arenholz, E. Folven, and T. Tybell. Magnetic domain configuration of (111)-oriented $LaFeO_3$ epitaxial thin films. *Apl Materials*, 5(8), 2017.

[22] G. W. Zhou, F. X. Jiang, J. L. Zang, Z. Y. Quan, and X. H. Xu. Observation of superconductivity in the $LaNiO_3$/$La_{0.7}Sr_{0.3}MnO_3$ superlattice. *Acs Applied Materials & Interfaces*, 10(2):1463–1467, 2018.

[23] E. J. Guo, M. A. Roldan, X. H. Sang, S. Okamoto, T. Charlton, H. Ambaye, H. N. Lee, and M. R. Fitzsimmons. Influence of chemical composition and crystallographic orientation on the interfacial magnetism in $BiFeO_3$/$La_{1-x}Sr_xMnO_3$ superlattices. *Physical Review Materials*, 2(11), 2018.

[24] R. Martinez, A. Kumar, R. Palai, G. Srinivasan, and R. S. Katiyar. Observation of strong magnetoelectric effects in $Ba_{0.7}Sr_{0.3}TiO_3$/$La_{0.7}Sr_{0.3}MnO_3$ thin film heterostructures. *Journal of Applied Physics*, 111(10), 2012.

[25] S. Koohfar, A. B. Georgescu, A. N. Penn, J. M. LeBeau, E. Arenholz, and D. P. Kumah. Confinement of magnetism in atomically thin $La_{0.7}Sr_{0.3}CrO_3$/$La_{0.7}Sr_{0.3}MnO_3$ heterostructures. *Npj Quantum Materials*, 4, 2019.

[26] C. Tsang. Magnetics of small magnetoresistive sensors. *Journal of Applied Physics*, 55(6):2226–2231, 1984.

[27] T. Jungwirth, X. Marti, P. Wadley, and J. Wunderlich. Antiferromagnetic spintronics. *Nature Nanotechnology*, 11(3):231–241, 2016.

[28] E. Arenholz, G. van der Laan, F. Yang, N. Kemik, M. D. Biegalski, H. M. Christen, and Y. Takamura. Magnetic structure of $La_{0.7}Sr_{0.3}MnO_3$/$La_{0.7}Sr_{0.3}FeO_3$ superlattices. *Applied Physics Letters*, 94(7), 2009.

[29] F. Yang, N. Kemik, A. Scholl, A. Doran, A. T. Young, M. D. Biegalski, H. M. Christen, and Y. Takamura. Correlated domain structure in perovskite oxide superlattices exhibiting spin-flop coupling. *Physical Review B*, 83(1), 2011.

[30] E. Folven, A. Scholl, A. Young, S. T. Retterer, J. E. Boschker, T. Tybell, Y. Takamura, and J. K. Grepstad. Crossover from spin-flop coupling to collinear spin alignment in antiferromagnetic/ferromagnetic nanostructures. *Nano Letters*, 12(5):2386–2390, 2012.

[31] Y. Takamura, E. Folven, J. B. R. Shu, K. R. Lukes, B. Z. Li, A. Scholl, A. T. Young, S. T. Retterer, T. Tybell, and J. K. Grepstad. Spin-flop coupling and exchange bias in embedded complex oxide micromagnets. *Physical Review Letters*, 111(10), 2013.

[32] Y. Takamura, R. V. Chopdekar, A. Scholl, A. Doran, J. A. Liddle, B. Harteneck, and Y. Suzuki. Tuning magnetic domain structure in nanoscale $La_{0.7}Sr_{0.3}MnO_3$ islands. *Nano Letters*, 6(6):1287–1291, 2006.

[33] E. Folven, T. Tybell, A. Scholl, A. Young, S. T. Retterer, Y. Takamura, and J. K. Grepstad. Antiferromagnetic domain reconfiguration in embedded $LaFeO_3$ thin film nanostructures. *Nano Letters*, 10(11):4578–4583, 2010.

[34] E. Folven, J. Linder, O. V. Gomonay, A. Scholl, A. Doran, A. T. Young, S. T. Retterer, V. K. Malik, T. Tybell, Y. Takamura, and J. K. Grepstad. Controlling the switching field in nanomagnets by means of domain-engineered antiferromagnets. *Physical Review B*, 92(9), 2015.

[35] F. Y. Bruno, M. N. Grisolia, C. Visani, S. Valencia, M. Varela, R. Abrudan, J. Tornos, A. Rivera-Calzada, A. A. Unal, S. J. Pennycook, Z. Sefrioui, C. Leon, J. E. Villegas, J. Santamaria, A. Barthelemy, and M. Bibes. Insight into spin transport in oxide heterostructures from interface-resolved magnetic mapping. *Nature Communications*, 6, 2015.

[36] I. Hallsteinsen, M. Moreau, A. Grutter, M. Nord, P. E. Vullum, D. A. Gilbert, T. Bolstad, J. K. Grepstad, R. Holmestad, S. M. Selbach, A. T. N'Diaye, B. J. Kirby, E. Arenholz, and T. Tybell. Concurrent magnetic and structural reconstructions at the interface of (111)-oriented $LaFeO_3$/$La_{0.7}Sr_{0.3}MnO_3$. *Physical Review B*, 94(20), 2016.

[37] I. Hallsteinsen, A. Grutter, M. Moreau, S. D. Sloetjes, K. Kjaernes, E. Arenholz, and T. Tybell. Role of antiferromagnetic spin axis on magnetic reconstructions at the (111)-oriented $LaFeO_3/La_{0.7}Sr_{0.3}MnO_3$ interface. *Physical Review Materials*, 2(8), 2018.

[38] V. M. Goldschmidt. Die gesetze der krystallochemie. *Naturwissenschaften*, 14(21):477–485, 1926.

[39] N. A. Benedek and C. J. Fennie. Why are there so few perovskite ferroelectrics? *Journal of Physical Chemistry C*, 117(26):13339–13349, 2013.

[40] P. M. Woodward. Octahedral tilting in perovskites. II. structure stabilizing forces. *Acta Crystallographica Section B-Structural Science*, 53:44–66, 1997.

[41] A. M. Glazer. Classification of tilted octahedra in perovskites. *Acta Crystallographica Section B-Structural Science*, B 28(Nov15):3384–3392, 1972.

[42] J. M. Rondinelli and N. A. Spaldin. Structure and properties of functional oxide thin films: Insights from electronic-structure calculations. *Advanced Materials*, 23(30):3363–3381, 2011.

[43] J. W. Matthews and A. E. Blakeslee. Defects in epitaxial multilayers. I. misfit dislocations. *Journal of Crystal Growth*, 27(Dec):118–125, 1974.

[44] N. A. Pertsev, A. K. Tagantsev, and N. Setter. Phase transitions and strain-induced ferroelectricity in $SrTiO_3$ epitaxial thin films. *Physical Review B*, 61(2):R825–R829, 2000.

[45] J. H. Haeni, P. Irvin, W. Chang, R. Uecker, P. Reiche, Y. L. Li, S. Choudhury, W. Tian, M. E. Hawley, B. Craigo, A. K. Tagantsev, X. Q. Pan, S. K. Streiffer, L. Q. Chen, S. W. Kirchoefer, J. Levy, and D. G. Schlom. Room-temperature ferroelectricity in strained $SrTiO_3$. *Nature*, 430(7001):758–761, 2004.

[46] A. J. Hatt and N. A. Spaldin. Structural phases of strained $LaAlO_3$ driven by octahedral tilt instabilities. *Physical Review B*, 82(19), 2010.

[47] S. J. May, J. W. Kim, J. M. Rondinelli, E. Karapetrova, N. A. Spaldin, A. Bhattacharya, and P. J. Ryan. Quantifying octahedral rotations in strained perovskite oxide films. *Physical Review B*, 82(1), 2010.

[48] A. T. Zayak, X. Huang, J. B. Neaton, and K. M. Rabe. Structural, electronic, and magnetic properties of $SrRuO_3$ under epitaxial strain. *Physical Review B*, 74(9), 2006.

[49] P. Zubko, S. Gariglio, M. Gabay, P. Ghosez, and J. M. Triscone. Interface physics in complex oxide heterostructures. *Annual Review of Condensed Matter Physics, Vol 2*, 2:141–165, 2011.

[50] Z. Liao, M. Huijben, Z. Zhong, N. Gauquelin, S. Macke, R. J. Green, S. Van Aert, J. Verbeeck, G. Van Tendeloo, K. Held, G. A. Sawatzky, G. Koster, and G. Rijnders. Controlled lateral anisotropy in correlated manganite heterostructures by interface-engineered oxygen octahedral coupling. *Nature Materials*, 15(4):425–+, 2016.

[51] P. M. Raccah and J. B. Goodenough. First-order localized-electron = collective-electron transition in LaCoO3. *Physical Review*, 155(3):932–943, 1967.

[52] D. Treves. Studies on orthoferrites at Weizmann institute of science. *Journal of Applied Physics*, 36(3p2):1033–1039, 1965.

[53] P. W. Anderson. Antiferromagnetism - theory of superexchange interaction. *Physical Review*, 79(2):350–356, 1950.

[54] J. B. Goodenough. Theory of the role of covalence in the perovskite-type manganites [La,M(II)]MnO_3. *Physical Review*, 100(2):564–573, 1955.

[55] J. Kanamori. Superexchange interaction and symmetry properties of electron orbitals. *Journal of Physics and Chemistry of Solids*, 10(2-3):87–98, 1959.

[56] G. H. Jonker. Magnetic compounds with perovskite structure. iv. Conducting and non-conducting compounds. *Physica*, 22(8):707–722, 1956.

[57] E. Jahn, H.A. Teller. Stability of polyatomic molecules in degenerate electronic states, I-Orbital degeneracy. *Proc. R. Soc. Lond. A*, 161:220–235, 1937.

[58] C. Zener. Interaction between the d-shells in the transition metals. II. Ferromagnetic compounds of manganese with perovskite structure. *Physical Review*, 82(3):403–405, 1951.

[59] I. S. Lyubutin, T. V. Dmitrieva, and A. S. Stepin. Dependence of exchange interactions on chemical bond angle in a structural series: Cubic perovskite-rhombic orthoferrite-rhombohedral hematite. *Journal of Experimental and Theoretical Physics*, 88(3):590–597, 1999.

[60] I. Dzyaloshinsky. A thermodynamic theory of weak ferromagnetism of antiferromagnetics. *Journal of Physics and Chemistry of Solids*, 4(4):241–255, 1958.

[61] T. Moriya. Anisotropic superexchange interaction and weak ferromagnetism. *Physical Review*, 120(1):91–98, 1960.

[62] I. Sosnowska, T. Peterlinneumaier, and E. Steichele. Spiral magnetic-ordering in bismuth ferrite. *Journal of Physics C-Solid State Physics*, 15(23):4835–4846, 1982.

[63] I. Sosnowska and A. K. Zvezdin. Origin of the long-period magnetic-ordering in bifeo3. *Journal of Magnetism and Magnetic Materials*, 140:167–168, 1995.

[64] N. A. Spaldin. *Magnetic Materials Fundamentals and Applications*. Cambridge University Press, 2011.

[65] H.C. Stöhr, J. Siegmann. *Magnetism From Fundamentals to nanoscale Dynamics*. Springer, 2006.

[66] R. O'Handley. *Modern Magnetic Materials*. John Wiley & Sons, Inc, 2000.

[67] J.M.D. Coey. *Magnetism and Magnetic Materials*. Cambridge University Press, 2010.

[68] Y. Suzuki, H. Y. Hwang, S. W. Cheong, and R. B. vanDover. The role of strain in magnetic anisotropy of manganite thin films. *Applied Physics Letters*, 71(1):140–142, 1997.

[69] Y. Suzuki, H. Y. Hwang, S. W. Cheong, T. Siegrist, R. B. van Dover, A. Asamitsu, and Y. Tokura. Magnetic anisotropy of doped manganite thin films and crystals. *Journal of Applied Physics*, 83(11):7064–7066, 1998.

[70] N. C. Koon. Calculations of exchange bias in thin films with ferromagnetic/antiferromagnetic interfaces. *Physical Review Letters*, 78(25):4865–4868, 1997.

[71] A. E. Berkowitz and K. Takano. Exchange anisotropy - a review. *Journal of Magnetism and Magnetic Materials*, 200(1-3):552–570, 1999.

[72] W. Zhang and K. M. Krishnan. Epitaxial exchange-bias systems: From fundamentals to future spin-orbitronics. *Materials Science & Engineering R-Reports*, 105:1–20, 2016.

[73] J. Nogues and I. K. Schuller. Exchange bias. *Journal of Magnetism and Magnetic Materials*, 192(2):203–232, 1999.

[74] W. H. Meiklejohn and C. P. Bean. New magnetic anisotropy. *Physical Review*, 102(5):1413–1414, 1956.

[75] M. Kiwi. Exchange bias theory. *Journal of Magnetism and Magnetic Materials*, 234(3):584–595, 2001.

[76] T. C. Anthony and J. A. Brug. Magnetoresistance of symmetrical spin-valve structures. *Ieee Transactions on Magnetics*, 30(6):3819–3821, 1994.

[77] W. F. Egelhoff, P. J. Chen, C. J. Powell, M. D. Stiles, R. D. McMichael, C. L. Lin, J. M. Sivertsen, J. H. Judy, K. Takano, A. E. Berkowitz, T. C. Anthony, and J. A. Brug. Optimizing the giant magnetoresistance of symmetric and bottom spin valves. *Journal of Applied Physics*, 79(8):5277–5281, 1996.

[78] W. H. Meiklejohn. Exchange anisotropy - a review. *Journal of Applied Physics*, 33(3):1328–1335, 1962.

[79] P. Miltenyi, M. Gierlings, M. Bamming, U. May, G. Guntherodt, J. Nogues, M. Gruyters, C. Leighton, and I. K. Schuller. Tuning exchange bias. *Applied Physics Letters*, 75(15):2304–2306, 1999.

[80] S. Sahoo, T. Mukherjee, K. D. Belashchenko, and C. Binek. Isothermal low-field tuning of exchange bias in epitaxial Fe/Cr_2O_3/Fe. *Applied Physics Letters*, 91(17), 2007.

[81] T. Maity, S. Goswami, D. Bhattacharya, and S. Roy. Superspin glass mediated giant spontaneous exchange bias in a nanocomposite of $BiFeO_3$-$Bi_2Fe_4O_9$. *Physical Review Letters*, 110(10), 2013.

[82] S. Chauhan, S. K. Srivastava, and R. Chandra. Zero-field cooled exchange bias in hexagonal $YMnO_3$ nanoparticles. *Applied Physics Letters*, 103(4), 2013.

[83] J. K. Murthy and A. Venimadhav. Giant zero field cooled spontaneous exchange bias effect in phase separated $La_{1.5}Sr_{0.5}CoMnO_6$. *Applied Physics Letters*, 103(25), 2013.

[84] C. Shang, S. P. Guo, R. L. Wang, Z. G. Sun, H. B. Xiao, L. F. Xu, C. P. Yang, and Z. C. Xia. Positive to negative zero-field cooled exchange bias in $La_{0.5}Sr_{0.5}Mn_{0.8}Co_{0.2}O_3$ ceramics. *Scientific Reports*, 6, 2016.

[85] P. Huang, D. M. Deng, J. S. Zheng, Q. Li, Z. J. Feng, B. J. Kang, W. Ren, C. Jing, J. C. Zhang, and S. X. Cao. Negative magnetization and zero-field cooled exchange bias effect in $Eu_{0.9}Pr_{0.1}CrO_3$ ceramics. *Physica B-Condensed Matter*, 530:95–100, 2018.

[86] J. K. Murthy and P. S. A. Kumar. Interface-induced spontaneous positive and conventional negative exchange bias effects in bilayer $La_{0.7}Sr_{0.3}MnO_3$/$Eu_{0.45}Sr_{0.55}MnO_3$ heterostructures. *Sci Rep*, 7(1):6919, 2017.

[87] W. H. Meiklejohn and C. P. Bean. New magnetic anisotropy. *Physical Review*, 105(3):904–913, 1957.

[88] H. Ohldag, A. Scholl, F. Nolting, E. Arenholz, S. Maat, A. T. Young, M. Carey, and J. Stohr. Correlation between exchange bias and pinned interfacial spins. *Physical Review Letters*, 91(1):017203, 2003.

[89] J. Nogues, T. J. Moran, D. Lederman, I. K. Schuller, and K. V. Rao. Role of interfacial structure on exchange-biased FeF_2-Fe. *Physical Review B*, 59(10):6984–6993, 1999.

[90] J. Nogues, J. Sort, V. Langlais, V. Skumryev, S. Surinach, J. S. Munoz, and M. D. Baro. Exchange bias in nanostructures. *Physics Reports-Review Section of Physics Letters*, 422(3):65–117, 2005.

[91] Y. Jia, R. V. Chopdekar, E. Arenholz, A. T. Young, M. A. Marcus, A. Mehta, and Y. Takamura. Exchange coupling in (111)-oriented $La_{0.7}Sr_{0.3}MnO_3$/$La_{0.7}Sr_{0.3}FeO_3$ superlattices. *Physical Review B*, 92(9), 2015.

[92] X. Ke, M. S. Rzchowski, L. J. Belenky, and C. B. Eom. Positive exchange bias in ferromagnetic $La_{0.67}Sr_{0.33}MnO_3$/$SrRuO_3$ bilayers. *Applied Physics Letters*, 84(26):5458–5460, 2004.

[93] R. Rana, P. Pandey, R. P. Singh, and D. S. Rana. Positive exchange-bias and giant vertical hysteretic shift in $La_{0.7}Sr_{0.3}MnO_3$/$SrRuO_3$ bilayers. *Scientific Reports*, 4, 2014.

[94] M. Kawasaki, K. Takahashi, T. Maeda, R. Tsuchiya, M. Shinohara, O. Ishiyama, T. Yonezawa, M. Yoshimoto, and H. Koinuma. Atomic control of the $SrTiO_3$ crystal-surface. *Science*, 266(5190):1540–1542, 1994.

[95] Y. Y. Pai, A. Tylan-Tyler, P. Irvin, and J. Levy. Physics of $SrTiO_3$-based heterostructures and nanostructures: a review. *Reports on Progress in Physics*, 81(3), 2018.

[96] J. F. Scott. Soft-mode spectroscopy - experimental studies of structural phase-transitions. *Reviews of Modern Physics*, 46(1):83–128, 1974.

[97] D. Pesquera, V. Skumryev, F. Sanchez, G. Herranz, and J. Fontcuberta. Magnetoelastic coupling in $La_{2/3}Sr_{1/3}MnO_3$ thin films on $SrTiO_3$. *Physical Review B*, 84(18), 2011.

[98] W. D. Luo, W. H. Duan, S. G. Louie, and M. L. Cohen. Structural and electronic properties of n-doped and p-doped $SrTiO_3$. *Physical Review B*, 70(21), 2004.

[99] T. Tomio, H. Miki, H. Tabata, T. Kawai, and S. Kawai. Control of electrical-conductivity in laser-deposited $SrTiO_3$ thin-films with Nb doping. *Journal of Applied Physics*, 76(10):5886–5890, 1994.

[100] K. Fukushima and S. Shibagaki. Nb doped $SrTiO_3$ thin films deposited by pulsed laser ablation. *Thin Solid Films*, 315(1-2):238–243, 1998.

[101] Z. Q. Liu, W. M. Lu, S. L. Lim, X. P. Qiu, N. N. Bao, M. Motapothula, J. B. Yi, M. Yang, S. Dhar, T. Venkatesan, and Ariando. Reversible room-temperature ferromagnetism in Nb-doped $SrTiO_3$ single crystals. *Physical Review B*, 87(22), 2013.

[102] H. Fujishiro, T. Fukase, and M. Ikebe. Charge ordering and sound velocity anomaly in la1-xsrxmno3 (x >= 0.5). *Journal of the Physical Society of Japan*, 67(8):2582–2585, 1998.

[103] D. Louca, T. Egami, E. L. Brosha, H. Roder, and A. R. Bishop. Local jahn-teller distortion in $La_{1-x}Sr_xMnO_3$ observed by pulsed neutron diffraction. *Physical Review B*, 56(14):R8475–R8478, 1997.

[104] M. Bowen, M. Bibes, A. Barthelemy, J. P. Contour, A. Anane, Y. Lemaitre, and A. Fert. Nearly total spin polarization in $La_{2/3}Sr_{1/3}MnO_3$ from tunneling experiments. *Applied Physics Letters*, 82(2):233–235, 2003.

[105] Y. Tokura. Critical features of colossal magnetoresistive manganites. *Reports on Progress in Physics*, 69(3):797–851, 2006.

[106] P. G. Radaelli, G. Iannone, M. Marezio, H. Y. Hwang, S. W. Cheong, J. D. Jorgensen, and D. N. Argyriou. Structural effects on the magnetic and transport properties of perovskite $A_{1-x}A_x'MnO_3$ (x=0.25, 0.30). *Physical Review B*, 56(13):8265–8276, 1997.

[107] Y. Moritomo, A. Asamitsu, and Y. Tokura. Pressure effect on the double-exchange ferromagnet $La_{1-x}Sr_xMnO_3$ ($0.15 \leq x \leq 0.5$). *Physical Review B*, 51(22):16491–16494, 1995.

[108] D. P. Kozlenko, I. N. Goncharenko, B. N. Savenko, and V. I. Voronin. High pressure effects on the crystal and magnetic structure of $La_{0.7}Sr_{0.3}MnO_3$. *Journal of Physics-Condensed Matter*, 16(37):6755–6762, 2004.

[109] A. Khapikov, L. Uspenskaya, I. Bdikin, Y. Mukovskii, S. Karabashev, D. Shulyaev, and A. Arsenov. Magnetic domains and twin structure of the $La_{0.7}Sr_{0.3}MnO_3$ single crystal. *Applied Physics Letters*, 77(15):2376–2378, 2000.

[110] K. Steenbeck, R. Hiergeist, A. Revcolevschi, and L. Pinsard-Gaudart. Magnetic anisotropy in $la_{0.7}(Sr,Ca)_{0.3}MnO_3$ epitaxial thin films and crystals. *Polycrystalline Metal and Magnetic Thin Films*, 562:57–62, 1999.

[111] M. Konoto, T. Kohashi, K. Koike, T. Arima, Y. Kaneko, Y. Tomioka, and Y. Tokura. Magnetic domain structure of a $La_{0.7}Sr_{0.3}MnO_3$ (001) surface observed by a spin-polarized scanning electron microscope. *Applied Physics Letters*, 84(13):2361–2363, 2004.

[112] A. Vailionis, H. Boschker, W. Siemons, E. P. Houwman, D. H. A. Blank, G. Rijnders, and G. Koster. Misfit strain accommodation in epitaxial ABO_3 perovskites: Lattice rotations and lattice modulations. *Physical Review B*, 83(6), 2011.

[113] I. Hallsteinsen, E. Folven, F. K. Olsen, R. V. Chopdekar, M. S. Rzchowski, C. B. Eom, J. K. Grepstad, and T. Tybell. Crystalline symmetry controlled magnetic switching in epitaxial (111) $La_{0.7}Sr_{0.3}MnO_3$ thin films. *Apl Materials*, 3(6), 2015.

[114] A. Monsen, J. E. Boschker, F. Macia, J. W. Wells, P. Nordblad, A. D. Kent, R. Mathieu, T. Tybell, and E. Wahlström. Thickness dependence of dynamic and static magnetic properties of pulsed laser deposited $La_{0.7}Sr_{0.3}MnO_3$ films on $SrTiO_3$(001). *Journal of Magnetism and Magnetic Materials*, 369:197–204, 2014.

[115] M. Huijben, L. W. Martin, Y. H. Chu, M. B. Holcomb, P. Yu, G. Rijnders, D. H. A. Blank, and R. Ramesh. Critical thickness and orbital ordering in ultrathin $La_{0.7}Sr_{0.3}MnO_3$ films. *Physical Review B*, 78(9), 2008.

[116] A. Tebano, C. Aruta, S. Sanna, P. G. Medaglia, G. Balestrino, A. A. Sidorenko, R. De Renzi, G. Ghiringhelli, L. Braicovich, V. Bisogni, and

N. B. Brookes. Evidence of orbital reconstruction at interfaces in ultrathin $La_{0.67}Sr_{0.33}MnO_3$ films. *Physical Review Letters*, 100(13), 2008.

[117] R. Herger, P. R. Willmott, C. M. Schleputz, M. Bjorck, S. A. Pauli, D. Martoccia, B. D. Patterson, D. Kumah, R. Clarke, Y. Yacoby, and M. Dobeli. Structure determination of monolayer-by-monolayer grown $La_{1-x}Sr_xMnO_3$ thin films and the onset of magnetoresistance. *Physical Review B*, 77(8), 2008.

[118] J. Rao, C. N. R. Gopalakrishnan. *New Directions in Solid State Chemistry*. Cambridge University Press, 2nd edition, 1997.

[119] J. Dho, N. H. Hur, I. S. Kim, and Y. K. Park. Oxygen pressure and thickness dependent lattice strain in $La_{0.7}Sr_{0.3}MnO_3$ films. *Journal of Applied Physics*, 94(12):7670–7674, 2003.

[120] M. Eibschutz, S. Shtrikman, and D. Treves. Mossbauer studies of Fe^{57} in orthoferrites. *Physical Review*, 156(2):562–+, 1967.

[121] J. Stohr, A. Scholl, T. J. Regan, S. Anders, J. Luning, M. R. Scheinfein, H. A. Padmore, and R. L. White. Images of the antiferromaguetic structure of a NiO(100) surface by means of x-ray magnetic linear dichroism spectromicroscopy. *Physical Review Letters*, 83(9):1862–1865, 1999.

[122] A. Scholl, J. Stohr, J. Luning, J. W. Seo, J. Fompeyrine, H. Siegwart, J. P. Locquet, F. Nolting, S. Anders, E. E. Fullerton, M. R. Scheinfein, and H. A. Padmore. Observation of antiferromagnetic domains in epitaxial thin films. *Science*, 287(5455):1014–1016, 2000.

[123] J. W. Seo, E. E. Fullerton, F. Nolting, A. Scholl, J. Fompeyrine, and J. P. Locquet. Antiferromagnetic lafeo3 thin films and their effect on exchange bias. *Journal of Physics-Condensed Matter*, 20(26), 2008.

[124] R. L. White. Review of recent work on magnetic and spectroscopic properties of rare-earth orthoferrites. *Journal of Applied Physics*, 40(3):1061–+, 1969.

[125] J. Luning, F. Nolting, A. Scholl, H. Ohldag, J. W. Seo, J. Fompeyrine, J. P. Locquet, and J. Stohr. Determination of the antiferromagnetic spin axis in epitaxial $LaFeO_3$ films by x-ray magnetic linear dichroism spectroscopy. *Physical Review B*, 67(21), 2003.

[126] E. Folven, A. Scholl, A. Young, S. T. Retterer, J. E. Boschker, T. Tybell, Y. Takamura, and J. K. Grepstad. Effects of nanostructuring and substrate

symmetry on antiferromagnetic domain structure in $LaFeO_3$ thin films. *Physical Review B*, 84(22), 2011.

[127] S. Czekaj, F. Nolting, L. J. Heyderman, P. R. Willmott, and G. van der Laan. Sign dependence of the x-ray magnetic linear dichroism on the antiferromagnetic spin axis in $LaFeO_3$ thin films. *Physical Review B*, 73(2), 2006.

[128] S. Czekaj, F. Nolting, L. J. Heyderman, K. Kunze, and M. Kruger. Antiferromagnetic domain configurations in patterned $LaFeO_3$ thin films. *Journal of Physics-Condensed Matter*, 19(38), 2007.

[129] J. K. Grepstad, Y. Takamura, A. Scholl, I. Hole, Y. Suzuki, and T. Tybell. Effects of thermal annealing in oxygen on the antiferromagnetic order and domain structure of epitaxial lafeo3 thin films. *Thin Solid Films*, 486(1-2):108–112, 2005.

[130] A. D. Bang, I. Hallsteinsen, R. V. Chopdekar, F. K. Olsen, S. D. Sloetjes, K. Kjaernes, E. Arenholz, E. Folven, and J. K. Grepstad. Shape-imposed anisotropy in antiferromagnetic complex oxide nanostructures. *Applied Physics Letters*, 115(11), 2019.

[131] A. D. Bang, I. Hallsteinsen, F. K. Olsen, S. D. Sloetjes, S. T. Retterer, A. Scholl, E. Arenholz, E. Folven, and J. K. Grepstad. Neel vector reorientation in ferromagnetic/antiferromagnetic complex oxide nanostructures. *Applied Physics Letters*, 114(19), 2019.

[132] D. Dijkkamp, T. Venkatesan, X. D. Wu, S. A. Shaheen, N. Jisrawi, Y. H. Minlee, W. L. Mclean, and M. Croft. Preparation of Y-Ba-Cu oxide superconductor thin-films using pulsed laser evaporation from high-Tc bulk material. *Applied Physics Letters*, 51(8):619–621, 1987.

[133] M. K. Wu, J. R. Ashburn, C. J. Torng, P. H. Hor, R. L. Meng, L. Gao, Z. J. Huang, Y. Q. Wang, and C. W. Chu. Superconductivity at 93 K in a new mixed-phase Y-Ba-Cu-O compound system at ambient pressure. *Physical Review Letters*, 58(9):908–910, 1987.

[134] G. Koster, D. H. A. Blank, and G. A. J. H. M. Rijnders. Oxygen in complex oxide thin films grown by pulsed laser deposition: a perspective. *Journal of Superconductivity and Novel Magnetism*, 33(1):205–212, 2020.

[135] I. Bozovic and J. N. Eckstein. Analysis of growing films of complex oxides by RHEED. *Mrs Bulletin*, 20(5):32–38, 1995.

[136] G. J. H. M. Rijnders, G. Koster, D. H. A. Blank, and H. Rogalla. In situ monitoring during pulsed laser deposition of complex oxides using reflection high energy electron diffraction under high oxygen pressure. *Applied Physics Letters*, 70(14):1888–1890, 1997.

[137] J. E. Boschker and T. Tybell. Qualitative determination of surface roughness by in situ reflection high energy electron diffraction. *Applied Physics Letters*, 100(15), 2012.

[138] G. Binnig, C. F. Quate, and C. Gerber. Atomic force microscope. *Physical Review Letters*, 56(9):930–933, 1986.

[139] S. Foner. Vibrating sample magnetometer. *Review of Scientific Instruments*, 27(7):548–548, 1956.

[140] S. Foner. Versatile and sensitive vibrating-sample magnetometer. *Review of Scientific Instruments*, 30(7):548–557, 1959.

[141] E. Arenholz, G. van der Laan, R. V. Chopdekar, and Y. Suzuki. Anisotropic x-ray magnetic linear dichroism at the Fe $L_{2,3}$ edges in Fe_3O_4. *Physical Review B*, 74(9), 2006.

[142] E. Arenholz, G. van der Laan, R. V. Chopdekar, and Y. Suzuki. Angle-dependent Ni^{2+} x-ray magnetic linear dichroism: Interfacial coupling revisited. *Physical Review Letters*, 98(19), 2007.

ISBN 978-82-326-5474-1 (printed ver.)
ISBN 978-82-326-5491-8 (electronic ver.)
ISSN 1503-8181 (printed ver.)
ISSN 2703-8084 (online ver.)

NTNU

Norwegian University of
Science and Technology